Ministère de l'Enseignement Supérieur et de la Recherche Scientifique

جامعة أكلي محند أولحاج - البويرة

Université Akli Mohand Oulhadj Bouira

كلية الـعـلــــــــوم التطبيقية

Faculté des Sciences Appliquées

Département de génie électrique

Laboratoire des Matériaux et du Développement Durable (LMDD)

THESE DE DOCTORAT

Présentée en vue de l'obtention du grade de docteur

En : Électrotechnique

Spécialité : Énergies Renouvelables

Par :

Achit Mohamed

Intitulée :

Diagnostic des defauts dans un systeme photovoltaïque

Soutenue publiquement devant le jury composé de :

MELLAH Hacene	MCA	Président	Université de Bouira
YASSA Nacera	MCA	Encadrant	Université de Bouira
BOUZIDA Ahcene	Prof	Co-encadrant	Université de Bouira
BOUDOUDA Aimad	Prof	Examinateur	Université de Boumerdes
AIBECHE Abderrezak	MCA	Examinateur	Université de Boumerdes
BENSAFIA Yacine	Prof	Examinateur	Université de Bouira
MAAFA Amar	MCA	Examinateur	Université de Bouira

2025/2026

Ministry of Higher Education and Scientific Research
جامعة أكلي محند أولحاج - البويرة
University of Akli Mohand Oulhadj Bouira
كلية الـعـلــــــــوم التطبيقية
Faculty of Applied Sciences

Department of electrical engineering

Laboratory of Materials and Sustainable Development (LMSD)

DOCTORAL THESIS

Presented to obtain the degree of doctor

In: Electrotechnics

Specialty: Renewable energies

By :

Achit Mohamed

Entitled:

Fault diagnosis in a photovoltaic system

Publicly defended in front of the jury composed of:

MELAH Hacene	MCA	President	Bouira University
YASSA Nacera	MCA	Supervisor	Bouira University
BOUZIDA Ahcene	Prof	Co-supervisor	Bouira University
BOUDOUDA Aimad	Prof	Examiner	Boumerdes University
AIBECHE Abderrezak	MCA	Examiner	Boumerdes University
BENSAFIA Yacine	Prof	Examiner	Bouira University
MAAFA Amar	MCA	Examiner	Bouira University

2025/2026

Acknowledgements

I sincerely thank all individuals who supported the completion of this doctoral thesis. I am especially grateful to my supervisor, Professor Yassa Nacera, for her guidance, expertise, and constant support, which were crucial to the success of this work. I also thank my co-supervisor, Professor Bouzida Ahcene, for his valuable technical input and constructive advice.

I would like to express my sincere gratitude to Dr MELLAH Hacene, President of the jury, and to Professor BOUDOUDA Aimad, Dr AIBECHE abderrezak, Professor BENSAFIA Yacine, and Dr MAAFA Amar for accepting to evaluate this thesis. I deeply appreciate the time they devoted to reviewing this work and their valuable comments, insightful suggestions, and constructive discussions, which have significantly contributed to improving the quality of this dissertation.

My appreciation also extends to the LMDD Laboratory and the Department of Electrical Engineering at the University of Akli Mohand Oulhadj Bouira for providing an encouraging and supportive research environment. I am thankful to my colleagues and friends for their support throughout this journey.

Above all, I am deeply grateful to my parents for their unwavering encouragement, unconditional love, and countless sacrifices, without which this achievement would not have been possible.

ABSTRACT

This thesis evaluates deep learning-based object detection for automated photovoltaic (PV) inspection using thermal infrared and electroluminescence (EL) imaging. For thermal hotspot detection, the transformer-based RT-DETR consistently outperformed YOLOv8, achieving a higher mAP of 0.802 and eliminating post-processing time. For EL imagery, detecting subtle cell-level defects required finer feature extraction; the proposed PV-YOLOv12n model, developed by integrating an A2C2f module, achieved an improved mAP@50 of 0.91, outperforming the baseline YOLOv12n in identifying low-contrast cracks. Overall, this research demonstrates that tailored deep learning architectures offer robust solutions for real-time PV inspection, optimizing energy yield and reducing maintenance costs.

Keywords: Photovoltaic (PV) inspection, Deep learning, Object detection, Thermal infrared imaging, Electroluminescence (EL), RT-DETR, YOLOv8, PV-YOLOv12n, Hotspot detection, Defect screening.

ملخص

تقيم هذه الأطروحة نماذج كشف الكائنات القائمة على التعلم العميق للفحص الآلي للألواح الكهروضوئية (PV) باستخدام التصوير بالأشعة تحت الحمراء الحرارية والتصوير بالوميض الكهربائي (EL). بالنسبة لكشف النقاط الساخنة الحرارية، تفوق نموذج RT-DETRالقائم على الترانزستور باستمرار علىYOLOv8 ، محققاً معدل mAP أعلى قدره 0.802 مع إلغاء وقت المعالجة اللاحقة. أما بالنسبة لتصوير الوميض الكهربائي(EL) ، فقد تطلب اكتشاف العيوب الدقيقة على مستوى الخلايا استخلاصًا أدق للميزات؛ حيث حقق النموذج المقترحPV-YOLOv12n ، المدعم بوحدة A2C2f ، معدل mAP@50 محسناً قدره 0.91، متفوقاً على النموذج الأساسي YOLOv12n في تحديد الشقوق منخفضة التباين. ختاماً، تُظهر هذه الدراسة أن بنيات التعلم العميق المخصصة تقدم حلولاً قوية للفحص الفوري للأنظمة الكهروضوئية، مما يساهم في تقليل تكاليف الصيانة وتحسين إنتاج الطاقة.

الكلمات المفتاحية :الفحص الكهروضوئي، التعلم العميق، كشف الكائنات، التصوير بالأشعة تحت الحمراء الحرارية، الوميض الكهربائي، PV-YOLOv12n, RT-DETR, YOLOv8، كشف النقاط الساخنة، فحص العيوب.

Résumé

Cette thèse évalue la détection d'objets par apprentissage profond pour l'inspection automatisée des panneaux photovoltaïques (PV) via l'imagerie infrarouge thermique et l'électroluminescence (EL). Pour la détection des points chauds thermiques, le modèle basé sur les transformeurs RT-DETR a systématiquement surpassé YOLOv8, atteignant un mAP supérieur de 0,802 et éliminant le temps de post-traitement. Pour l'imagerie EL, la détection des défauts subtils au niveau des cellules a nécessité une extraction de caractéristiques plus précise ; le modèle proposé, PV-YOLOv12n, intégrant un module A2C2f, a atteint un mAP@50 amélioré de 0,91, surpassant le YOLOv12n de base pour identifier les fissures à faible contraste. En somme, ces travaux démontrent que des architectures d'apprentissage profond adaptées offrent des solutions robustes pour l'inspection PV en temps réel, optimisant le rendement et réduisant les coûts de maintenance.

Mots-clés: Inspection photovoltaïque (PV), Apprentissage profond, Détection d'objets, Imagerie infrarouge thermique, Électroluminescence (EL), RT-DETR, YOLOv8, PV-YOLOv12n, Détection des points chauds, Dépistage des défauts.

Table of contents

List of figures

List of tables

List of symbols

Symbol	Description
V	Output voltage
I	Output current
Pout	Output power
Voc	Open-circuit voltage
Isc	Short-circuit current
Vmpp	Voltage at the maximum power point
Impp	Current at the maximum power point
Pmpp	Maximum power output
FF	Fill factor
η	Conversion efficiency
G	Solar irradiance
T	Cell temperature
Rs	Series resistance
Rsh	Shunt resistance
Iph	Photogenerated current
I0	Diode reverse saturation current
n	Diode ideality factor
q	Electron charge
k	Boltzmann constant
E	Electrical energy

Symbol	Description
TP	True Positive
TN	True Negative
FP	False Positive
FN	False Negative
Prec	Precision
Rec	Recall
F1	F1-score
Acc	Accuracy
Spec	Specificity
IoU	Intersection over Union
AP	Average Precision
mAP@0.5	Mean Average Precision at IoU = 0.5
mAP@0.5:0.95	Mean Average Precision averaged over IoU thresholds from 0.5 to 0.95
Conf	Confidence score
L	Loss function
FPS	Frames per second
GFLOPs	Giga Floating Point Operations

List of abbreviation

Abbreviation	Definition
AI	Artificial Intelligence
ANN	Artificial Neural Network
AP	Average Precision
AUC	Area Under the Curve
CNN	Convolutional Neural Network
CSP	Cross Stage Partial
DDM	Double-Diode Model
DL	Deep Learning
DSP	Digital Signal Processing
DWConv	Depthwise Convolution
ECA	Efficient Channel Attention
EL	Electroluminescence
FFT	Fast Fourier Transform
FF	Fill Factor
FLOPs	Floating Point Operations
FPS	Frames Per Second
GAN	Generative Adversarial Network
GFLOPs	Giga Floating Point Operations
GHG	Greenhouse Gas
GPS	Global Positioning System
IMU	Inertial Measurement Unit

Abbreviation	**Definition**
IoT	Internet of Things
IoU	Intersection over Union
IR	Infrared
IRT	Infrared Thermography
LCOE	Levelized Cost of Electricity
LIT	Lock-In Thermography
MCSAM	Multi-Channel Spatial Attention Module
MFI	Magnetic Field Imaging
MLP	Multi-Layer Perceptron
MPP	Maximum Power Point
MPPT	Maximum Power Point Tracking
mAP	Mean Average Precision
NMS	Non-Maximum Suppression
PAN	Path Aggregation Network
PID	Potential-Induced Degradation
PL	Photoluminescence
PLC	Programmable Logic Controller
PR	Performance Ratio
PV	Photovoltaic
PVEL-AD	Photovoltaic Electroluminescence Anomaly Detection Dataset
PV-YOLOv12n	Proposed Modified YOLOv12 Nano Model for Photovoltaic Defect Detection
RCA	Residual Channel Attention

Abbreviation	**Definition**
ReLU	Rectified Linear Unit
RES	Renewable Energy Sources
RGB	Red, Green, Blue
RMS	Root Mean Square
RT-DETR	Real-Time Detection Transformer
SC	Solar Cell
SDM	Single-Diode Model
SGD	Stochastic Gradient Descent
SP	Solar Panel
SPPF	Spatial Pyramid Pooling–Fast
SVM	Support Vector Machine
UAV	Unmanned Aerial Vehicle
UV	Ultraviolet
ViT	Vision Transformer
YOLO	You Only Look Once

General introduction

The global transition toward sustainable energy has established utility-scale photovoltaic (PV) power plants as indispensable pillars of the modern energy grid. However, ensuring the operational efficiency, prolonged lifespan, and structural integrity of these assets presents a critical technical challenge. PV installations are continuously subjected to severe environmental stressors, mechanical loading, and cyclic thermal fluctuations that induce material-level and system-level degradation. To mitigate energy yield losses and avoid catastrophic localized failures such as localized fire hazards non-contact non-destructive testing (NDT) methodologies have become the industry standard for intelligent operation and maintenance (O&M) strategies.

Among these techniques, infrared thermography (IRT) and electroluminescence (EL) imaging are widely recognized as complementary diagnostics. IRT, typically captured via unmanned aerial vehicles (UAVs) at the system level, excels at identifying surface anomalies and thermal abnormalities, such as hot spots caused by bypass diode failures, partial shading, or localized short circuits [1], [2]. Conversely, EL imaging operates at the component scale of individual solar cells. By forward-biasing the PV cell to emit near-infrared light, EL imaging reveals sub-surface material-level defects, including microcracks, finger-line interruptions, cell disconnects, and potential induced degradation (PID) [3], [4].

Historically, defect evaluation relied on manual visual inspection by human experts a process that is inherently slow, error-prone, subjective, and economically unviable for gigawatt-scale power plants. To address this, early automated approaches deployed traditional computer vision and machine learning (ML) workflows. These methods relied on handcrafted feature descriptors, such as Local Binary Patterns (LBP) or Scale-Invariant Feature Transform (SIFT), combined with classic classifiers like Support Vector Machines (SVM) or Random Forests. While effective under controlled laboratory settings, these shallow learning frameworks struggled significantly in real-world scenarios due to low generalization capabilities, poor adaptation to complex environmental noise, and high sensitivity to varying illumination and flight parameters.

The emergence of Deep Learning (DL) and Convolutional Neural Networks (CNNs) initiated a paradigm shift in PV defect detection. Two-stage object detectors, such as Faster R-CNN, coupled with Feature Pyramid Networks (FPN), offered high spatial localization accuracy for multi-scale anomalies but suffered from intensive computational overhead. Consequently, research pivoted toward single-stage detectors, primarily from the You Only Look Once (YOLO) lineage such as YOLOv8 through YOLO11 and Single Shot MultiBox Detectors (SSD) [5], [6], [7]. These architectures significantly increased throughput by combining localization and classification into a single forward pass, providing real-time processing capabilities [8], [9].

Concurrently, the development of Vision Transformers (ViTs) introduced Detection Transformer (DETR) families, which capture long-range global contextual dependencies via self-attention mechanisms [10], [11]. The recent introduction of the Real-Time Detection Transformer (RT-DETR) successfully bridged the gap between transformer-based global semantic understanding and real-time processing requirements by eliminating non-maximum suppression (NMS) bottlenecks [12], [13]. The cutting edge of PV vision has further evolved with the launch of the YOLOv12 framework, introducing FlashAttention-driven area attention mechanisms within feature networks to isolate subtle structural defects amidst complex background clutters [14].

Despite the rapid advancements in deep learning frameworks, automating the inspection of PV installations remains a challenging problem. This doctoral thesis addresses a multi-scale diagnostic problem: How can a unified intelligent vision framework achieve both highly localized structural fidelity at the micro-component level and rapid, low-latency semantic processing at the macro-system level, under severe computational and environmental edge constraints?

This problem is characterized by four fundamental challenges that limit current state-of-the-art models:

- **The multiscale and multi-modal disconnect:** Existing architectures are typically optimized for a single modality or structural scale. Models designed for macro-level IRT drone footage struggle to detect small defects due to atmospheric distortion, varying flight altitudes, and background noise [13]. Conversely, component-level EL imagery features micro-scale defects, such as sub-millimeter line cracks, that are embedded in dense structural noise like busbars and finger lines [13]. Current models lack the architectural adaptability to suppress structural noise at the component level while preserving high-speed execution at the system level.

- **The post-processing latency bottleneck:** Utility-scale solar fields demand immediate, onboard anomaly sorting to guide autonomous UAV navigation. While single-stage CNN models deliver high frame rates, they rely heavily on NMS post-processing to eliminate redundant bounding boxes. NMS introduces a highly unstable, data-dependent computational bottleneck during dense defect clustering, which increases latency and reduces edge computing viability [1].

- **The parameter-precision tradeoff for edge hardware:** Improving a model's sensitivity to low-contrast, fine-grained structural defects typically requires expanding the network's parameter volume or depth. However, aerial drones and industrial embedded vision boards possess strict payload and energy constraints [8]. Deploying heavy networks causes severe latency or thermal throttling, whereas aggressive lightweighting compromises the representation capacity needed to detect complex, curved, or faint anomalies [7].

- **Severe dataset class imbalance and environmental noise:** Real-world solar installations present highly skewed defect distributions where critical failure states, such as cracked bypass diodes or micro-dislocations, are rarely captured compared to standard operating conditions. This lack of representative data leads to poor model sensitivity and weak generalization under unseen environmental, dust accumulation, and weather conditions [9].

To resolve these bottlenecks, this thesis introduces an architectural framework that redefines the efficiency-accuracy boundary across both IRT and EL inspection domains. The primary contributions and originality of this work are summarized as follows:

- **Elimination of NMS latency via RT-DETR for system-level IRT:** This work introduces the transformer-based RT-DETR paradigm to aerial infrared thermography for solar panels. By replacing the traditional NMS layer with an end-to-end Hungarian matching assignment algorithm, this model resolves the post-processing latency bottleneck. It achieves an elite processing throughput of 114 FPS and a superior mAP@50 of 0.802, providing a high-speed, post-processing-free detector viable for edge-guided autonomous UAV flight.

- **Design of the lightweight PV-YOLOv12n with background suppression:** For component-scale EL images, this thesis designs a lightweight architecture, PV-YOLOv12n, restricting the model footprint to just 2.6 million parameters. The core originality lies in the integration of an Attention-driven A2C2f module at the deep P5 scale. This structural addition dynamically filters out repetitive background patterns like busbars and fingers, allowing the network to focus on low-contrast material fractures and achieving an mAP@50 of 0.91 on highly imbalanced benchmarks [15].

- **Validation across multi-dataset benchmarks:** The proposed frameworks are rigorously validated against established open benchmarks, including PVEL-AD and Roboflow. This ensures high architectural reproducibility and robust generalization across varying sensor resolutions, aspect ratios, and industrial manufacturing environments.

Organization of the thesis

This thesis is organized into five chapters, in addition to a general introduction and a general conclusion.

- Chapter I presents the theoretical background required for the remainder of the thesis. It discusses the importance of renewable energy and photovoltaic technology, the main components of photovoltaic systems, the operating principle and mathematical modeling of photovoltaic cells, and their electrical characteristics.
- Chapter II provides a comprehensive review of photovoltaic module defects and fault diagnosis. It examines the structure of photovoltaic modules, the most common degradation mechanisms and failure modes, non-destructive inspection techniques, quantitative performance evaluation metrics, and recent advances in deep learning-based defect detection. The chapter concludes by identifying the current research gaps and motivating the proposed methodologies.
- Chapter III reviews the principal techniques employed for fault diagnosis in photovoltaic systems. It covers aerial inspection methods, current–voltage (I–V) curve analysis, signal processing approaches, analytical monitoring techniques, and other emerging fault detection methods, highlighting their operating principles, advantages, and limitations.
- Chapter IV presents the proposed methodology for system-level photovoltaic panel inspection using infrared thermal imagery. A comparative study between the transformer-based RT-DETR model and the YOLOv8 architecture is conducted to evaluate their effectiveness in hotspot detection under real-time operating conditions.

- Chapter V introduces the proposed lightweight PV-YOLOv12n architecture for defect detection in electroluminescence (EL) images. The chapter describes the datasets, architectural modifications, implementation methodology, experimental evaluation, ablation studies, and comparisons with state-of-the-art approaches.

Finally, the thesis concludes with a summary of the main findings and contributions of the research, discusses its limitations, and outlines potential directions for future work in intelligent photovoltaic fault diagnosis and automated inspection systems.

Chapter I: Fundamentals of photovoltaic energy conversion

I.1 Introduction:

The increasing global demand for energy, coupled with concerns over climate change, environmental degradation, and the depletion of fossil fuel reserves, has accelerated the transition toward sustainable and renewable energy sources. Renewable energy technologies, including solar, wind, hydroelectric, biomass, and geothermal energy, have become essential components of modern energy systems due to their ability to generate electricity with minimal greenhouse gas emissions. Among these technologies, solar photovoltaic (PV) energy has emerged as one of the fastest-growing renewable energy sources because of its abundance, scalability, declining installation costs, and continuous technological advancements.

Photovoltaic systems directly convert solar radiation into electrical energy through semiconductor devices known as solar cells. Owing to their reliability, modularity, and low maintenance requirements, PV systems are widely deployed in residential, commercial, industrial, and utility-scale applications. The rapid expansion of photovoltaic installations worldwide has significantly contributed to the diversification of energy resources and the achievement of global sustainability goals. However, ensuring the efficiency and long-term reliability of PV systems requires a comprehensive understanding of their operating principles, system components, electrical behavior, and mathematical models.

This chapter provides the theoretical foundation necessary for the remainder of this thesis. It begins by discussing the importance of renewable energy and the growing role of photovoltaic technology in the global energy transition. It then presents the main components of a photovoltaic system and explains their respective functions. Finally, the mathematical modeling of photovoltaic cells is introduced.

I.2 Importance of renewable energy

Renewable energy sources (RES) have become a cornerstone of the global transition toward sustainable energy systems. Derived from naturally replenished resources such as solar, wind, hydropower, biomass, geothermal, and ocean energy, RES provide a clean and sustainable alternative to fossil fuels while enhancing energy security and promoting long-term economic development [16].

The increasing deployment of renewable energy is largely attributed to its environmental benefits. Unlike conventional fossil-fuel-based power generation, renewable energy technologies produce little or no greenhouse gas (GHG) emissions during operation. Life-cycle assessments indicate that photovoltaic (PV) systems typically emit approximately 20–50 gCO_2-eq/kWh, which is an order of magnitude lower than coal-fired electricity generation, making PV technology an effective solution for climate change mitigation and supporting the objectives of the Paris Agreement [17].

Renewable resources are also abundant and widely distributed. Solar energy, in particular, represents the largest available renewable resource, as the solar radiation reaching the Earth's surface greatly exceeds the current global energy demand. This widespread availability enables countries to reduce dependence on imported fossil fuels, improve energy security, and expand electricity access, especially in remote and rural areas [18].

From an economic perspective, continuous technological advancements and large-scale manufacturing have substantially reduced the cost of renewable electricity. The levelized cost of electricity (LCOE) of utility-scale solar photovoltaic systems has declined by nearly 90% over the past two decades, making solar power one of the most cost-competitive technologies for new electricity generation worldwide [19].

In addition to its environmental and economic advantages, the renewable energy sector has become an important source of employment and industrial development. According to the International Renewable Energy Agency (IRENA), the renewable energy industry employed approximately 12.7 million people worldwide in 2021, with the solar photovoltaic sector accounting for the largest share of these jobs [20]. Consequently, renewable energy has become a key pillar of modern energy strategies, contributing simultaneously to environmental sustainability, energy independence, economic competitiveness, and sustainable development.

The share of renewable energy increased significantly from 23% in 2015 to 32% in 2024, reflecting the accelerating transition toward cleaner energy systems. Solar power exhibited the most rapid growth among renewable technologies, reaching 6.9% of global electricity generation in 2024, while wind power contributed 8.1% and hydropower remained the largest renewable source at 14.3%. Despite this progress, fossil fuels continued to dominate the global electricity mix, accounting for 59.1% of total generation in 2024. These trends demonstrate the increasing role of renewable energy, particularly photovoltaic technology, in the global energy transition while highlighting the continued need to expand renewable deployment to reduce dependence on fossil fuels [21]. As shown in figure I.1.

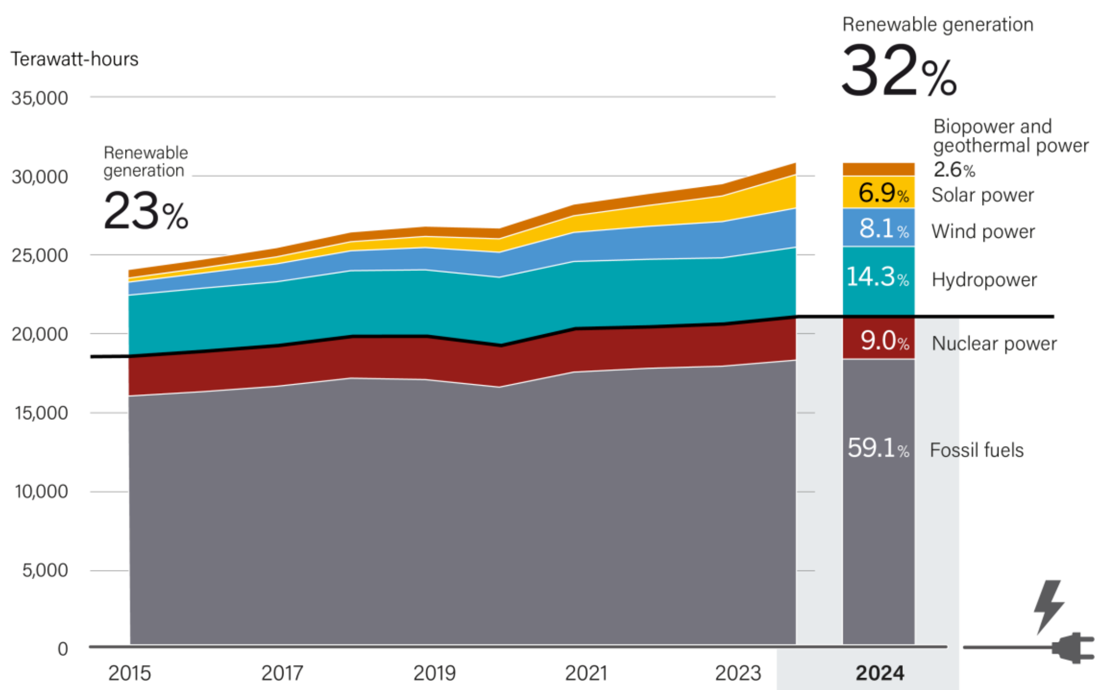

Figure I.1 Evolution worldwide cumulative electricity generation by energy Source, 2015-2024 [21].

I.3 Overview of photovoltaic technology

PV technology has become a key driver of the global transition toward clean and sustainable energy owing to the high reliability of PV systems [22] and the widespread availability of solar resources. The continuous expansion of installed PV capacity has also increased the importance of accurate PV power forecasting, which is essential for efficient power system operation, grid stability, and the effective integration of renewable energy sources. In recent years, the global photovoltaic market has experienced substantial growth, with the cumulative installed capacity reaching 1186 GW by the end of 2022 (figure I.2) [23]. This upward trend is expected to continue as countries accelerate the deployment of renewable energy technologies to reduce greenhouse gas emissions, decrease dependence on fossil fuels, and achieve their climate and energy objectives.

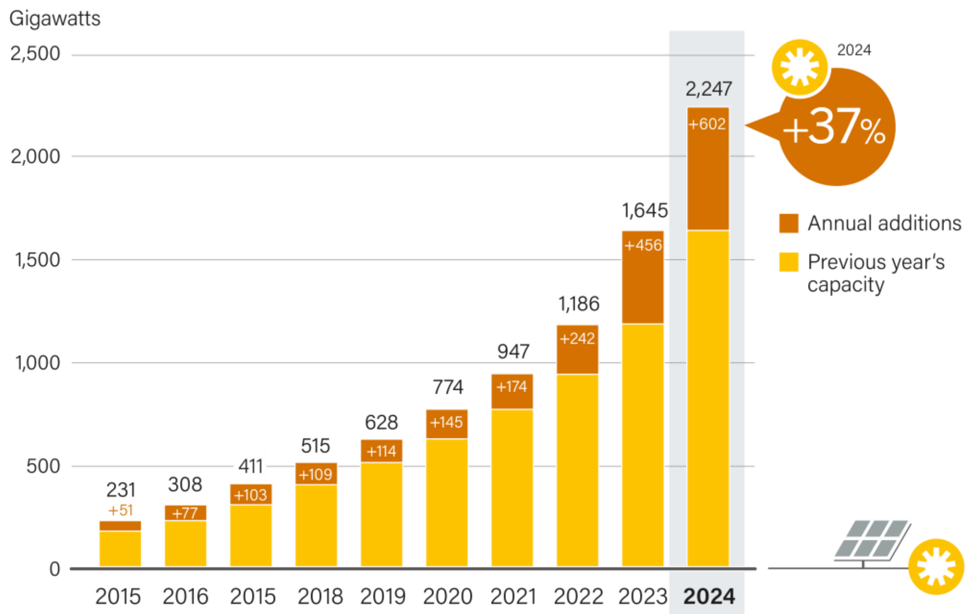

Figure I.2 Evolution of worldwide cumulative installed photovoltaic capacity [24].

I.4 Components of a photovoltaic system

A PV system is an integrated energy conversion system that transforms solar radiation into usable electrical power. Depending on the application, PV systems may operate as grid-connected, off-grid, or hybrid installations. Regardless of their configuration, all PV systems consist of several essential components that work together to ensure efficient energy generation, power conditioning, storage (when required), and electricity delivery.

I.4.1 Photovoltaic modules

Solar panels serve as the core power-generating unit of a photovoltaic system by layering distinct structural components together. At the center of this assembly is an array of interconnected solar cells, which are sandwiched directly between two layers of protective EVA encapsulant to shield them from environmental wear.

This core package is further secured by a durable back sheet on the bottom and a pane of high-transparency tempered glass on top, all rigidly bound together by a heavy-duty aluminium frame. External electrical connectivity is managed via the junction box mounted on the rear. Together, these structural layers ensure the module can safely generate power under varying weather conditions, though the final energy output remains dependent on external factors such as solar irradiance, cell operating temperature, panel orientation, and manufacturing design (such as high-efficiency monocrystalline silicon) [25].

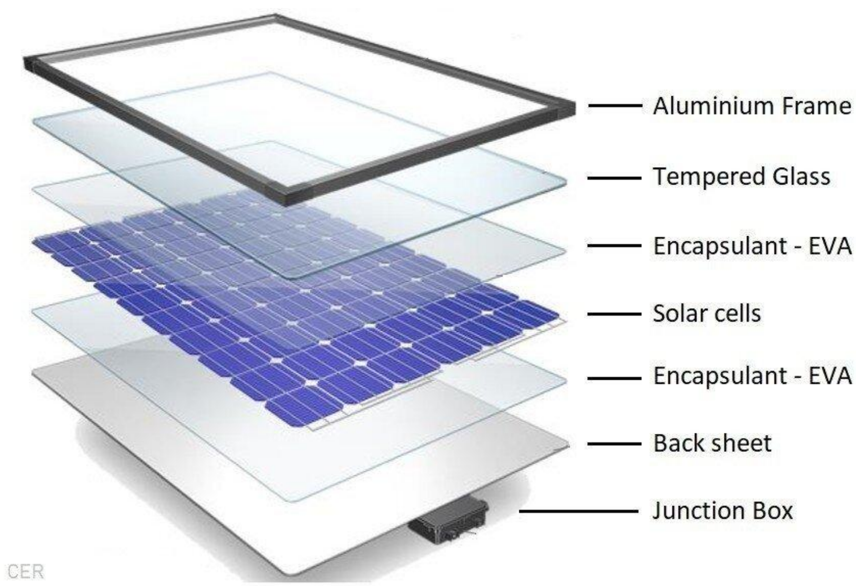

Figure I.3 Exploded view of a PV module structure and its components.

I.4.2 Mounting structure

The mounting structure provides mechanical support for PV modules while ensuring their optimal orientation and tilt angle to maximize solar energy capture. Mounting systems may be installed on rooftops, ground-mounted structures, or tracking systems that automatically follow the sun's movement. Proper structural design is essential for maintaining system reliability under wind, snow, and seismic loads while facilitating module cooling through adequate ventilation [26].

I.4.3 Inverter

The inverter is one of the most critical components of a photovoltaic system. It converts the direct current (DC) produced by the PV array into alternating current (AC) compatible with electrical loads and utility grids. In addition to power conversion, modern inverters perform several advanced functions, including Maximum Power Point Tracking (MPPT), grid synchronization, anti-islanding protection, fault monitoring, communication, and system diagnostics. Depending on the application, central, string, and microinverters may be employed [27].

Figure I.4 solar inverter

I.4.4 Maximum power point tracker

The output characteristics of photovoltaic modules vary continuously with solar irradiance and operating temperature. Consequently, PV systems incorporate MPPT algorithms to ensure that the modules operate at the voltage and current corresponding to the maximum available power. Widely used MPPT techniques include Perturb and Observe (P&O), Incremental Conductance (IncCond), Hill Climbing, Fuzzy Logic Control, and Artificial Neural Network-based methods [28].

I.4.5 Battery energy storage system

Battery Energy Storage Systems (BESS) are primarily used in off-grid and hybrid photovoltaic installations to store excess electrical energy generated during periods of high solar irradiance and supply power when solar production is insufficient. Lithium-ion batteries, particularly lithium iron phosphate ($LiFePO_4$), have become the preferred storage technology because of their high energy density, long cycle life, high efficiency, and low maintenance requirements [29].

Figure I.5 Solar batteries

I.4.6 Charge controller

A charge controller regulates the charging and discharging processes of the battery bank to prevent overcharging, deep discharge, and excessive current. It also improves battery lifespan and overall system reliability. Two main categories are widely employed: Pulse Width Modulation (PWM) controllers and MPPT charge controllers, with the latter providing higher energy harvesting efficiency [30].

Figure I.6 Solar charge controller

I.4.7 Electrical protection devices

Electrical protection equipment ensures the safe operation of photovoltaic systems under normal and fault conditions. Typical protection devices include DC and AC circuit breakers, fuses, surge protection devices (SPDs), disconnect switches, grounding systems, and lightning protection equipment. These components protect both personnel and equipment against short circuits, overloads, over voltages, and insulation failures [31].

I.4.8 Electrical cabling and connectors

Electrical cables transport the generated power between the PV modules, inverter, batteries, and electrical loads while minimizing transmission losses. PV cables are specifically designed to withstand prolonged exposure to ultraviolet radiation, humidity, and elevated temperatures. Standardized connectors, such as MC4 connectors, provide secure, weather-resistant electrical connections and facilitate installation and maintenance [32].

I.4.9 Monitoring and communication system

Modern photovoltaic installations incorporate monitoring systems that continuously measure electrical, environmental, and operational parameters, including voltage, current, power, energy yield, irradiance, and module temperature. These systems enable real-time performance assessment, fault detection, preventive maintenance, and remote operation through internet-based supervisory platforms. Monitoring has become increasingly important in large-scale PV plants where intelligent diagnostics and predictive maintenance significantly improve system availability [33].

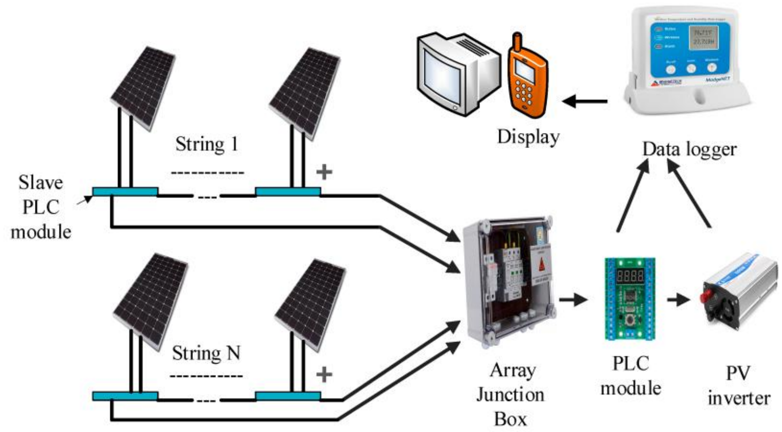

Figure I.7 Architecture of a solar PV monitoring system with PLC modules and data loggers.

I.5 Working principle of PV cells

A PV cell is the fundamental component of a solar energy conversion system, responsible for directly transforming solar radiation into electrical energy through the photovoltaic effect. Structurally, a PV cell consists of a p–n junction semiconductor, where the n-type layer contains an excess of free electrons introduced by donor impurities, while the p-type layer is characterized by the presence of holes generated by acceptor impurities. The interaction between these two semiconductor regions enables the generation of electrical current when exposed to sunlight. The basic structure of a photovoltaic cell is illustrated in Figure 1 [34].

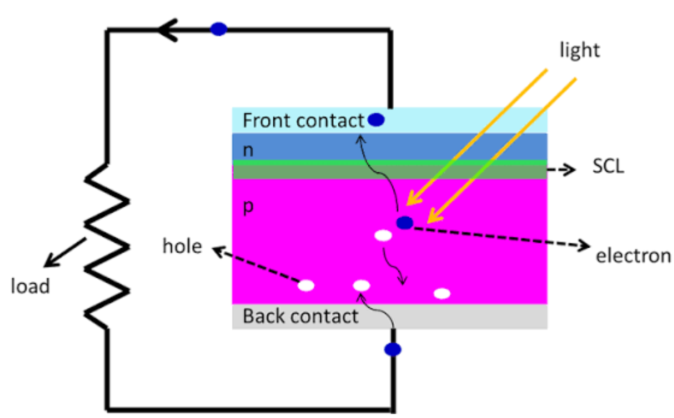

Figure I.8 P-N junction of a PV cell [35].

I.6 Solar cell mathematical model

The design and optimization of photovoltaic modules require accurate estimation of the internal parameters of solar cells using mathematical modeling. In practice, the electrical characteristics of a solar cell are typically described by equivalent diode-based circuit models.

I.6.1 Single diode model

The single diode model is one of the most widely adopted equivalent circuit models for representing the electrical behavior of photovoltaic cells because of its simplicity and satisfactory accuracy. In this model, the photovoltaic cell is described by a photocurrent source (I_{ph}) connected in parallel with a diode, which represents the p–n junction and accounts for the cell's nonlinear current voltage characteristics. To better match the behavior of a real solar cell, an ideality factor is introduced to compensate for deviations from the ideal diode characteristics. Owing to its relatively low computational complexity, the SD model is suitable for a broad range of simulation and performance analysis applications. Nevertheless, obtaining accurate values for its five unknown parameters remains a challenging task, as the model's predictive accuracy strongly depends on their proper estimation. The equivalent electrical circuit of the single-diode model is illustrated in Figure II.1 [36].

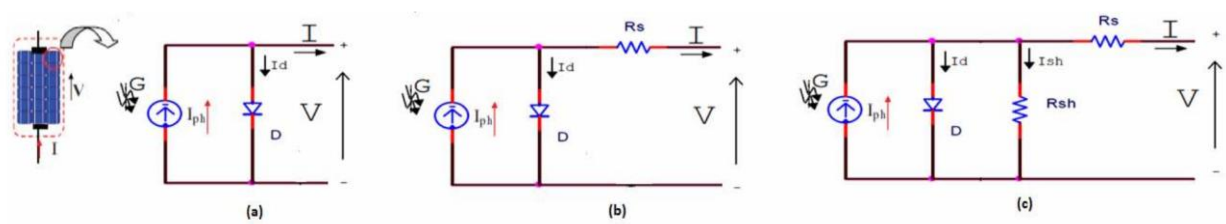

Figure I.9 Equivalent circuit model for single diode [37].

I.6.1.1 Ideal photovoltaic model

Figure II.2 (a) illustrates the equivalent circuit of the solar cell consists of a single diode connected in parallel with a light generated current source, from which the output current can be determined using the following equation [37]:

$$I = I_{ph} - I_s \left[exp\left(\frac{V}{nV_T}\right) - 1\right] \qquad (I\text{-}1)$$

where:

I_s = cell saturation of dark current,

V_T = thermal voltage = $\frac{kT_c}{q}$

k = Boltzmann's constant = 1.38×10^{-23} J/K

T_c = cell's working temperature

q = electron charge = 1.6×10^{-19} C

n = ideality factor = 1.1

I.6.1.2 Non-ideal photovoltaic models

a) Photovoltaic model with series resistance

The photovoltaic model incorporating a series resistance (R_s), illustrated in Figure II.2 (b), extends the basic equivalent circuit by accounting for internal resistive losses. Consequently, the output current can be expressed by the following equation [37]:

$$I = I_{ph} - I_s \left[exp\left(\frac{V+IR_s}{nV_T}\right) - I\right] \quad (I\text{-}2)$$

b) Photovoltaic model with series and parallel resistances

Although the model described by Equation (II-2) provides a simplified representation of a photovoltaic cell, it does not accurately capture the cell's electrical behavior under varying environmental conditions, particularly in the low-voltage operating region. To improve modeling accuracy, a more realistic equivalent circuit, illustrated in Figure II.2 (c), incorporates both a series resistance (R_s) and a shunt resistance (R_{sh}). The series resistance accounts for internal ohmic losses resulting from the semiconductor material, metal contacts, and interconnections, whereas the shunt resistance represents leakage currents caused by manufacturing imperfections and surface defects. In an ideal photovoltaic cell, the series resistance is assumed to be zero ($R_s = 0$), while the shunt resistance approaches infinity ($R_{sh} \to \infty$). By applying Kirchhoff's Current Law to the equivalent circuit, the output current of the photovoltaic cell can be expressed as follows [37]:

$$I = I_{ph} - I_d - I_{sh} \quad (I\text{-}3)$$

$$I = I_{ph} - I_s \left[exp\left(\frac{V+IR_s}{nV_T}\right) - 1\right] - \left[\frac{V+IR_s}{R_{sh}}\right] \quad (I\text{-}4)$$

Although mathematical models accurately describe the electrical behavior of photovoltaic cells under normal operating conditions, various defects and degradation mechanisms can significantly alter their performance. Faults such as cracks, short circuits, delamination, and contamination affect the I–V and P–V characteristics, resulting in reduced power output and efficiency. Therefore, early detection and diagnosis of these defects are essential for maintaining the reliability and performance of photovoltaic systems. This need has motivated the development of advanced inspection techniques, including aerial imaging and computer vision-based fault detection.

I.6.2 Double-diode equivalent circuit model

The equivalent circuit of the double-diode PV model is shown in Figure I.10. It comprises a series resistance (Rs) that represents Joule losses within the solar cell, a shunt resistance (Rp) that models leakage currents caused by manufacturing imperfections, a light-generated current source (IL), and two diodes ((D_1) and (D_2)) accounting for the diffusion and recombination current mechanisms, respectively.

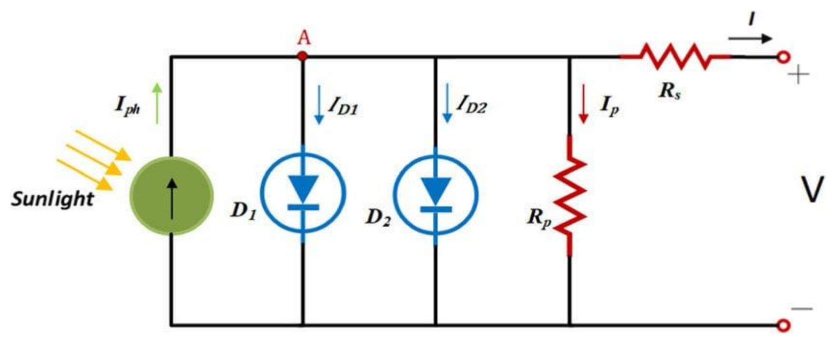

Figure I.10 Equivalent circuit of the double-diode PV model.

The I–V characteristic of a PV generator based on the double-diode model is expressed by the following equation:

$$I = I_L - I_{01}\left[exp\left(\frac{V+IR_S}{n_1 N_S V_{th}}\right) - 1\right] - I_{02}\left[exp\left(\frac{V+IR_S}{n_2 N_S V_{th}}\right) - 1\right] - G_p(V + IR_s) \qquad (I\text{-}5)$$

where:

- I is the output current of the PV generator (A);
- V is the output voltage of the PV generator (V);
- I_L is the light-generated (photocurrent) current (A);

- I_{01} and I_{02} are the reverse saturation currents of the first and second diodes, respectively (A);
- Rs is the series resistance (Ω);
- Rp is the shunt (parallel) resistance (Ω);
- n_1 and n_2 are the ideality factors of the first and second diodes, respectively;
- Ns is the number of cells connected in series;
- V_{th} is the thermal voltage, given by:

$$V_{th} = \frac{T \times k_B}{q} \tag{I-6}$$

Where K_B is the Boltzmann constant (1.380649 × 10^{-23} J/K), T is the absolute operating temperature of the PV generator (K), and q is the elementary charge (1.602176634 × 10^{-19} C). Finally, and G_p is the parallel admittance equals $1/R_p$.

I.7 Electrical characteristics of a photovoltaic cell

The electrical performance of a photovoltaic (PV) cell is primarily described by its current–voltage (I–V) and power–voltage (P–V) characteristics. These characteristics define the relationship between the output current, voltage, and power under specific operating conditions and provide valuable information for evaluating the efficiency and performance of photovoltaic systems. The shape of these curves is strongly influenced by solar irradiance, cell temperature, and the electrical properties of the semiconductor material [38].

I.7.1 Current–voltage (I–V) characteristics

The I–V characteristic represents the variation of the output current as a function of the terminal voltage. Under standard test conditions (STC), the current remains nearly constant over a wide voltage range before decreasing rapidly as the voltage approaches the open-circuit value. Two important operating points define the limits of the curve [39]:

- **Short-Circuit Current (ISC)**: The maximum current produced when the output terminals are short-circuited (V = 0). It is directly proportional to solar irradiance and only slightly affected by temperature.
- **Open-Circuit Voltage (VOC)**: The maximum voltage generated when no external load is connected (I = 0). Unlike the short-circuit current, the open-circuit voltage decreases significantly with increasing cell temperature.

Between these two points lies the operating region where the PV cell delivers electrical power.

I.7.2 Power–voltage (P–V) characteristics

The electrical power generated by a photovoltaic cell is given by:

$$P = V \times I \tag{I-7}$$

where P is the output power, V is the terminal voltage, and I is the output current.

The P–V curve exhibits a unique peak known as the Maximum Power Point (MPP), at which the product of voltage and current reaches its highest value. The voltage and current corresponding to this point are denoted by VMPP and IMPP, respectively. Since the location of the MPP varies with irradiance and temperature, photovoltaic systems employ MPPT algorithms to continuously operate near this optimum point [40].

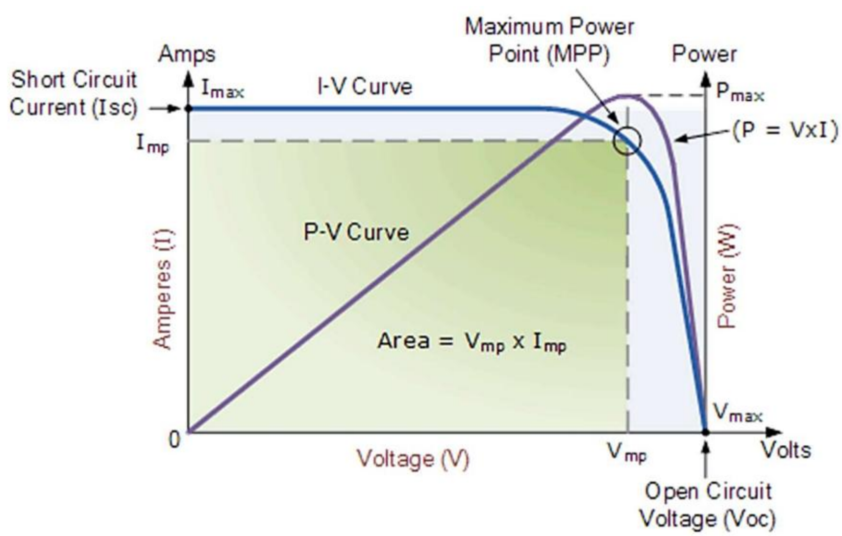

Figure I.11 A typical I-V and P-V curve of a solar cell

I.7.3 Fill factor

The Fill Factor (FF) is an important performance indicator that measures the quality of a photovoltaic cell. It is defined as the ratio between the maximum output power and the product of the open-circuit voltage and short-circuit current [41]:

$$FF = \frac{V_{MPP} I_{MPP}}{V_{OC} I_{SC}} \qquad (I\text{-}8)$$

A higher fill factor indicates lower internal losses and better electrical performance. Commercial crystalline silicon solar cells typically exhibit fill factor values between 0.70 and 0.85 [42].

I.7.4 Conversion efficiency

The conversion efficiency η represents the ability of a photovoltaic cell to convert incident solar energy into electrical energy. It is expressed as [43]:

$$\eta = \frac{P_{max}}{GA} \qquad (I\text{-}9)$$

where (P_{max}) is the maximum electrical output power, (G) is the incident solar irradiance (W/m²), and (A) is the active surface area of the photovoltaic cell.

Modern commercial monocrystalline silicon cells generally achieve efficiencies exceeding 22%, while laboratory prototypes have demonstrated efficiencies above 27% [43].

I.7.5 Effect of solar irradiance

Solar irradiance has a significant influence on the electrical characteristics of photovoltaic cells. As irradiance increases, the short-circuit current increases almost linearly, resulting in higher maximum output power. In contrast, the open-circuit voltage exhibits only a slight increase with increasing irradiance. Consequently, higher irradiance conditions lead to improved energy production [44].

I.7.6 Effect of temperature

Cell temperature mainly affects the voltage characteristics of photovoltaic cells. An increase in temperature causes a noticeable reduction in the open-circuit voltage and the maximum output power, whereas the short-circuit current increases only slightly. Therefore, elevated operating temperatures reduce the overall conversion efficiency of photovoltaic modules, emphasizing the importance of adequate cooling and ventilation [45].

I.8 Conclusion

This chapter presented the fundamental concepts of PV energy conversion systems. It discussed the importance of renewable energy and the growing role of photovoltaic technology, followed by an overview of the main components of a PV system. The chapter also introduced the mathematical models of photovoltaic cells and examined their electrical characteristics, including the current–voltage (I–V) and power–voltage (P–V) curves, as well as the influence of solar irradiance and temperature.

Despite their high reliability and long service life, photovoltaic systems are susceptible to various defects and degradation mechanisms that can reduce energy production, accelerate aging, and compromise system safety and reliability. Consequently, accurate and timely fault detection has become essential for improving system performance and extending the operational lifetime of PV installations.

To address these challenges, numerous fault diagnosis methods have been developed, ranging from conventional electrical and thermal analysis to advanced image-based and artificial intelligence techniques. The next chapter presents a comprehensive literature review of these approaches, highlighting the current state of the art, identifying existing research gaps, and establishing the scientific basis for the methodology proposed in this thesis.

Chapter II: Literature review

II.1 Introduction

Fault diagnosis within PV systems has traditionally relied on conventional inspection methodologies, primarily involving expert intervention coupled with thermal and electrical modeling [46]. These techniques focus on analyzing the instantaneous temperature profiles and power output characteristics of the panel to infer performance anomalies. However, these conventional approaches are often insufficient for accurately identifying or classifying subtle but critical defects such as cracking, severe hotspots, or micro-cracks at the SP or SC level. Consequently, advanced DL techniques have emerged as a superior and viable approach to precisely detect and classify these performance-limiting defects [47].

The integration of DL models for PV fault diagnosis is facilitated by non-destructive image acquisition methods. For system-level inspection, images of SP arrays are typically captured by Unmanned Aerial Vehicles equipped with thermal imaging cameras to identify large-scale thermal anomalies and hotspots [48]. For high-resolution component-level diagnosis, such as SC classification, the Electroluminescence EL imaging technique is employed. This process involves externally applying an electrical current to the SC, causing the emission of weak IR light. This light is then captured by specialized IR or EL cameras, generating image data used to train deep learning models, such as the Optimized YOLO variant, for intricate defect classification in SCs [49].

II.2 Background

This section provides a foundational understanding of the structural components of SC and SP, which is essential for contextualizing the subsequent review of defect detection and classification methodologies.

II.2.1 Solar photovoltaic panel

The SP is fundamentally constructed from a series-parallel array connection of individual SCs. The industrial standard incorporates several common cell array configurations, prominently the 60-cell, 72-cell, and 96-cell matrices, as illustrated in figure II.1. The 60-cell and 72-cell modules are standard choices for commercial and residential installations, generally producing between 160 Watts and 300 Watts at a nominal voltage of 36 Volts, contingent upon the specific cell technology [50].

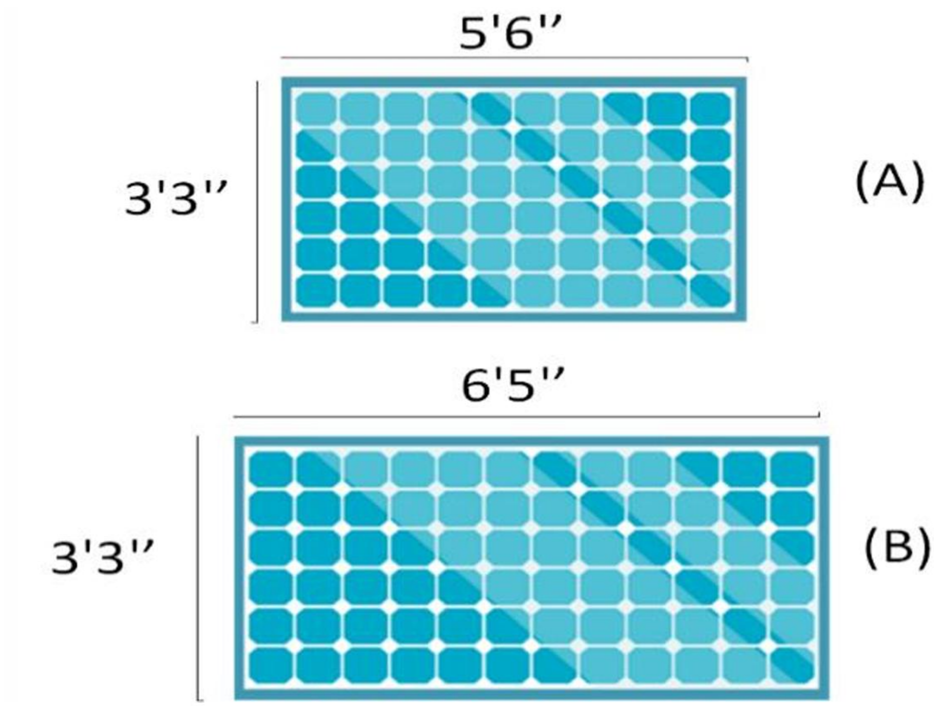

Figure II.1 Schematic illustration of standard solar panel configurations: (A) The 60-Cell (10x6) matrix and (B) The 72-Cell (12x6) matrix

The panel assembly is characterized by its protective layers: the front surface is typically encapsulated with durable tempered glass (or other highly transparent materials), while the back is protected by a waterproof, non-conductive backsheet. Crucially, the back of the panel houses the junction box, which facilitates the electrical connection between the internal SC circuitry and external wiring [51]. This box integrates bypass diodes, essential components that prevent the potentially damaging flow of reverse current and minimize power loss in scenarios involving partial shading or module obstruction, thus ensuring the safe and reliable operation of the PV system by protecting the wiring from environmental degradation [52].

The degradation of Solar Panels and the subsequent occurrence of defects are frequently initiated by exposure to adverse environmental conditions, such as strong wind, snow accumulation, and airborne dust or soiling. Although the origin of these defects is multifaceted, ranging from manufacturing flaws to errors during the installation process or persistent environmental stressors, the primary focus of this thesis is dedicated to the automated detection of the most common and performance-critical faults [53].

Specifically, this research focuses on the in-field detection and classification of hotspots, which are localized overheating regions that arise from current mismatch, partial shading, defective interconnections, or degraded solar cells. The physical mechanism responsible for hotspot formation is schematically illustrated in Figure II.2. In addition to hotspot defects, this study investigates other prevalent PV module faults, including soiling, characterized by the accumulation of dust, sand, bird droppings, or other contaminants on the module surface, and various forms of cracking, ranging from microcracks to severe cell fractures caused by manufacturing imperfections, mechanical stress, transportation, installation, or long-term environmental exposure. These defects are among the most frequently encountered in operating PV installations and can substantially reduce power output, accelerate module degradation, and compromise system reliability. To facilitate a structured understanding of their characteristics and origins, the considered PV defects are systematically categorized according to their source, namely manufacturing-related defects, installation-induced defects, and environmentally induced defects. This comprehensive classification, presented in Table II-1, provides the conceptual framework for the defect detection and classification tasks addressed by the deep learning models developed and evaluated throughout this thesis.

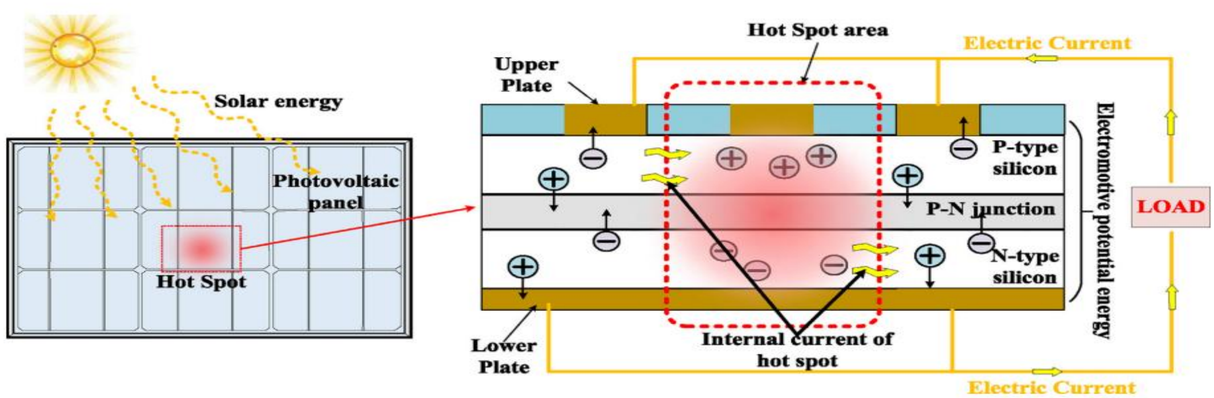

Figure II.2 Mechanistic diagram illustrating the process of hotspot formation in photovoltaic panels

***Table II-1** Classification of solar photovoltaic panel defects by etiology: manufacturer, environmental conditions, and installation/user issues*

No.	Defect Type	Possible Causes	Component Affected
1	**Hotspot [46]**	Exposure to extreme operational temperatures	Cells and Panels
2	**Broken Glass** [16]	High-velocity hail impact or other physical collisions	Panels
3	**Dust Build-up (Soiling) [54]**	Accumulation resulting from strong wind or high dust concentration	Panels
4	**Cracked Backsheets [54]**	Impact from collision or severe external environmental conditions	Panels
5	**Ribbon Discoloration [55]**	Material corrosion, prolonged exposure to heat, or moisture ingress	Panels
6	**Encapsulant Discoloration [56]**	Exposure to Ultraviolet (UV) light, high ambient temperature, and humidity	Panels
7	**Delamination [57]**	Concurrent issues arising from manufacturing, installation, and environmental exposure	Cells and Panels
8	**Bubbles [58]**	Insufficient heating during the lamination process, and the presence of moisture or contaminants	Panels
9	**Defective Junction Box** [17]	Malfunctions originating from faulty electrical connections within the box	Panels
10	**Poor String [59]Connection**	Deficiencies such as inadequate soldering, mechanical damage, or the presence of debris	Panels
11	**Potential Induced Degradation (PID) [52]**	Sustained exposure to hot temperatures combined with high humidity	Cells and Panels
12	**Back Contacts [60]**	Malfunctioning due to faulty electrical connections at the back contact point	Cells and Panels
13	**Corroded Components [61]**	Deterioration due to moisture or high humidity combined with extreme temperature	Cells and Panels
14	**Soiling [62, 63]**	Surface accumulation of dirt, dust, or various external particulate matter	Cells and Panels
15	**Multi-Defects [63]**	Concurrent faults arising from a combination of the listed possible causes	Cells and Panels
16	**Diode Defects [64]**	Operational or installation issues related to the bypass diodes	Panels

Degradation mechanisms in Photovoltaic systems frequently commence with failures in the panel's protective layers. For instance, Broken Glass [65] compromises the primary defense against environmental factors, potentially caused by hail or collisions, which consequently exposes the underlying cells to weather damage and severely impairs performance. Similarly, Dust Buildup (Soiling) constitutes a prevalent defect that attenuates solar radiation ingress, directly lowering the overall power output and efficiency. Furthermore, compromised backsheet integrity, evidenced by Cracked Backsheets, is critical, as it allows moisture and contaminants to penetrate the panel's structure, increasing the risk of corrosion and internal damage that affects system efficiency.

While the aforementioned defects represent a broad spectrum of Photovoltaic failures, the empirical focus of this research is specifically restricted to anomalies that are highly detectable using advanced computer vision techniques. The specific defects leveraged for model training in this work are Hotspot, Diode Defect, and Junction Defect. These data points were sourced from public dataset repositories and are analyzed under a simplified classification scheme where they are grouped into a binary class of defective and non-defective panels for rigorous object detection model training, consistent with the methodology employed for YOLO variant and Transformer development [67].

A solar cell is a photoelectric device that converts light energy directly into electrical energy through the photovoltaic effect. This phenomenon occurs when electromagnetic radiation generates a voltage and electric current within a semiconductor material. Solar cells can operate using either natural sunlight or artificial light sources. In addition to power generation, they can also function as photodetectors by sensing electromagnetic radiation, particularly in the near-visible spectrum [38].

The most common semiconducting material utilized in Solar Cell construction is silicon. A typical silicon Solar Cell is rated to produce approximately 0.5 Volts and 6.0 Amperes, yielding an equivalent power output of 3.0 Watts. These standardized electrical characteristics are cumulative: the required voltage and amperage for a complete Solar Panel such as the standard 60-cell or 72-cell configurations are achieved by electrically connecting multiple Solar Cells in series and parallel [68].

The integrity of these foundational components is vital, as Solar Cell defects directly propagate performance issues to the entire panel. In the context of this study, the detection of Solar Cell defects is critical, with the potential causes being primarily attributed to manufacturing issues, as comprehensively detailed in Table II-2 [69].

Table II-2 *Classification of solar cell defects by etiology: manufacturer, environmental conditions, and installation/user issues*

No.	Defect Type	Possible Causes	Component Affected
1	**Hotspot** [46]	Exposure to extreme thermal conditions	Cells and Panels
2	**Microcracks**	Flaws introduced during the manufacturing process or post-production.	Cells
3	**Cracked Cells**	Result of severe thermal stress or mechanical impact (collision)	Cells
4	**Snail Trails**	Consequence of mechanical stress or physical impact	Cells
5	**Delamination**	Concurrent issues stemming from fabrication errors and improper installation.	Cells and Panels
6	**Potential Induced Degradation (PID)**	Extended exposure to high temperature and relative humidity	Cells and Panels
7	**Back contacts**	Electrical discontinuity or faulty connection at the back contact point	Cells and Panels
8	**Edge Isolation**	Electrical shorting between front and back contacts of an individual SC	Cells
9	**Fingerprint** [70]	Residue from manufacturing or installation handling (often detected via Magnetic Field Imaging)	Cells
10	**Picker Print**	Manufacturing-related flaws in deposition technique, paste quality, or printing parameters	Cells
11	**Corroded**	Deterioration due to moisture, high humidity, or extreme thermal cycling	Cells and Panels

The detailed analysis of defects at the Solar Cell level reveals several critical failure modes. Hotspot defects [46] are triggered when a damaged or underperforming Solar Cell section experiences localized heating, often due to a bypass failure or increased resistance. This intense, localized heat can inflict secondary damage on adjacent cells and significantly accelerate the degradation of the entire Solar Panel performance [71]. The non-contact detection of hotspots is effectively achieved using thermal imaging, a technology employing infrared cameras to accurately map and measure these critical temperature variations across the Solar Panel surface [72].

Microcracks represent another class of cell-level defects. These minute cracks are typically sub-millimeter in size, making them invisible to the unaided eye. Despite their size, they compromise the electrical integrity of the Photovoltaic system, reducing both performance and efficiency. Microcracks are primarily introduced during the manufacturing process or post-production handling and installation. Their detection requires specialized non-destructive testing, such as electroluminescence imaging. More severe Cracked Cells directly lead to power output reduction, decreased durability, and are themselves a common precursor to the formation of detrimental hotspots [73].

Other common defects include Snail Trails, which are visually identifiable as dark, discolored lines traversing the Solar Cell surface [74]. Potential Induced Degradation (PID) is a critical phenomenon where a high voltage potential difference between the Solar Cell and the grounded panel frame causes significant power loss. This condition is frequently exacerbated by sustained exposure to high operational temperatures and humidity.

Electrical connectivity failures also constitute a significant source of defects:

- **Back contacts** are essential for current collection. Poor quality or inadequate connections at the back contacts of a cell can lead to reduced power output at both the Solar Cell and Solar Panel levels [75].

- **Edge isolation defects** occur when the process designed to electrically disconnect the front and back contacts near the Solar Cell edges is improperly executed. This failure to adequately isolate the contacts can result in internal short-circuiting, leading to reduced power output or catastrophic failure of the Solar Panel [76].

- **Fingerprint and picker print defects** are primarily attributable to manufacturing processes, resulting from issues related to deposition techniques, ink quality, or general handling [77].
- **Dark area defects** signify regions of electrical inactivity or weakened diode performance. This phenomenon is often characterized by voltage drops and a localized extension of low electroluminescence intensity, particularly in areas adjacent to an electrical shunt [78].

II.2.2 Approaches for detection and classification of defects in solar photovoltaic systems

The comprehensive diagnosis of faults within Photovoltaic systems is fundamentally a two-stage process. The first stage involves detecting the presence of an anomaly in a specific Solar Panel, while the second stage requires classifying the detected fault into its specific etiology, such as a hotspot, soiling, or cracking [79].

To facilitate reliable fault detection, a variety of Non-Destructive Testing or Non-Destructive Evaluation imaging modalities are employed. These techniques are essential because they permit the analysis of a sample without inducing structural damage or alteration, allowing for the component's continued use and repeated analysis, unlike destructive methods (e.g., X-ray crystallography or certain electron microscopy techniques) [80].

The key non-destructive imaging techniques used for Photovoltaic defect identification include:

- Electroluminescence Imaging (Solar Cell defects) [70]
- Infra-Red Thermal Imaging (Solar Panel defects) [70]
- Lock-in Thermal Imaging (Solar Panel defects) [81]
- Ultraviolet Imaging (Solar Panel defects) [82]
- Magnetic Field Imaging (Solar Panel defects) [83]
- Spectroscopic Diagnostic Techniques (Solar Panel defects) [84]

Infrared Thermal Imaging and Electroluminescence Imaging are the two pivotal methodologies informing the dataset collection and object detection development in this thesis.

Infrared Thermal Imaging is a non-contact, non-destructive technique that utilizes infrared radiation to generate a visual representation of the Solar Panel's surface temperature distribution [70]. By mapping these thermal profiles, Infrared Thermal Imaging is highly effective for identifying hotspots and other thermal anomalies that indicate resistance faults or localized power dissipation within the panel, making it a standard tool for field inspection. Figure II.3 (a) illustrates a typical Infrared Thermal image of a Solar Panel.

Electroluminescence Imaging is a powerful and commonly used non-destructive method for internal defect localization in Solar Cells. The technique involves flashing an external electrical current across the Solar Cell, which induces the emission of measurable near-infrared light. The resulting image intensity is directly proportional to the current flow [85]. This technique detects defects such as microcracks, delamination, shunts, and broken interconnections. Figure II.3(b) shows an electroluminescence (EL) image used for defect analysis. EL imaging is widely applied in both manufacturing and field inspection of photovoltaic modules.

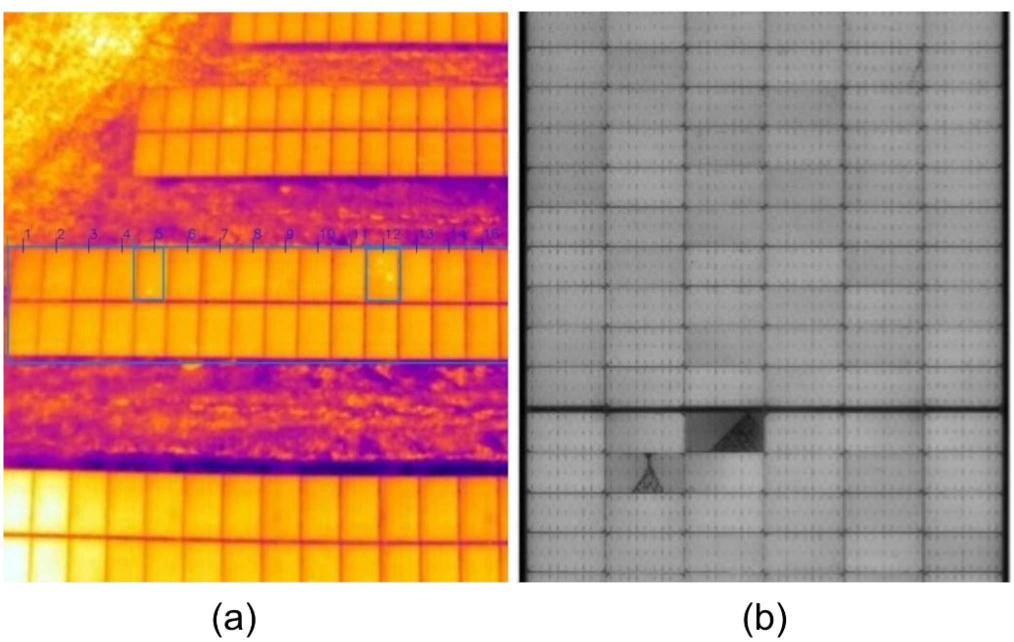

Figure II.3 Comparative visualization of non-destructive photovoltaic inspection techniques: (a) Infra-Red thermal (IRT) imaging and (b) electroluminescence (EL) imaging

Lock-in Thermal Imaging is another advanced, non-destructive, and non-contact thermal imaging technique widely applied for the identification of defects and failures within Solar Panels [81]. This technique is based on the principle of actively modulating light or heat input to induce a periodic thermal response within the panel's material. An infrared camera then captures the resulting thermal waves. The critical distinction of this method lies in the use of a lock-in amplifier to analyze the generated thermal signature, allowing it to isolate specific thermal waves at varying frequencies. This isolation process enables the high-resolution detection of localized defective areas within the Solar Panel.

Lock-in Thermal Imaging is particularly suitable for revealing concealed faults in modules or wafers, such as delamination, residual stresses, and shunts on the Solar Panel surface. While both Lock-in Thermal Imaging and Infrared Thermal Imaging are thermal detection techniques, they differ in their operational complexity and resolution capabilities [86]. Lock-in Thermal Imaging is considered an advanced approach capable of detecting defects and localized thermal variations with high resolution, as illustrated by its capacity to reveal a shunt defect in figure I. 4. Conversely, Infrared Thermal Imaging is more commonly deployed for detecting larger-scale faults on the Solar Panel, such as hotspots, by simply measuring the surface temperature variations [87].

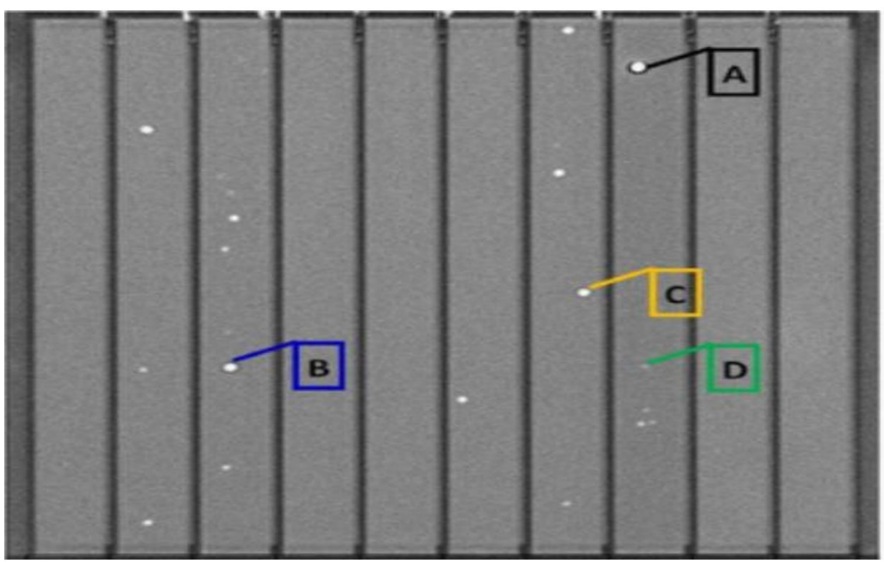

Figure II.4 Lock-in thermal (LIT) imaging technique for solar panel defect detection, illustrating shunt anomalies at points A, B, C, and D [87]

UV imaging is another non-destructive technique employed in SP diagnostics. This method detects defects such as internal cracks or delamination by identifying localized variations in the panel's surface fluorescence, rather than temperature. The technique involves exciting the panel sample with a high-energy UV light source, typically a UV LED, and capturing the resultant emission of fluorescent light with an imaging system [82]. UV imaging is capable of revealing microscopic faults, such as microcracks, that are not visible to the unaided eye. This capability makes it a valuable tool for quality control during manufacturing and for field inspection, enabling corrective actions that prevent damage propagation and sustain the SP’s energy output.

Magnetic Field Imaging (MFI) offers a distinct non-destructive diagnostic approach by analyzing the magnetic field induced by the electrical currents flowing within the SP [83]. This technique uses a magnetic field sensor placed on the panel surface to capture variations in the field generated by the internal circuitry. MFI can successfully identify defects like broken or poorly connected cells, which produce a weaker magnetic field signature compared to normally functioning cells.

Finally, Spectroscopic diagnostic techniques involve illuminating the SP surface and measuring the resulting radiation spectrum [84]. By analyzing the spectral data, defects can be identified and localized non-destructively. However, the adoption of these techniques is often constrained by the requirement for specialized equipment, technical expertise, and potential limitations regarding sensitivity and resolution.

It is important to note that no laboratory experiments or direct measurements using these techniques were performed in this research. Instead, this thesis utilizes the outputs of these non-destructive techniques specifically EL images applied to Solar Cells which were acquired and downloaded from various public data repositories, serving as the core input data for the subsequent classification stages.

Following the detection of potential anomalies via imaging, the crucial second stage is classification, which involves identifying and assigning the specific fault type to the detected region. The primary methodologies explored for this task include:

1. Deep Learning and Machine Learning
2. Adaptive Neuro-Fuzzy Inference Systems [88]
3. Digital Signal Processing (DSP) (e.g., Wavelet Transform and FFT) [89]

Deep Learning models have been extensively applied to the analysis of Solar Panel images for fault classification [33, 34], leading to significant increments in efficiency and performance. Due to their capacity to process massive datasets and improve performance through iterative learning, Deep Learning models have proven highly effective for tasks such as defect detection, degradation prediction, and operational optimization. The utilization of large datasets enhances classification accuracy by accounting for the diverse nature of field data. Consequently, sophisticated deep learning architectures such as YOLO variants and Transformer-based models are ideally suited for the classification and localization of defects in Solar Panels.

While other techniques exist, such as the ANFIS, which combines fuzzy logic with neural networks for prediction [88], they often face limitations. Although ANFIS has shown promise in classification, it can suffer from a loss of interpretability and a lack of scalability when dealing with the large, high-dimensional datasets common in modern PV diagnostics. Similarly, DSP techniques, which employ methods like Wavelet Transform and FFT for defect segmentation and classification [89], can be effective, particularly for segmenting linear defects like cracks, as conceptually shown in figure II.5. However, Deep Learning methods generally exhibit superior performance and adaptability for complex image-based classification tasks compared to these traditional approaches.

Therefore, this thesis adopts the use of Deep Learning models (YOLO variants and Transformers) as the exclusive and most advanced approach to classify and detect defects, prioritizing performance over the limitations associated with ANFIS and DSP techniques.

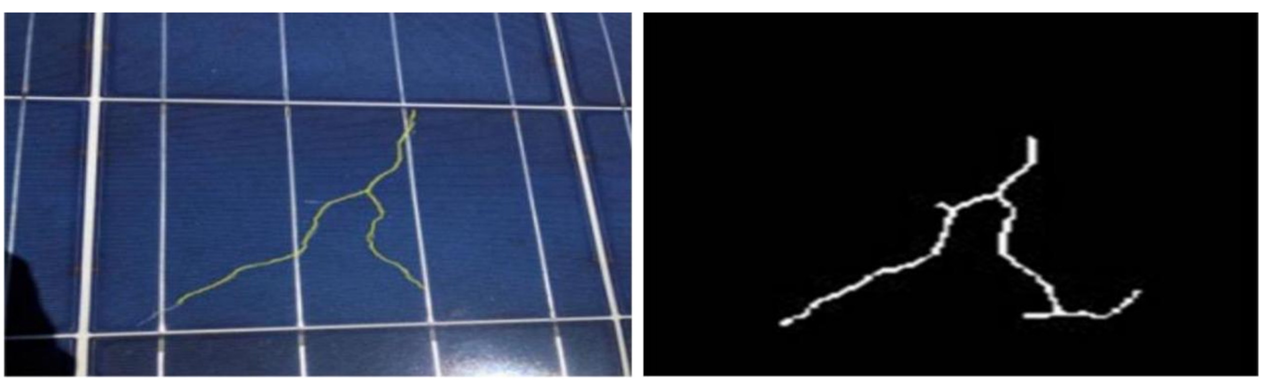

Figure II.5 Defect segmentation in solar panels utilizing digital signal processing: crack detection via wavelet transform and fast fourier transform (FFT) [89]

II.2.3 Quantitative performance evaluation metrics employed in photovoltaic literature

Performance metrics are defined as quantitative measures essential for assessing the efficacy and operational capabilities of a given system or process. In the context of this study, they serve to rigorously evaluate the deep learning models developed for defect detection within SCs datasets and SP images.

The scholarly literature establishes that model assessment relies on standardized metrics applicable to classification, segmentation, and object detection paradigms. Core classification performance metrics namely accuracy, F1 score, precision, and recall are typically reported using two distinct methods of aggregation: micro averaging and weighted averaging [90], as defined in subsequent equations (1-5).

- **Micro averaging** calculates the global average by aggregating statistical counts (such as true positives and false positives) across all samples and classes before computing the final metric.
- **Weighted averaging** first determines the metric score for each individual class, then computes a final average by adjusting the weight of each class score based on its frequency of occurrence within the ground truth data [91]. This approach ensures that performance on larger, more frequent classes proportionally influences the final reported score.

$$P = \left(\frac{TP}{TP+FP}\right) \tag{II-1}$$

$$R = \left(\frac{TP}{TP+FN}\right) \tag{II-2}$$

$$F1 = \left(\frac{2\times P\times R}{P+R}\right) \tag{II-3}$$

$$Accuracy = \frac{TP+TN}{TP+TN+FP+FN} \tag{II-4}$$

$$Balanced\ accuracy = \frac{Recall+specifity}{2} \tag{II-5}$$

Where specificity is $\frac{TN}{TN+FP}$, TP indicates that a specific class of defect is correctly identified as present in the test instance, while a TN represents the accurate identification of the absence of a specific defect. An error occurs with a FP, which is the incorrect assertion that a defect exists when it is, in fact, absent. Conversely, a FN occurs when the model mistakenly classifies a component as not having a specific type of defect, even though it is present in reality.

For segmentation tasks, the evaluation metrics commonly employed include mean accuracy and IoU, as defined in Equation (II-6). Mean accuracy measures the average pixel-level prediction correctness across all classes, accounting for both correct and incorrect classifications, thereby providing an overall assessment of model performance across the dataset. The IoU metric, on the other hand, quantifies the spatial correspondence between the predicted region or bounding box and the ground truth. It is computed as the ratio of the area of overlap between the predicted and actual regions to the total area covered by their union.

In the context of solar panel defect detection, primary performance metrics include precision, recall, mean average recall, and mean average precision. These metrics are typically evaluated at specific confidence thresholds or IoU ranges, such as mAP@50 or mAP@50–95, to assess both detection accuracy and the model's ability to correctly localize defects.

$$IoU\ (Segmentation) = \frac{TP}{TP+FP+FN} \qquad (II\text{-}6)$$

II.3 Literature review of solar cell and solar panel defect detection and classification

This thesis focuses on solar panel defect detection and solar cell defect classification. Unlike many existing approaches that rely on RGB images, it emphasizes the use of thermal imaging for solar panel defect detection. For solar cell classification, Machine Learning models analyze EL images, with the widely used Electroluminescence dataset serving as a common benchmark [92].

II.3.1 Solar panel defect detection

As part of this thesis, a comprehensive review of segmentation and object detection techniques for solar panel defect detection was conducted, with the main findings summarized in Table II-3. The review revealed that most previous studies relied on aerial RGB images for defect classification. However, accurate defect identification in photovoltaic power plants generally requires specialized imaging techniques, such as Electroluminescence (EL), Infrared Thermal (IR), Lock-in Thermal, Ultraviolet (UV), and Magnetic Field Imaging, before applying deep learning models [93]. This preliminary step is crucial for achieving better visibility and more precise defect localization.

For instance, a ResNet-34-based UNet segmentation model was employed in to identify potential defects on aerial rooftop images and analyze incoming solar radiation for optimal Solar Panel placement. This model demonstrated an accuracy of 77.0%. Similarly, [94] utilized a deep learning model combining EfficientNet-B7 and U-Net segmentation to accurately locate Solar Panel structures and measure their surface area from aerial satellite images obtained via the Static Application Programming Interface from Google Maps, achieving an IoU score of 86.0%. In a related effort, [95] created a Python software package for solar segmentation that relies on the Resnet-50 FPN model to analyze satellite images [96], resulting in a mean Average Precision (mAP) score of 77.8%.

In [97], a segmentation model based on the ResNet-34 UNet architecture, named RU-Net, was introduced for segmenting aerial remote sensing images, achieving an IoU score of 84.0%. Furthermore, [98] evaluated three distinct segmentation models U-Net, RefineNet, and DeepLab v3+ using satellite images with varying spatial resolutions of Solar Panels, where all models achieved mean IoU scores exceeding 85.0%. Likewise, [99] tested three segmentation models: U-Net, SegNet, and FCN on satellite RGB images, achieving classification accuracies of 94.7%, 94.1%, and 93.5%, respectively. By contrast, [100] employed alternative segmentation methods, including image enhancement, line-segment detection, and k-means clustering, to pinpoint Solar Panel regions in an infrared RGB image dataset. The synthesis of these methods led to a Solar Panel segmentation model, labeled SPS, which achieved an F1 score of 86.0%.

Table II-3 Summary of existing literature on segmentation and object detection techniques for solar panel analysis

Authors	Tasks	Model(s)	Dataset(s)	Results
Soares et al. [101]	Segmentation	ResNet-34-based UNet	Aerial RGB Images (Unavailable)	77.0% (Accuracy)
Parhar et al. [94]	Segmentation	EfficientNet-B7 based U-Net	Satellite RGB images from Google Maps	86.0% (IoU) and 92.0% (mean F1 Score)
Perry et al. [95]	Segmentation	Resnet-50 (FPN)	Aerial RGB image (Available)	77.8% (mean Average Precision)
Li et al. [42]	Segmentation	ResNet-34-based UNet	Remote sensing RGB images	84.0% (Intersection over Union)
Jiang et al. [44]	Segmentation	U-Net, RefineNet, DeepLab v3+	Satellite and aerial RGB dataset	>85.0% (mean Intersection over Union)
Sampath et al. [45]	Segmentation	U-Net, Seg-Net, FCN	Satellite RGB images (Unavailable)	94.7% (Acc, U-Net), 94.1% (Acc, Seg-Net), and 93.5%
Wang et al. [100]	Segmentation	Solar Panel Segmentation	Infra-Red RGB image (Unavailable)	86.0% (F1 Score)
Tommaso et al. [102]	Detection	YOLOv3	Infra-Red and Visible imaging by Drone	70.0% (mAP@0.5)
Tajwar et al. [103]	Detection	YOLOv3	Infra-Red Thermal images (Unavailable)	74.0% (Accuracy)
Zhu et al. [104]	Detection	TPH-YOLOv5	VisDrone2021, DET-test-challenge dataset	39.2% (mAP) for DET-test-challenge and 39.4% mAP
Pathak et al. [105]	Detection	Faster R-CNN	Infra-Red thermal Image (Unavailable)	67.0% (mAP)
Sun et al. [106]	Detection	YOLOv5	Infra-Red thermal Image (Unavailable)	87.8% (mean Average Precision), 89.0% (Average Recall), and 88.9% (F1 Score)

RGB satellite images are fundamentally unsuitable for accurately detecting and classifying Solar Panel defects due to their inherent lack of visibility regarding thermal and electrical anomalies [107]. This limitation necessitates the use of non-destructive detection techniques, such as Infrared Thermal and Lock-in Thermal imaging, before applying object detection models.

Several studies have integrated these specialized images with detection models. For example, [102] applied the YOLOv3 object detection architecture to analyze fused infrared and Red, Green, and Blue images acquired by an aerial platform after Infrared Thermal processing. In a related work, [103] utilized YOLOv3 exclusively on infrared images for hotspot defect detection and on Red, Green, and Blue images for other defect types, reporting a mean Average Precision at an Intersection over Union threshold of 0.5 of 70.0% and a hotspot detection confidence level of 74.0%. Moving toward advanced architectures, [104] proposed the TPH-YOLOv5 model, which enhanced the original YOLOv5 by integrating Transformer Prediction Heads. This model was evaluated on Red, Green, and Blue datasets from VisDrone [108] and the DET-test-challenge, achieving average precisions of 39.2% and 39.4%, respectively. Separately, the Faster R-CNN model, known for its effectiveness in edge detection, was applied to infrared thermal images for hotspot localization and achieved a mean Average Precision of 67.0% [105]. Furthermore, [106] proposed the AP-YOLOv5 variation by optimizing the anchor boxes and prediction heads, resulting in a mean Average Precision of 87.8%, an average recall of 89.0%, and an F1 score of 88.9% when tested on infrared thermal images.

II.3.2 Solar cell defects detection and classification

This section reviews major developments in PV defect detection, with particular emphasis on the evolution of YOLO-based methods and their relevance to current inspection practices. The objective is to situate the present work within ongoing research by summarizing notable advancements and persistent challenges in the field.

Imenes et al. [52] compared thermal imaging with multiwavelength composite images to enhance fault detection and classification in PV modules. Using YOLOv3 for its balance between computational load and detection performance, they combined thermal and visible-light imagery through convolutional neural networks to achieve an mAP of 0.75. While the approach reliably detected defects, differentiating specific fault types remained challenging, though the composite method had demonstrated utility in applications such as shadow detection [53].

Zou et al. [54] developed a drone-based inspection platform equipped with a FLIR DUO PRO R thermal camera, leveraging a 5G connection for real-time image transmission. Thermal images were analyzed using YOLOv4 implemented in Python, OpenCV, and Darknet. Among 1,000 collected images, 641 contained defects, and the system achieved an mAP of 1.0 at an 89% confidence threshold, demonstrating that high-quality PV inspection can be accomplished with cost-effective hardware and streamlined processing pipelines.

For EL imagery, Meng et al. [55] proposed YOLO-PV, an optimized YOLOv4 variant designed to capture fine defect structures. By modifying the backbone and incorporating a Spatial Pyramid Attention Network for improved feature fusion, the model reached an AP of 91.34% and inference speeds above 35 FPS, outperforming CSP-PV by 0.64% while reducing processing time by over a third. Additional data augmentation further increased accuracy to 94.55%, although the relationship between EL-detected defects and actual module performance was noted as requiring further study.

Li et al. [56] addressed the challenge of detecting small, visually similar defects through GBH-YOLOv5, which integrates Ghost Convolution, BottleneckCSP, and an additional prediction head. Using the PV-Multi-Defect dataset (1,108 images and 4,235 annotated defects), the model achieved an mAP of 97.8%, surpassing Fast R-CNN [57] by 27.8%. The increased architectural complexity led the authors to convert images to grayscale to reduce computation, although this approach may risk information loss, motivating future work on lightweight models capable of RGB processing for real-time deployment.

Hong et al. [58] combined visible and infrared imagery using a YOLOv5-ResNet framework for more efficient fault detection. A dual infrared camera system captured 3,000 images under controlled conditions, with data split into training, testing, and validation subsets. The model achieved 95% accuracy at 36 FPS, outperforming VGG (93%), demonstrating its practical value for PV maintenance environments.

Zhang et al. [59] adapted YOLOv5 for challenging solar cell defect detection by incorporating deformable convolutions, ECA-Net attention, and a dedicated prediction head for small defects. Coupled with Mosaic and MixUp augmentation and K-means++ anchor clustering, the modified network reached 89.64% mAP, improving 7.85% over standard YOLOv5 while maintaining 36.24 FPS.

To enhance speed without sacrificing accuracy, Zheng [60] developed S-YOLOv5, a lighter YOLOv5 variant employing adaptive scaling and normalization. Tested on UAV-acquired thermal images, it achieved an mAP of 98.1% at 49 FPS, outperforming contemporary detectors. Similarly, Hassan et al. [61] designed a custom CNN for automated PV inspection, integrating variable convolutional and pooling layers and achieving 98.07% validation accuracy. In a case study on PID, the system detected all defective modules with 96.6% precision, demonstrating strong potential as an alternative to manual inspection.

Cao et al. [62] extended YOLOv8 with YOLOv8-GD, incorporating Depthwise and Group-Shuffle Convolutions in the backbone and a BiFPN for enhanced feature extraction. This model achieved 92.8% mAP@0.5 and 63.1% mAP@0.5–0.95, improving over YOLOv8 by 4.2% and 5.7%, while reducing model size by 16.7%. Ghahremani et al. [63] evaluated YOLOv9–YOLOv11 on thermal and optical PV images, with YOLOv11-X delivering top performance (precision 89.7%, recall 87.7%, mAP 92.7%, F1 90%), outperforming classical approaches such as SVM and Faster R-CNN.

Wang et al. [64] proposed MRA-YOLOv8, integrating a Multi-branch Coordinate Attention Network and ResBlock module for improved feature extraction. Tested on the PVEL-AD dataset, the model reached 91.7% mAP@50, exceeding YOLOv8 by 3.1% and DETR by 16.1%, while exploring GAN-based synthetic data to address dataset imbalance. Xu et al. [65] enhanced YOLOv5 for photoluminescence images, integrating a C2f module, modified SPPF block, and augmentations (Mosaic, MixUp, HSV adjustments), achieving 91.5% mAP at 24.2 FPS, outperforming YOLOv7, YOLOv9, and Faster R-CNN.

Beyond YOLO, two-stage detectors remain relevant for tasks demanding high precision. Chen et al. [66] improved Faster R-CNN for EL images by adding a CBAM attention block and DIoU loss, achieving 87.14% mAP and outperforming YOLOv5 and SSD. Akram et al. [67] benchmarked multiple detectors, finding their optimized YOLOv9 variant achieved the highest mAP@0.5 (94.3%), while EfficientDet and DETR also performed competitively.

The reviewed literature shows that photovoltaic defect detection has advanced significantly with the development of deep learning-based object detectors. Single-stage models, particularly the YOLO family, offer an effective balance between detection accuracy and computational efficiency, making them suitable for real-time PV inspection. In contrast, two-stage detectors, such as Faster R-CNN, generally provide higher localization accuracy but require greater computational resources. Recent studies have focused on improving small-defect detection, multi-scale feature extraction, multimodal imaging, and lightweight architectures for edge deployment. However, challenges remain in distinguishing visually similar defects, ensuring robust performance under varying conditions, and achieving high accuracy with real-time efficiency. These limitations motivate the proposed methodology presented in this thesis, with its comparison to existing approaches summarized in Table II-4.

***Table II-4** Summary of state-of-the-art fault detection techniques utilizing YOLO*

Study	Model	Key Architectural Enhancements	Dataset	Performance Metric	Speed (FPS)
Li et al. [109]	GBH-YOLOV5	Ghost Convolution, BottleneckCSP, Extra Prediction Head	PV-Multi-Defect (1108 images)	97.8% mAP	–
Hong et al. [110]	YOLOV5 and ResNet	Infrared and Visible Image Fusion	3000 images (Hainan solar plant)	95% accuracy	36
Zhang et al. [111]	Enhanced YOLOV5	Deformable Convolution, ECA-Net Attention, Dedicated Small Defect Head	–	89.64% mAP	36.24
Zheng [112]	S-YOLOV5	Lightweight, Adaptive Scaling and Normalization	UAV Thermal IR dataset	98.1% mAP	49
Hassan et al. [113]	Custom CNN	Varying Convolutional and Pooling Layers	–	98.07% accuracy	–
Cao et al. [114]	YOLOV8-GD	Depthwise Convolution (DW-Conv), Group-Shuffle Convolution, Bi-directional Feature Pyramid Network	–	92.8% mAP@0.5,	–
Ghahremani et al. [115]	YOLOV11-X	Latest YOLO versions (v9, v10, v11), Multi-modal Input (Thermal & Optical)	Thermal and Optical images	92.7% mAP	–
Wang et al. [116]	MRA-YOLOV8	Multi-branch Coordinate Attention Network, ResBlock, Generative Adversarial Networks for augmentation	PVEL-AD	91.7% mAP@50	–
Xu et al. [117]	Upgraded YOLOV5	C2f, SPPF with Soft Pooling Augmentation	Photoluminescence (PL) images	91.5% mAP	24.2

II.4 Research gap and methodological contributions

The following highlights the limitations of the previous methodology for SP defects detection.

1. Over-reliance on Visual Spectrum RGB Imagery: A significant limitation in the literature has been the predominant application of deep learning models to SP defect detection using

standard visual (RGB) images. These models are restricted to identifying only visual-spectrum defects. This thesis, however, builds upon recent advancements that have shifted focus to more informative imaging modalities. Foundational work, such as the application of optimized YOLO models for EL images at the *cell level* (e.g., PV-YOLOv12n) and Transformer-based models for thermal images to detect *panel-level hotspots* (e.g., RT-DETR), has demonstrated the superiority of these data sources. Solar thermal images, for instance, provide invaluable data by capturing temperature variations and patterns indicative of performance issues, which are invisible in standard RGB imagery.

2. Lack of Methodological Standardization: This research gap highlights a systemic issue within the SP defect detection community, where different researchers or groups often use varying techniques, models, and datasets for similar tasks. This lack of standardization makes it challenging to compare and generalize results effectively. Foundational work, such as the direct comparison of RT-DETR vs YOLO v8, has begun to address this by providing clear benchmarks for specific tasks. This thesis aims to significantly expand this effort by creating a unified, comparative framework. As outlined in the thesis objectives, a core goal is to systematically evaluate the *comparative efficiency* of the best-in-class models from different architectures (e.g., optimized YOLO variants vs. Transformer-based detectors) on a standardized dataset for a *comprehensive* range of defects, thereby establishing a much-needed baseline for the field.

3. The Discrepancy in Dataset Scale for Deep Learning: One persistent challenge in the application of deep learning models to SP problems is the size and diversity of available datasets. Frequently, deep learning models require large-scale data for effective training and generalization. In the context of SP defect detection, many datasets available in the literature are relatively insignificant, leading to overfitting and hindering the models' ability to generalize to real-world scenarios. While previous studies have successfully used focused datasets (like PVEL-AD and Roboflow), this research work directly confronts the generalization problem. A key objective of this thesis is to validate the chosen model's viability for "practical, real-world implementation" and "high-throughput deployment" in "extensive commercial solar power installations," which necessitates a solution that is robust and generalizable beyond small, academic datasets.

4. Insufficient Focus on Model Improvement: Many research efforts in the field of deep learning for SP defect detection have focused primarily on *applying* existing, off-the-shelf models. This has led to a significant gap in terms of model improvement and innovation. This thesis, however, is grounded in a methodology of *active model optimization*. This approach is built upon prior work that, instead of merely applying models, *created* new, optimized architectures (e.g., PV-YOLOv12n with its A2C2f module) and *identified* superior architectures for specific tasks (e.g., RT-DETR for hotspots). This research work continues this focus by aiming to "develop and fine-tune an optimized YOLO model" to specifically enhance detection accuracy, thereby addressing the gap by prioritizing model refinement and innovation over simple application.

II.5 Conclusion

This chapter presented a comprehensive review of photovoltaic module defects and the principal fault diagnosis techniques reported in the literature. It discussed the origins, characteristics, and impacts of the most common PV defects, together with conventional monitoring approaches and recent advances in deep learning-based detection methods. A comparative analysis of state-of-the-art object detection models highlighted their strengths and remaining limitations, particularly in detecting small, low-contrast, and visually similar defects under real operating conditions. These observations establish the motivation for the proposed methodology presented in the following chapter, where an enhanced YOLOv12-based architecture is developed to achieve more accurate, robust, and efficient photovoltaic defect detection.

Chapter III: PV system faults detection techniques

III.1 Introduction

Significant advancements in the fault detection and diagnosis of PV modules have recently transformed system performance monitoring [118]. Much of this progress has been guided by technical benchmarks from the International Energy Agency (IEA), which outline advanced diagnostic methodologies for assessing PV health. In practice, operational PV panels face various degradation challenges, including dust accumulation (soiling), structural microcracks, encapsulation discoloration, and thermal hotspots; swiftly identifying these anomalies is essential for proactive maintenance and long-term reliability [119]. Fueled by expanding PV deployment and manufacturing capabilities across Europe, predictive maintenance has evolved toward highly precise, rapid fault detection workflows. These workflows generally follow two primary pathways: simulation-driven model-based analysis and data-driven automatic analysis. Key diagnostic tools feature spectral imaging techniques such as infrared thermography (IR-T) for thermal gradients, EL and PL for microstructural anomalies, and ultraviolet fluorescence (UV-F) for material degradation. These are often cross-referenced with environmental data (irradiance, temperature) and I-V curve profiling [120].

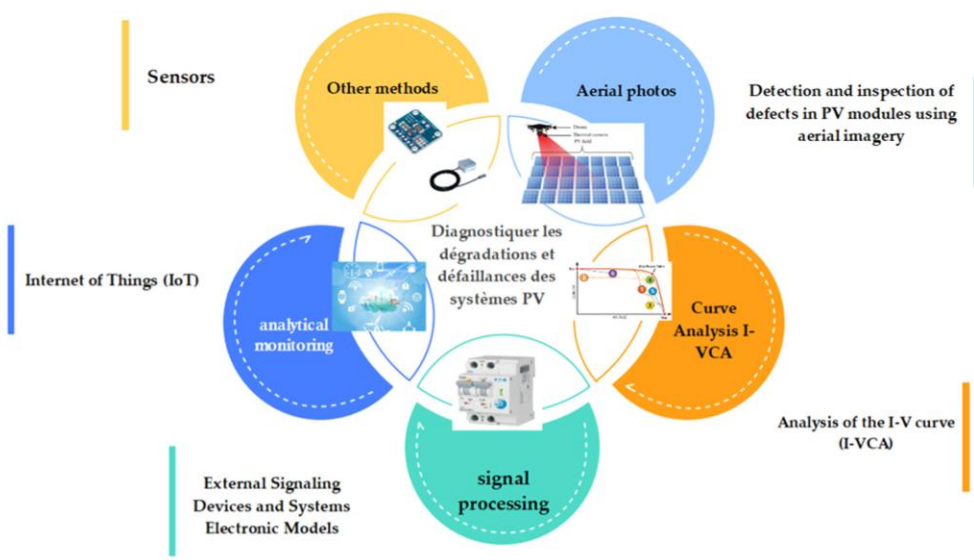

Figure III.1 Techniques for detecting common failures in PV systems.

III.2 Aerial detection and diagnosis of Faults in photovoltaic Modules

Visual inspection methods leveraging diverse imaging modalities offer a rapid, non-destructive approach to identifying failure modes, thereby safeguarding the overall safety and reliability of PV systems [121, 122]. These advanced techniques deliver high-resolution diagnostic imagery, often in real time. For instance, while thermal imaging characteristically isolates degradation anomalies through the detection of hotspots, it is important to note that not all localized module failures manifest as thermal overheating [123]. To address this limitation, complementary PV imaging techniques are deployed to uncover structural anomalies such as microcracks and severed finger grids that remain invisible to the naked eye during standard surface examinations. In field operations, visual and optical inspections are systematically performed before and after practical stress testing to benchmark degradation [52].

III.2.1 Principle of aerial inspection

The principle of aerial inspection consists of acquiring images of photovoltaic modules from an airborne platform and analyzing these images to identify defective regions. During inspection, the UAV follows a predefined flight path while capturing images at a constant altitude and speed. The acquired data are then transferred to a processing system where image enhancement, defect detection, and fault classification are performed.

III.2.2 UAV platform

The UAV serves as the carrier platform for the inspection sensors. Depending on the application, both multirotor and fixed-wing UAVs can be employed.

Multirotor UAVs are widely adopted because they provide excellent maneuverability, vertical takeoff and landing capabilities, and precise hovering over defective modules. In contrast, fixed-wing UAVs are more suitable for inspecting very large photovoltaic plants due to their longer flight endurance and higher coverage area.

III.2.3 Imaging sensors

The effectiveness of aerial inspection depends largely on the imaging sensor used. Two types of cameras are commonly employed:

- **RGB cameras**, which detect visible defects such as broken glass, heavy soiling, vegetation, and structural damage.
- **Infrared (IR) thermal cameras**, which detect temperature anomalies associated with electrical faults such as hotspots, bypass diode failures, and cell degradation.

Among these technologies, infrared thermography has become the preferred solution for field inspection because most photovoltaic defects generate localized thermal signatures, as shown in figure III.2.

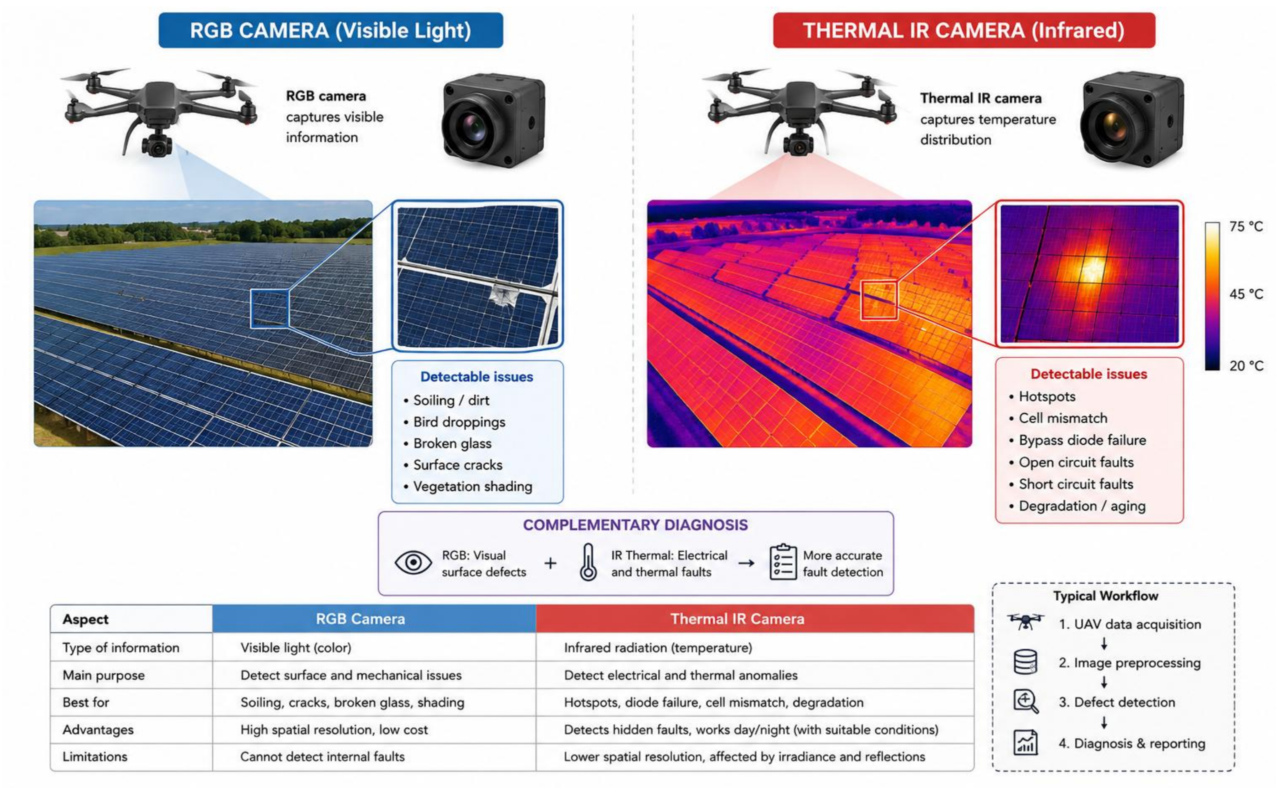

Figure III.2 RGB and infrared thermal cameras used in photovoltaic module inspection

III.2.4 Image acquisition procedure

The quality of the acquired images strongly influences the diagnostic performance. Several parameters should be considered during image acquisition:

- Flight altitude.
- Flight speed.

- Camera viewing angle.
- Image overlap.
- Solar irradiance.
- Ambient temperature.
- Wind conditions.

Careful planning of these parameters ensures complete coverage of the photovoltaic plant while maintaining sufficient image resolution for reliable fault detection.

III.2.5 Advantages of aerial inspection

Compared with conventional inspection methods, aerial inspection offers several advantages:

- Rapid inspection of large photovoltaic plants.
- Non-contact and non-destructive monitoring.
- Reduced labor and maintenance costs.
- High spatial resolution.
- Easy access to difficult or hazardous locations.
- Compatibility with automated image analysis algorithms.

III.2.6 Limitations of aerial inspection

Despite its effectiveness, aerial inspection also presents several limitations:

- Dependence on weather conditions.
- Limited UAV battery autonomy.
- Thermal measurements are influenced by irradiance and ambient temperature.
- Image quality decreases with excessive flight altitude.
- Aviation regulations may restrict UAV operations.

These limitations should be carefully considered when planning inspection missions.

III.2.7 Applications in photovoltaic fault diagnosis

Aerial inspection is widely employed to detect several types of photovoltaic faults, including:

- Hotspots.
- Cell mismatch.
- Defective bypass diodes.
- Open-circuit faults.
- Short-circuit faults.
- Soiling.
- Partial shading.
- String disconnections.

When combined with deep learning algorithms, aerial thermal images enable automatic localization and classification of these defects with high accuracy.

III.3 Current-voltage (I-V) curve analysis

A primary category of FDD methodologies for solar infrastructure involves the analysis of electrical characteristics. This approach facilitates continuous monitoring of the operational status of photovoltaic arrays by evaluating the I-V characteristics generated at both the individual cell and module string levels. These I-V curves serve as a critical diagnostic indicator of overall system health [124]. Consequently, any deviations or anomalies detected within the profile of these curves signal potential failure modes, including protective glass fractures, interconnection degradation, localized hotspots, or superficial defects [125].

III.3.1 Principle of I–V curve analysis

The I–V characteristic curve is obtained by varying the electrical load connected to the PV module while simultaneously measuring the corresponding output current and voltage. The resulting curve represents the electrical response of the module under a given irradiance and temperature.

A healthy PV module exhibits a characteristic nonlinear I–V curve with three important operating regions: the short-circuit condition, the open-circuit condition, and the maximum power point (MPP). Any deviation from the expected curve may indicate the presence of electrical or physical defects.

III.3.2 Key electrical parameters

Several electrical parameters extracted from the I–V curve are commonly used to evaluate the health of a photovoltaic module:

- **Short-circuit current (I_{SC}):** Maximum current delivered when the output voltage is zero.
- **Open-circuit voltage (V_{OC}):** Maximum voltage measured when no load is connected.
- **Maximum power point (MPP):** Operating point at which the product of current and voltage reaches its maximum value.
- **Fill factor (FF):** Indicator of the quality of the PV module, defined as the ratio between the maximum output power and the theoretical power obtained from (V_{OC}) and (I_{SC}).
- **Conversion efficiency (η):** Ratio of the electrical power generated to the incident solar power.

These parameters provide useful indicators for evaluating module degradation and identifying performance losses.

III.3.3 Fault detection using the I–V curve

Different faults affect the I–V characteristic in different ways. By comparing the measured curve with the expected reference curve, several types of defects can be identified.

Typical detectable faults include:

- Partial shading.
- Cell mismatch.
- Open-circuit faults.

- Short-circuit faults.
- Potential-Induced Degradation (PID).
- Module aging.
- Increased series resistance.
- Reduced shunt resistance.

For example, partial shading generally decreases the output current, while increased series resistance mainly reduces the fill factor and the maximum output power. Similarly, shunt resistance degradation causes a noticeable reduction in the output voltage and overall conversion efficiency.

III.3.4 Advantages of I–V curve analysis

The I–V curve analysis offers several advantages for photovoltaic fault diagnosis:

- Simple and well-established diagnostic technique.
- Non-destructive electrical testing.
- Capable of detecting multiple electrical faults.
- Provides quantitative performance indicators.
- Widely adopted in international PV testing standards.
- Suitable for periodic condition assessment.

III.3.5 Limitations

Despite its effectiveness, the I–V curve analysis has several limitations:

- Difficult to accurately localize the defective cell.
- Strongly influenced by irradiance and temperature variations.
- Measurements often require interruption of normal system operation.
- Less effective for detecting early-stage defects.
- Interpretation may require experienced personnel or advanced diagnostic algorithms.

III.3.6 Recent developments

Recent research has focused on integrating I–V curve analysis with artificial intelligence and machine learning techniques to improve diagnostic accuracy. Instead of relying solely on manual interpretation, extracted electrical parameters can be used as input features for classification algorithms capable of automatically identifying different fault types. In addition, real-time monitoring systems combined with Internet of Things (IoT) technologies enable continuous acquisition of I–V characteristics, allowing predictive maintenance and early fault detection in large-scale photovoltaic installations.

III.4 Signal processing methods

Signal processing methods constitute an important class of techniques for photovoltaic (PV) fault diagnosis by extracting meaningful information from electrical, thermal, or image data. Unlike conventional monitoring methods that rely solely on raw measurements, signal processing transforms the acquired data into representative features that facilitate the identification of abnormal operating conditions. These methods improve the detectability of faults by reducing measurement noise, enhancing signal quality, and emphasizing diagnostic characteristics.

A typical signal processing framework consists of several sequential stages, beginning with data acquisition from PV systems through electrical sensors or imaging devices. The acquired data are then preprocessed to remove noise and normalize the measurements before relevant features are extracted using mathematical and statistical techniques. These features are subsequently analyzed to identify patterns associated with healthy or faulty operating conditions, enabling the classification of different photovoltaic defects.

III.4.1 Principle of signal processing

The fundamental principle of signal processing is to transform raw measurements into representative features that can distinguish normal from faulty operating conditions. The input data may include current, voltage, power, temperature, infrared images, or electroluminescence images. After preprocessing, relevant features are extracted and analyzed using statistical or mathematical techniques to identify anomalies. The general workflow of signal processing for PV fault diagnosis is illustrated in Figure III.3.

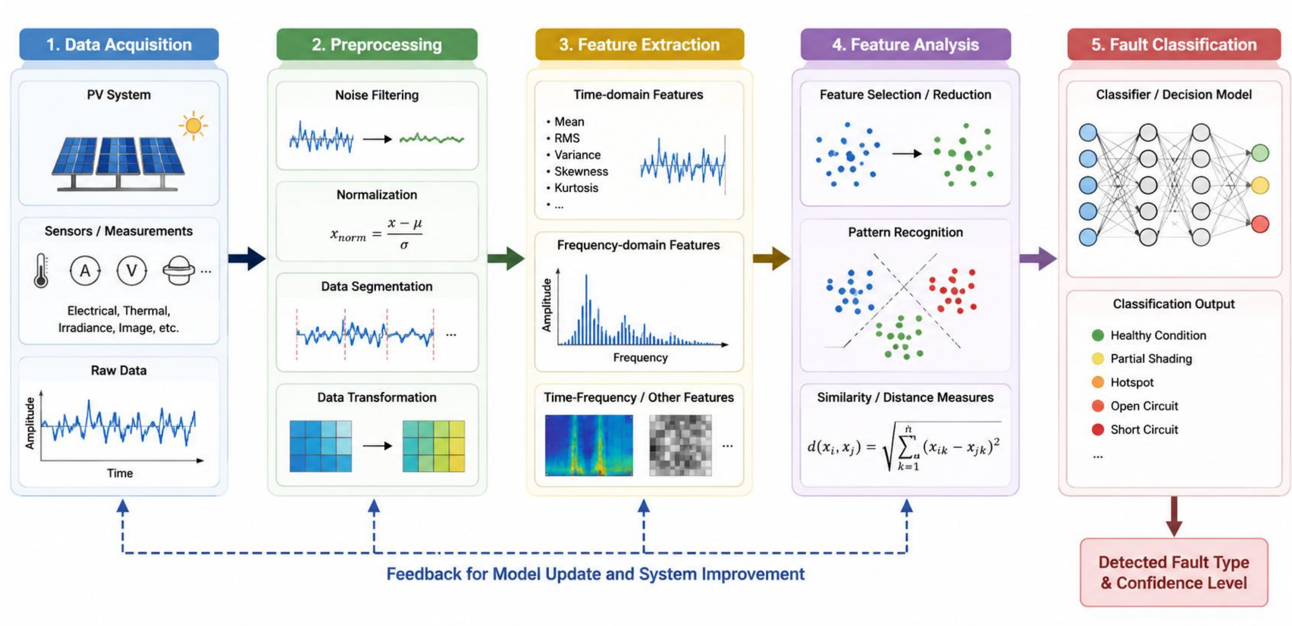

Figure III.3 General workflow of signal processing for PV fault diagnosis

III.4.2 Common signal processing techniques

Several signal processing techniques have been successfully applied to PV fault diagnosis, including:

- **Fourier transform (FT):** Used to analyze the frequency components of electrical signals and identify abnormal harmonic content caused by faults.
- **Wavelet transform (WT):** Provides simultaneous time-frequency analysis, making it suitable for detecting transient and localized faults.
- **Statistical analysis:** Employs statistical indicators such as mean, variance, skewness, kurtosis, and standard deviation to characterize signal variations.
- **Filtering techniques:** Reduce measurement noise while preserving useful diagnostic information.
- **Edge and texture analysis:** Applied mainly to thermal and electroluminescence images for identifying cracks, hotspots, and other structural defects.

III.4.3 Feature extraction

Feature extraction is one of the most important stages of signal processing. Instead of using raw signals directly, representative descriptors are calculated to simplify the diagnosis process.

Commonly extracted features include:

- Mean value.
- Root Mean Square (RMS).
- Peak value.
- Standard deviation.
- Entropy.
- Frequency spectrum.
- Texture descriptors.
- Histogram-based features.

These features improve the discrimination between healthy and defective photovoltaic modules.

III.4.4 Applications in PV fault diagnosis

Signal processing methods have been applied to detect various photovoltaic faults, including:

- Partial shading.
- Hotspots.
- Open-circuit faults.
- Short-circuit faults.
- Cell degradation.
- Module aging.
- Power fluctuations.

- Electrical noise anomalies.

These techniques are suitable for both electrical signal analysis and image-based inspection.

III.4.5 Advantages

Signal processing methods offer several advantages:

- Relatively low computational complexity.
- Fast implementation.
- Effective noise reduction.
- Applicable to different types of measured data.
- Easy integration with monitoring systems.
- Useful for feature extraction prior to machine learning.

III.4.6 Limitations

Despite their effectiveness, signal processing techniques have several limitations:

- Performance strongly depends on the selected features.
- Manual feature engineering requires expert knowledge.
- Reduced robustness under varying environmental conditions.
- Limited capability to represent highly complex fault patterns.
- Performance decreases when multiple defects occur simultaneously.

These limitations have encouraged the development of automatic feature learning approaches based on deep learning.

III.4.7 Recent developments

Recent studies combine traditional signal processing with machine learning and deep learning algorithms. Instead of manually selecting diagnostic features, signal processing is often used as a preprocessing step to enhance data quality before classification using convolutional neural networks (CNNs), object detection models, or transformer-based architectures. This hybrid approach improves both fault detection accuracy and computational efficiency.

III.5 Analytical monitoring methods

Analytical monitoring methods are model-based fault diagnosis techniques that detect abnormalities by comparing the actual operating behavior of a photovoltaic (PV) system with the response predicted by a mathematical model representing its fault-free operation. These approaches continuously monitor key electrical parameters, such as voltage, current, and power, under varying environmental conditions, enabling the identification of deviations associated with system faults. Unlike image-based inspection techniques, analytical monitoring does not require cameras or other visual sensing devices, as it relies exclusively on electrical measurements and mathematical modeling. Consequently, these methods enable continuous, non-invasive, and real-time supervision of PV system performance, making them particularly suitable for online condition monitoring. Their effectiveness depends largely on the accuracy of the underlying mathematical model and the robustness of the fault detection algorithm, both of which must account for environmental variations, measurement uncertainties, and parameter changes that occur during long-term system operation.

III.5.1 Principle of analytical monitoring

The fundamental principle of analytical monitoring is based on the development of a mathematical model capable of accurately representing the normal operating behavior of a photovoltaic (PV) system under varying environmental conditions. Such a model predicts key electrical parameters, including output voltage, current, and power, as functions of inputs such as solar irradiance and cell temperature. During system operation, these estimated values are continuously compared with the corresponding measurements acquired from the actual PV installation. Under fault-free conditions, the discrepancy between the predicted and measured responses remains within an acceptable tolerance determined by modeling and measurement uncertainties. However, when a fault occurs, this discrepancy increases significantly, indicating an abnormal system behavior.

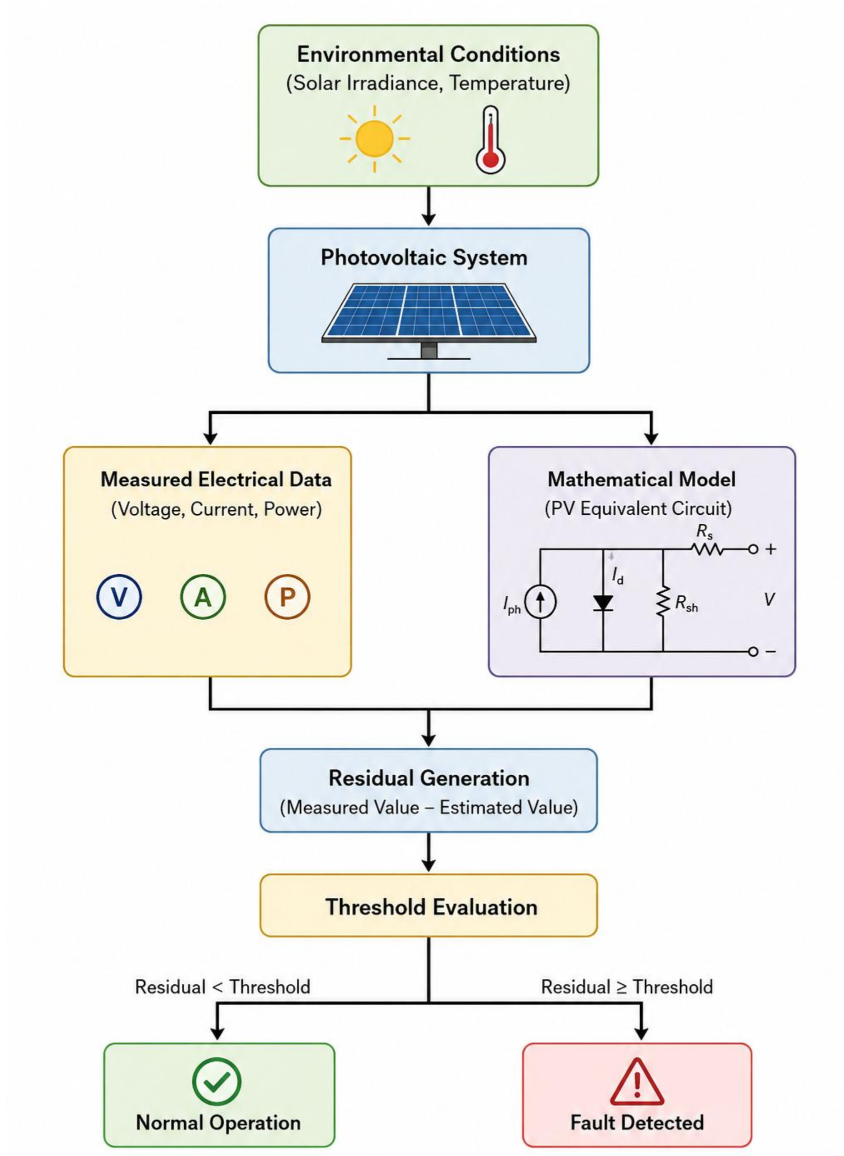

Figure III.4 General analytical monitoring framework for photovoltaic fault diagnosis

III.5.2 Mathematical modeling

The accuracy of analytical monitoring depends on the quality of the mathematical model used to represent the photovoltaic system. The most commonly employed models include:

- Single-Diode Model (SDM).
- Double-Diode Model (DDM).
- Five-Parameter Model.

- Equivalent Circuit Models.

These models estimate the electrical behavior of PV modules under different irradiance and temperature conditions, providing a reference for fault diagnosis.

III.5.3 Residual analysis

Residual analysis is one of the most widely used analytical diagnostic techniques. A residual is defined as the difference between the measured output and the value predicted by the mathematical model.

Under normal operating conditions, residual values remain close to zero. When faults occur, the residual exceeds a predefined threshold, indicating abnormal system behavior. The magnitude and evolution of the residual can also provide information about the severity of the fault.

III.5.4 Parameter estimation

Analytical monitoring often relies on estimating important photovoltaic parameters during system operation. Variations in these parameters may indicate module degradation or electrical faults.

Commonly estimated parameters include:

- Series resistance (Rs).
- Shunt resistance (Rsh).
- Photogenerated current.
- Diode saturation current.
- Ideality factor.

Monitoring the evolution of these parameters enables early detection of degradation mechanisms before significant power losses occur.

III.5.5 Applications in PV fault diagnosis

Analytical monitoring methods have been successfully applied to detect several photovoltaic faults, including:

- Open-circuit faults.
- Short-circuit faults.
- Module degradation.
- Partial shading.
- Potential-Induced Degradation (PID).
- Increased series resistance.
- Reduced shunt resistance.
- Power loss anomalies.

These methods are particularly useful for continuous performance monitoring in grid-connected photovoltaic systems.

III.5.6 Advantages

Analytical monitoring methods provide several advantages:

- Continuous online monitoring.
- Early fault detection.
- Non-destructive diagnosis.
- No imaging equipment required.
- Suitable for real-time performance assessment.
- Capable of identifying gradual degradation.

III.5.7 Limitations

Despite their advantages, analytical monitoring methods present several challenges:

- Dependence on accurate mathematical models.
- Sensitivity to parameter estimation errors.
- Reduced accuracy under rapidly changing weather conditions.

- Difficulty in distinguishing faults with similar electrical behavior.
- Limited capability for precise fault localization.

These limitations have encouraged researchers to combine analytical monitoring with artificial intelligence techniques to improve diagnostic accuracy.

III.5.8 Recent developments

Recent research has integrated analytical models with machine learning and digital twin technologies to enhance photovoltaic fault diagnosis. Model-based residuals are increasingly used as input features for intelligent classifiers, improving fault identification while reducing false alarm rates. Hybrid approaches that combine analytical monitoring with deep learning have demonstrated promising results for real-time monitoring of large-scale photovoltaic installations.

III.6 Conclusion

This chapter reviewed the main techniques used for photovoltaic (PV) fault detection, including aerial inspection, I–V curve analysis, signal processing methods, and analytical monitoring. These approaches provide effective solutions for monitoring PV systems and detecting electrical, thermal, and operational faults. However, each method presents specific limitations related to fault localization, environmental sensitivity, model accuracy, or the need for manual feature extraction. To overcome these limitations, recent research has increasingly adopted deep learning and computer vision techniques for automated PV fault diagnosis. These approaches enable accurate and efficient defect detection from aerial thermal images, making them particularly suitable for large-scale photovoltaic inspections. Therefore, the next chapter presents deep learning-based object detection methods for aerial photovoltaic fault diagnosis using infrared thermographic imagery.

Chapter IV: Comparative evaluation of RT-DETR and yolov8 for aerial photovoltaic panel defect detection

IV.1 Introduction

The assurance of continuous and optimal energy yield in PV systems necessitates the implementation of highly efficient, real-time defect detection capabilities. Among the various failure modes, hotspot detection via thermal infrared imagery is paramount, as elevated temperatures often signify critical defects such such as bypass diode failures, partial shading, or localized resistance issues that can lead to irreversible damage. This section, "Detection of Defects in Photovoltaic Panels," establishes a rigorous experimental framework to evaluate the performance of cutting-edge object detection paradigms specifically the RT-DETR and the established YOLOv8 architecture for the automated identification and localization of these thermal anomalies. The subsequent subsections detail the experimental design, which relies on a curated dataset of 1,015 annotated infrared images, and aims to answer a central research question: Does RT-DETR offer superior accuracy and real-time capability compared to YOLOv8 for the detection of PV hotspots? The comprehensive evaluation covers accuracy metrics, convergence stability analysis, and, crucially, computational efficiency, to determine the most viable model for deployment in resource-constrained, real-time field inspection systems.

IV.2 RT-DETR structure

As shown in Figure III 3, the RT-DETR model replaces the traditional ResNet backbone with HGNetv2, combining it with a hybrid encoder and a transformer decoder equipped with auxiliary prediction heads. The encoder accepts multi-scale feature maps extracted from the final three stages of the backbone (S_3, S_4, and S_5) and converts them into an image feature sequence via intra-scale interaction and cross-scale fusion. Subsequently, an IoU-aware query selection mechanism extracts a set number of these image features to serve as the initial object queries for the decoder. The decoder then iteratively updates these queries to generate the final bounding boxes and corresponding confidence scores.

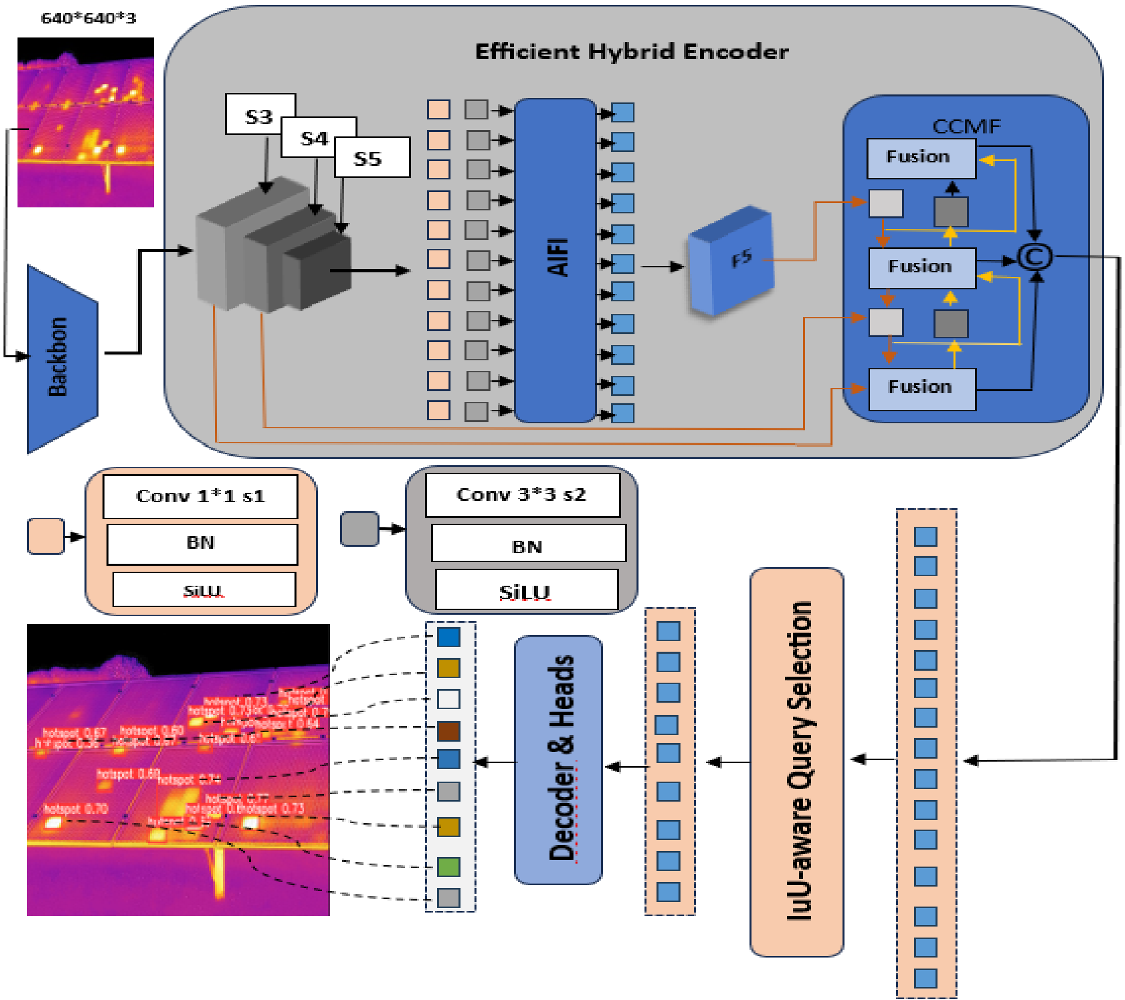

Figure IV.1 RT-DETR structure

IV.3 Hybrid encoder design

To optimize processing, the encoder structure was re-engineered into an Efficient Hybrid Encoder consisting of two main elements: the Attention-based Intrascale Feature Interaction (AIFI) module and the CNN-based Cross-scale Feature-fusion Module (CCFM). The AIFI module mitigates computational redundancy by limiting intra-scale self-attention exclusively to the S_5 layer. This strategy relies on the principle that self-attention applied to high-level, semantically rich features effectively captures relationships between conceptual entities, which is vital for subsequent object detection and recognition. Conversely, intra-scale interactions are omitted at lower levels, as they lack deep semantic content and risk introducing feature confusion and overlap with higher-level layers.

IV.3.1 IoU-Focused query system

The "IoU-aware query selection" mechanism guides the network during training to align high classification scores with features exhibiting high Intersection over Union (IoU) metrics, and lower classification scores with low-IoU features. Consequently, the top K encoder features selected based on classification performance yield bounding boxes that simultaneously display superior classification and precise localization. Integrating the IoU score into the objective function of the classification branch similar to VarifocalNet (VFL) ensures optimization alignment between the classification and localization of positive samples.

IV.4 Overview of the experiments

This chapter presents the experimental results obtained from evaluating the RT-DETR and comparing its performance against YOLOv8 for hotspot detection in PV panels. The experiments were designed to assess both detection accuracy and real-time capability when applied to thermal infrared imagery of PV modules.

The study utilized a curated dataset of 1,015 infrared images of PV panels, publicly available through Roboflow, with hotspot regions manually annotated using the CVAT platform. To ensure rigorous model evaluation, the dataset was partitioned following standard machine learning protocols, with separate subsets for training, validation, and testing, guaranteeing that the models were assessed on previously unseen data.

All experiments were conducted on an NVIDIA Quadro RTX 4080 GPU using Python 3.10.12 and PyTorch 2.1.0. Training parameters were standardized across both models to ensure a fair comparison: an input resolution of 640×640 pixels, batch size of 16, 200 epochs, and the AdamW optimizer with a learning rate of 0.002. These settings were selected to balance computational efficiency with stable convergence.

For benchmarking, five YOLOv8 variants (n, s, m, l, x) were initially evaluated, with YOLOv8-l achieving the highest performance. Consequently, this variant was chosen as the reference model for comparison with RT-DETR. Model performance was quantified using established object detection metrics, including precision, recall, F1 score, mAP, and inference time, enabling a comprehensive assessment of both accuracy and computational efficiency.

By integrating model-level performance measures, qualitative detection examples, and real-time processing analysis, the experiments aimed to answer a central research question of this thesis: Does RT-DETR offer superior accuracy and real-time capability compared to YOLOv8 for the detection of PV hotspots?

The remaining sections of this chapter provide detailed results, visualizations, and comparative discussion to address this question.

IV.5 Experimental results

The performance results of the five YOLOv8 configurations are summarized in table IV-1 [67]. Among these variants, YOLOv8-l achieved the highest mAP on the PV hotspot dataset and was therefore chosen as the baseline model for comparison with the proposed RT-DETR approach.

Table IV-1 *Performance results of the different YOLOv8 configurations [67].*

Model	mAP	Epochs completed
YOLOv8-n	0.635	230
YOLOv8-s	0.648	155
YOLOv8-m	0.651	126
YOLOv8-l	0.673	150
YOLOv8-x	0.661	120

IV.5.1 Loss curves

Figure III.2 and figure III.3 illustrate the evolution of the training and validation loss curves for the YOLOv8-l model and the proposed RT-DETR model, respectively. During training, YOLOv8-l shows a consistent reduction in its box, classification, and DFL losses, reaching low values by the end of the process. However, the validation losses display noticeable instability, marked by a sharp increase in the validation classification loss and a rising trend in the validation DFL loss. These irregularities indicate that YOLOv8-l may be overfitting to the occlusion-based training dataset.

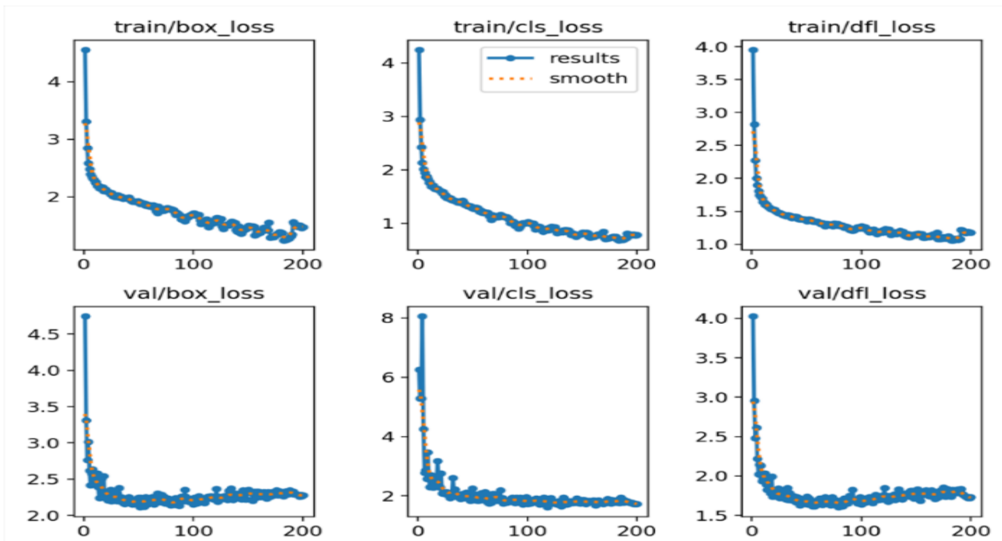

Figure IV.2 The loss curves of the initial YOLOv8 [67]

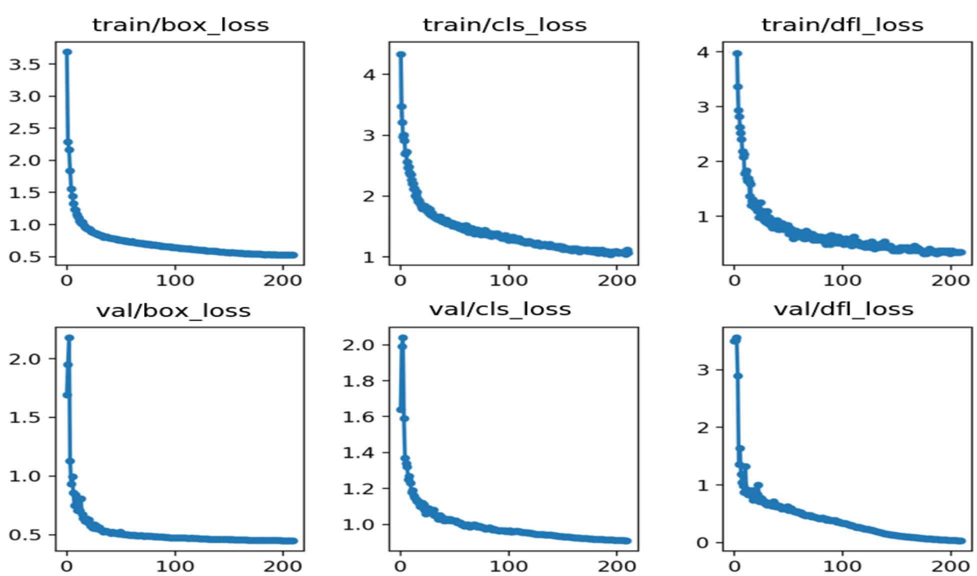

Figure IV.3 The loss curves of the RT-DETR [67]

- ❖ **Comparative Summary**

Convergence:
RT-DETR demonstrates stronger convergence behavior than YOLOv8-l, evidenced by its lower final training and validation loss values.

Stability:
The loss profiles of RT-DETR are noticeably smoother, indicating a more stable learning process. In contrast, the YOLOv8-l curves show considerable variability, reflecting less consistent optimization.

Overfitting:
RT-DETR shows no apparent signs of overfitting, as its validation losses decrease in parallel with the training losses. Conversely, YOLOv8-l exhibits elevated validation losses particularly in the classification component suggesting the possibility of overfitting to the training data.

Learning speed:

RT-DETR reaches effective learning more rapidly, with a sharp reduction in all loss metrics within the first 50 epochs. YOLOv8-l also improves during this period but does so with greater fluctuations and maintains higher loss values overall.

Generalization:
The validation loss patterns indicate that RT-DETR generalizes more effectively to unseen data compared to YOLOv8-l, reaffirming its robustness.

IV.5.2 F1–confidence curves

Figure III.4 shows that the YOLOv8-l model attains a maximum F1 score of 0.71 at a confidence threshold of around 0.327. Beyond this point, its performance gradually declines, indicating that the model’s optimal balance between precision and recall is confined to a relatively narrow confidence range. In contrast, Figure III.5 reveals that RT-DETR achieves a higher peak F1 score of 0.88 and maintains strong performance across a wider span of confidence values, with its optimal threshold occurring near 0.62. This broader stability suggests that RT-DETR preserves a more reliable precision–recall balance over varying decision thresholds.

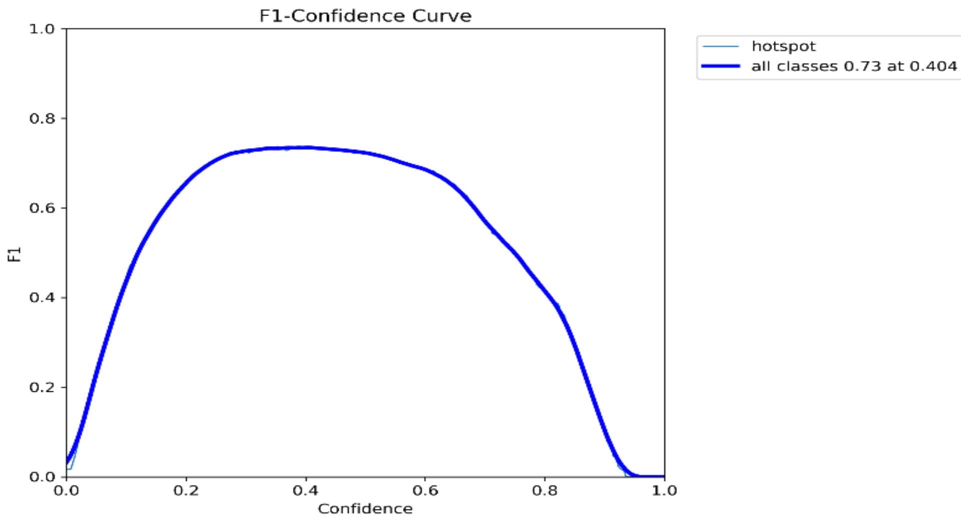

Figure IV.4 The F1–Confidence curves for YOLO v8-l [67]

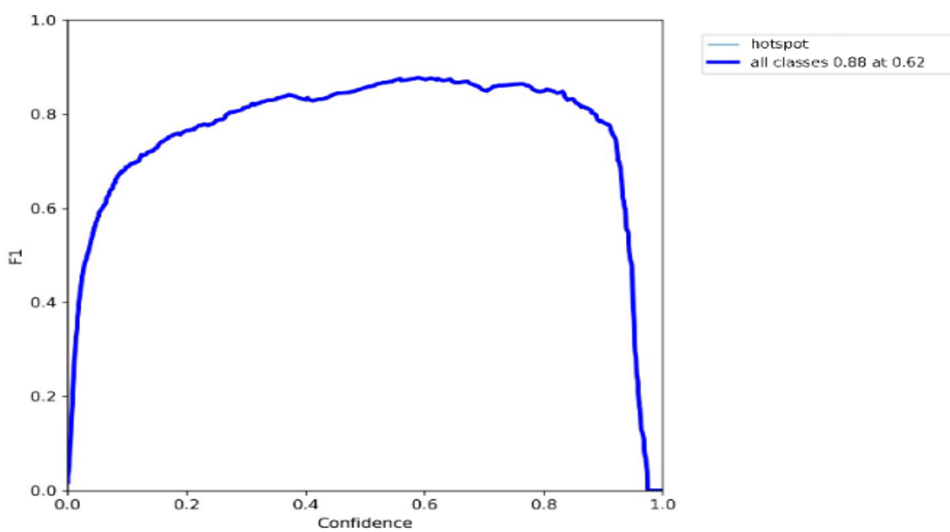

Figure IV.5 The F1–Confidence curves for RT-DETR [67]

IV.5.3 Comparative analysis of precision-recall curves

The P-R curve illustrated in figure III.6, which corresponds to the YOLOv8-l model, indicates a lower overall level of precision across most comparable recall thresholds. This is quantified by a mAP of 0.673 at an IoU threshold of 0.5. This result suggests that while the YOLOv8-l model successfully identifies a significant proportion of true positive samples (reasonable recall), it simultaneously exhibits a higher tendency toward generating False Positives when making predictions.

In sharp contrast, the second P-R curve, depicted in figure III.7, which represents the performance of the RT-DETR model, demonstrates a markedly higher and more sustained level of precision across a majority of the recall spectrum. This is substantiated by a superior mAP of 0.802 at an IoU threshold of 0.5. This metric confirms that the RT-DETR model achieves high precision when predicting a detection and is capable of correctly localizing a large proportion of all positive samples, maintaining its high performance until precision begins to drop sharply as the recall rate approaches unity.

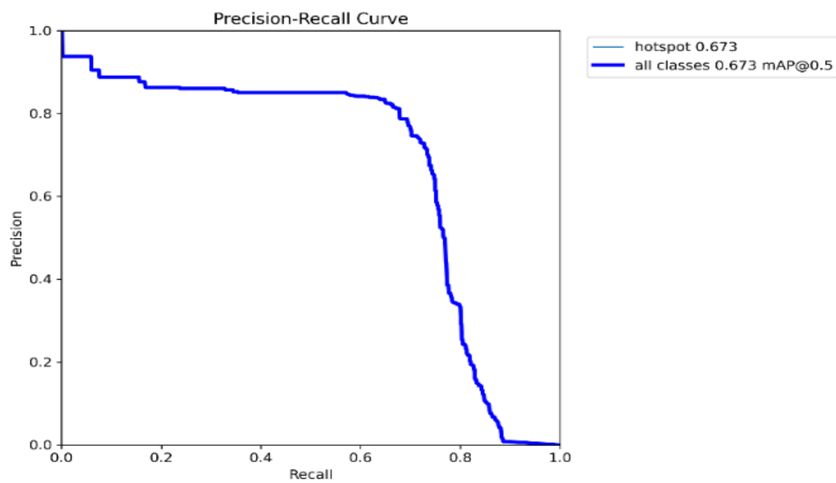

Figure IV.6 The P–R curves for the YOLO v8 [67]

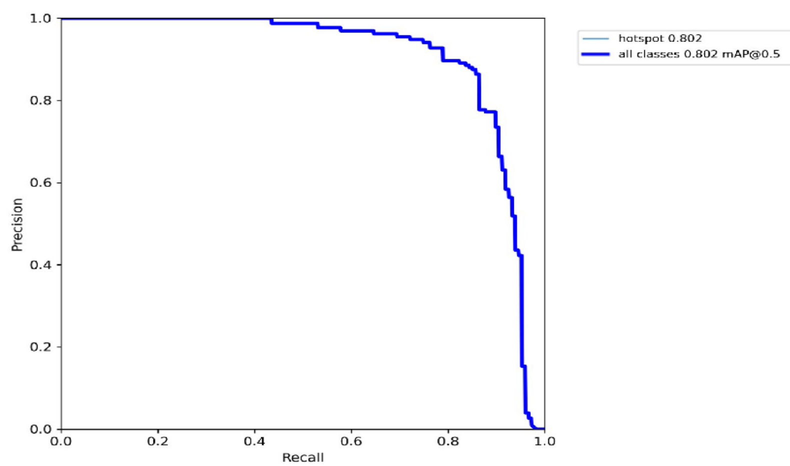

Figure IV.7 The P–R curves for the RT-DETR [67]

The RT-DETR model outperforms YOLOv8 by maintaining higher precision across almost the entire recall range. Its precision remains stable until a sharp decline at high recall, indicating consistently accurate predictions before reaching its detection limit. In contrast, YOLOv8 exhibits a gradual decrease in precision as recall increases, reflecting reduced prediction reliability when detecting a larger proportion of positive samples. These results demonstrate the superior precision and robustness of RT-DETR for photovoltaic hotspot detection.

IV.5.4 Detection effects

Figure III.8 provides a clear visual comparison between the YOLOv8 and the newly proposed RT-DETR models in their performance on thermal imagery of photovoltaic panels not previously encountered during training. These images are marked with bounding boxes and associated confidence scores that signify the detection of hotspots regions of elevated temperatures that often signal potential defects or performance issues within the panels.

The comparative analysis shows that YOLOv8 occasionally misses actual hotspots and incorrectly identifies non-hotspot regions as hotspots. In contrast, RT-DETR achieves more accurate hotspot detection, consistently producing high-confidence predictions without false hotspot identification. These qualitative observations agree with the quantitative results, demonstrating the superior reliability of RT-DETR for hotspot detection.

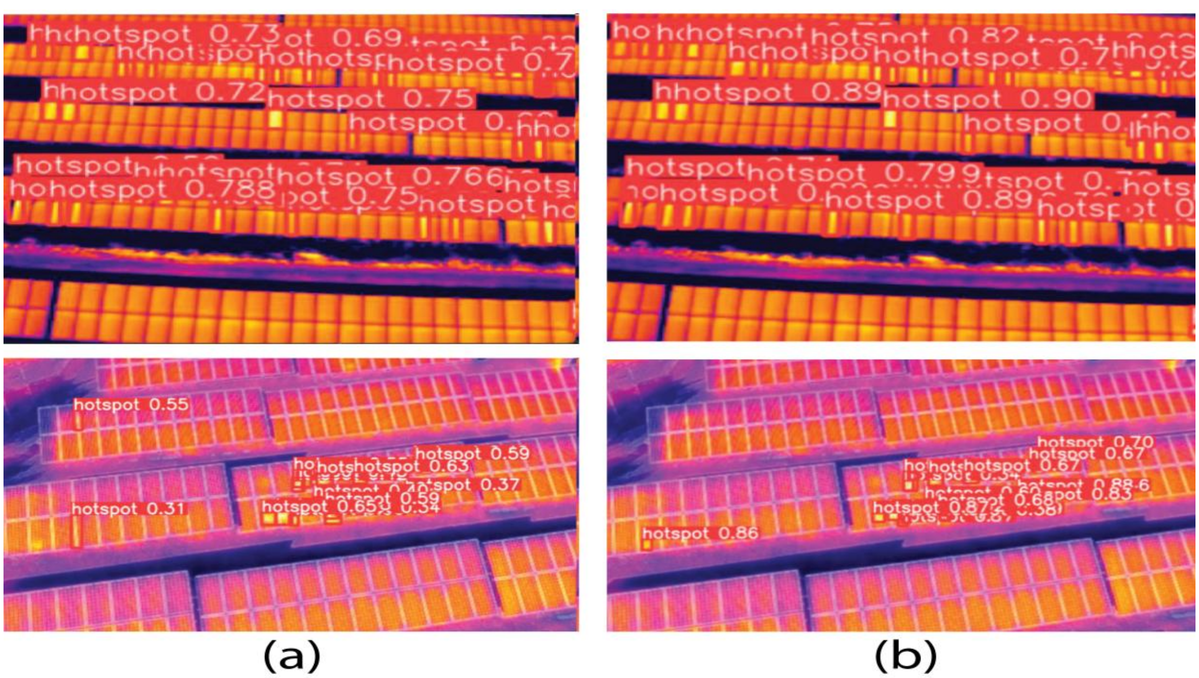

Figure IV.8 Qualitative comparison of defect detection effects between the baseline model (a) YOLOv8 and the proposed model (b) RT-DETR [67]

IV.5.5 Comparative analysis of computational efficiency and real-time detection capability

The analysis of processing speed is critical for determining the real-world viability of these models for deployment in field inspection systems, particularly on resource-constrained platforms. The RT-DETR model demonstrates a marginally superior total processing speed, achieving 884.4 milliseconds (ms) per image, which slightly edges out the YOLOv8-l model's time of 895.1 ms per image. This efficiency is paramount for achieving the real-time detection of Photovoltaic hotspots, facilitating an immediate response to mitigate damage and ensure optimal panel efficiency.

Furthermore, the RT-DETR model possesses a significantly lower computational requirement, quantified by only 32 million parameters and 110 Giga GFLOPs. This makes it substantially more viable for deployment in hardware-limited settings, such as drone-based systems used in solar farms. The model's higher frame rate of 114 FPS, compared to YOLOv8-l's 71 FPS, enables more frequent and effective monitoring of large solar installations, directly leading to faster hotspot detection. The comprehensive breakdown of the total processing times for both models, encompassing preprocessing, inference, and postprocessing, is presented in Table IV-2.

Table IV-2 *Comparative analysis of processing time for YOLOv8 and RT-DETR, including preprocessing, inference, and postprocessing stages [67]*

Model	Preprocess (ms)	Inference (ms)	postprocess (ms)
YOLOv8	3.1	891.1	1.0
RT-DETR	2.0	882.4	0.0

IV.5.6 Conclusion

The comparative evaluation conducted in this section unequivocally demonstrates the superior performance and robustness of the RT-DETR model for real-time PV hotspot detection via thermal infrared imagery. Through systematic analysis, RT-DETR exhibited stronger convergence stability and lower final loss values, avoiding the signs of overfitting that were apparent in the YOLOv8-l validation curves. Quantitatively, RT-DETR achieved a markedly higher mAP of 0.802 compared to YOLOv8-l's mAP of 0.673, confirming its capacity to maintain a more reliable balance between precision and recall across decision thresholds. Crucially, the model maintained a competitive processing speed (884.4 ms per image) while possessing a significantly leaner architecture (32 million parameters). This reduced computational requirement enables a higher frame rate (114 FPS) compared to YOLOv8-l's 71 FPS, solidifying RT-DETR's position as a more practical and highly scalable solution for immediate, on-site deployment in drone-based solar farm inspection systems. The findings affirm that the transformer-based detection paradigm offers tangible improvements in both detection accuracy and computational viability over traditional one-stage detectors in this critical application domain.

Chapter V: Enhanced YOLOv12-based framework for photovoltaic cell defect detection and classification

V.1 Introduction

The sustained operational efficiency and longevity of PV systems are critically dependent upon the timely and accurate identification of both structural and electrical anomalies. Moving beyond conventional, often error-prone manual inspections, this section outlines the advanced analytical framework developed for the precise detection and classification of defects in PV cells utilizing modern computer vision techniques. The goal is to establish a robust, quantitative methodology capable of categorizing multiple failure modes across diverse imaging conditions. This framework is specifically designed to leverage deep learning-based object detection, applying specialized architectural modifications to enhance feature extraction from critical inspection modalities, including high-resolution EL images and standard visible light (RGB) imagery. The following subsections detail the experimental foundation, including dataset characteristics and the proposed architectural optimizations, followed by the rigorous analysis of the model's performance in accurately locating and classifying the complex array of defects inherent to PV technology.

V.2 Dataset description and architecture modifications

This study relies on a robust experimental framework comprising two distinct datasets and a novel architectural optimization. This section details the characteristics of the EL imagery used for training, the statistical distribution of defects, and the specific enhancements introduced in the PV-YOLOv12n model.

V.2.1 Datasets for EL defect analysis

To ensure the model is capable of both high-precision feature extraction and real-world generalization, the analysis utilizes two specialized EL datasets: PVEL-AD and the Roboflow EL

Dataset. These datasets were selected to cover different scales of inspection from isolated cell morphology to full module integration.

V.2.1.1 PVEL-AD

The PVEL-AD dataset serves as the primary foundation for this research. It is a curated collection of high-resolution EL images focused specifically on individual solar cells.

- **Purpose:** This dataset provides the granular detail necessary for the model to learn the intricate morphological features of specific defects (e.g., the branching patterns of cracks or the intensity gradients of black cores) without the visual noise of a full panel background.
- **Defect Classes:** It includes a multi-class annotation set covering critical faults such as cracks, finger interruptions, and dislocations.
- **Dataset Split:** The available data were divided into three mutually exclusive subsets for model development and evaluation, with 70% allocated for training, 20% for validation, and the remaining 10% reserved for testing.

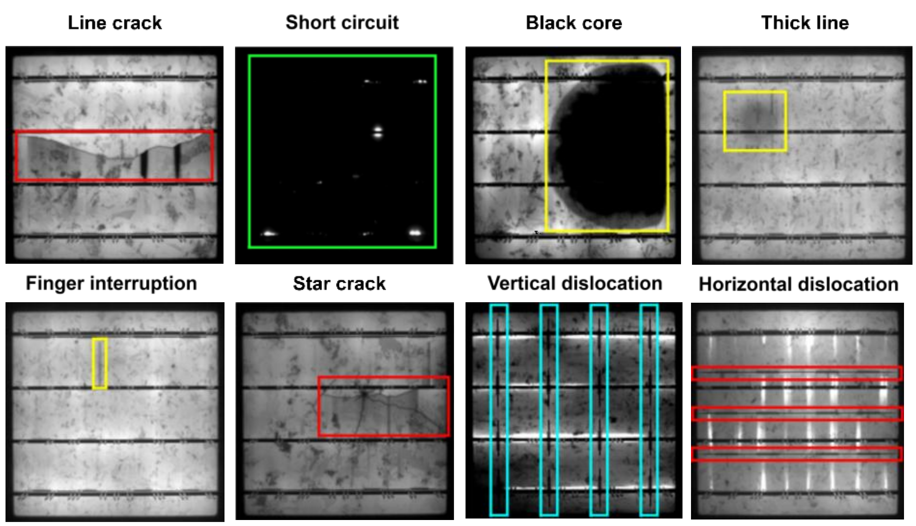

Figure V.1 Representative samples from the PVEL-AD dataset [15].

Figure V.1 displays isolated solar cells with clear annotations of specific defects, providing a noise-free environment for feature learning. The distribution of defect instances across the training, validation, and test sets is detailed in

Table **V-1**.

Table V-1 *Summary of instances across defect categories in the PVEL-AD dataset [15].*

Category	Train Instances	Val Instances	Test Instances	Total Instances
Black_core	1601	235	465	2301
Crack	1231	378	215	1824
Finger	2335	676	339	3350
Horizontal Dislocation	1474	424	201	2099
Short Circuit	1121	125	204	1450
Star Crack	36	201	15	252
Thick Line	1298	324	135	1757
Vertical Dislocation	166	48	26	240
Total Images	**3,912**	**1,118**	**559**	**5,589**

V.2.1.2 Roboflow EL dataset

To evaluate the robustness of the model, the Roboflow EL Dataset was utilized as a supplementary resource. Unlike PVEL-AD, this dataset consists of EL images capturing complete solar panels.

- **Purpose:** The inclusion of this dataset ensures that the model can generalize its detection capabilities from isolated cells to the more complex visual context of full panels, where grid lines, frame edges, and inter-cell spacing introduce realistic noise.
- **Dataset split:** Similar to PVEL-AD, this dataset followed a 70:20:10 distribution for robust training and evaluation[3].

Figure V.2 Representative samples from the Roboflow EL dataset [15].

Figure V.2 captures full solar panels, challenging the model to locate cell-level defects within a complex, multi-cell module context.

The statistical distribution of the four annotated classes in the Roboflow dataset is presented in Table V-2.

Table V-2 *Distribution of defect instances in the Roboflow EL dataset [15].*

Category	Train Instances	Val Instances	Test Instances	Total Instances
Cracked	4354	629	1250	6233
Panel (Non-defective)	3115	905	457	4477
Dusty	165	49	21	235
Bird Drop	40	14	6	60
Total Images	**4,545**	**1,298**	**650**	**6,493**

V.2.2 Data preprocessing and augmentation

To enhance the ability of the detection model to generalize across heterogeneous imaging conditions, a single, coherent data augmentation framework was adopted for both datasets. Applying a uniform augmentation policy helps mitigate the influence of variations stemming from acquisition settings, illumination differences, and environmental factors. The augmentation operations were organized into three categories: spatial transformations, photometric modifications, and occlusion-based perturbations.

Spatial augmentations, including mosaic composition, image flipping, scaling, and translation, were employed to improve robustness to positional and size variations. In photovoltaic inspection scenarios, defects such as micro-cracks, contamination, or structural irregularities may appear at arbitrary locations and scales. By deliberately altering the spatial configuration of training samples, the learning process is guided toward extracting defect-relevant features rather than memorizing fixed spatial patterns.

Photometric augmentation was implemented through controlled manipulation of hue, saturation, and intensity. For the RGB Roboflow dataset, these adjustments reproduce realistic changes in illumination, shadow distribution, and camera response. In contrast, for the grayscale PVEL-AD electroluminescence images, augmentation primarily targets intensity variations, effectively emulating differences in EL exposure levels and acquisition conditions. This strategy improves robustness to fluctuations in image quality and contrast.

To address partial visibility of defect regions, an occlusion-aware augmentation strategy based on Random Erasing was incorporated. In electroluminescence imagery, this operation approximates the visual masking introduced by metallic busbars or finger lines crossing the solar cell surface. For visible-spectrum images, it simulates common obstructions such as shadows or surface debris. By exposing the model to incomplete visual information during training, the network is encouraged to learn more distributed and resilient feature representations, enabling reliable detection even when defects are partially concealed.

The specific parameters adopted for these augmentation techniques are detailed in Table V-3.

Table V-3 *Configuration and impact of data augmentation techniques on electroluminescence (EL) and red, green, and blue (RGB) imagery [15].*

Augmentation	Parameters	Application Rate	Purpose	Impact on EL/RGB Images
Mosaic	mosaic=1.0	100%	Combines four images into one training sample.	Equally beneficial for both modalities.
HSV Adjustments	hsv_h=0.015, hsv_s=0.7, hsv_v=0.4	Per-image randomization	Modifies color properties (Hue, Saturation, Value).	RGB impacted; limited effect on EL (grayscale).
Horizontal Flip	fliplr=0.5	50%	Flips the image left-right.	Introduces orientation variability, useful for both.
Random Erasing	erasing=0.4	40%	Masks random image patches.	Simulates occlusions; helps prevent overfitting.
Translation	translate=0.1	Per-image randomization	Shifts image content by up to 10%.	Adds positional variance, enhancing location robustness.
Scaling	scale=0.5	Per-image randomization	Zooms (0.5x–1.5x).	Critical for multi-scale defects and small cracks in EL.

V.3 Proposed methodology

This section outlines the architectural framework of the proposed PV-YOLOv12n model. To overcome the challenges of background grid noise and subtle multi-scale anomalies in EL imagery, we introduce a lightweight feature extraction strategy combined with an optimized attention-driven layer aggregation mechanism.

V.3.1 Advanced computational core & light convolution

Traditional architectures rely on heavy convolutional operations that increase memory bottlenecks and slow down inference latency during real-time inspections. PV-YOLOv12n circumvents this by enforcing a high-parallelism, lightweight convolutional strategy in its early extraction layers.

Spatial feature mapping is distributed across sequences of smaller, localized kernels rather than treating global context in a single pass. The transformation mapping an input tensor F_{in} to an optimized output feature map F_{out} is formalized as:

$$F_{out} = \sum_{i=1}^{M} W_i * F_{in} + b_i \qquad (V\text{-}1)$$

Where:

- F_{in} and F_{out} represent the incoming and generated multi-channel feature tensors.
- W_i corresponds to the weight matrix of the localized i-th convolution block.
- b_i denotes the localized structural bias term.

By sequencing these smaller, decoupled operations, the model preserves critical spatial details for fine-grained defect footprints (such as micro-cracks or finger interruptions) while maintaining low computational complexity.

V.3.2 Optimized A2C2f module block

The defining architectural breakthrough of this study centers on the configuration of the network at the deep P5 semantic scale (Layer 20). Standard configurations employ a convolution-heavy, bottleneck-centric $C3k2$ block at this junction. In our proposed network, this is substituted with an $A2C2f$ block.

To enhance feature extraction and capture complex geometric defect shapes in EL images, the module splits the incoming feature map into parallel streams, allowing for multi-scale property aggregation simultaneously. The detailed internal architecture and multi-branch layout of this module are visually illustrated in Figure V. 3.

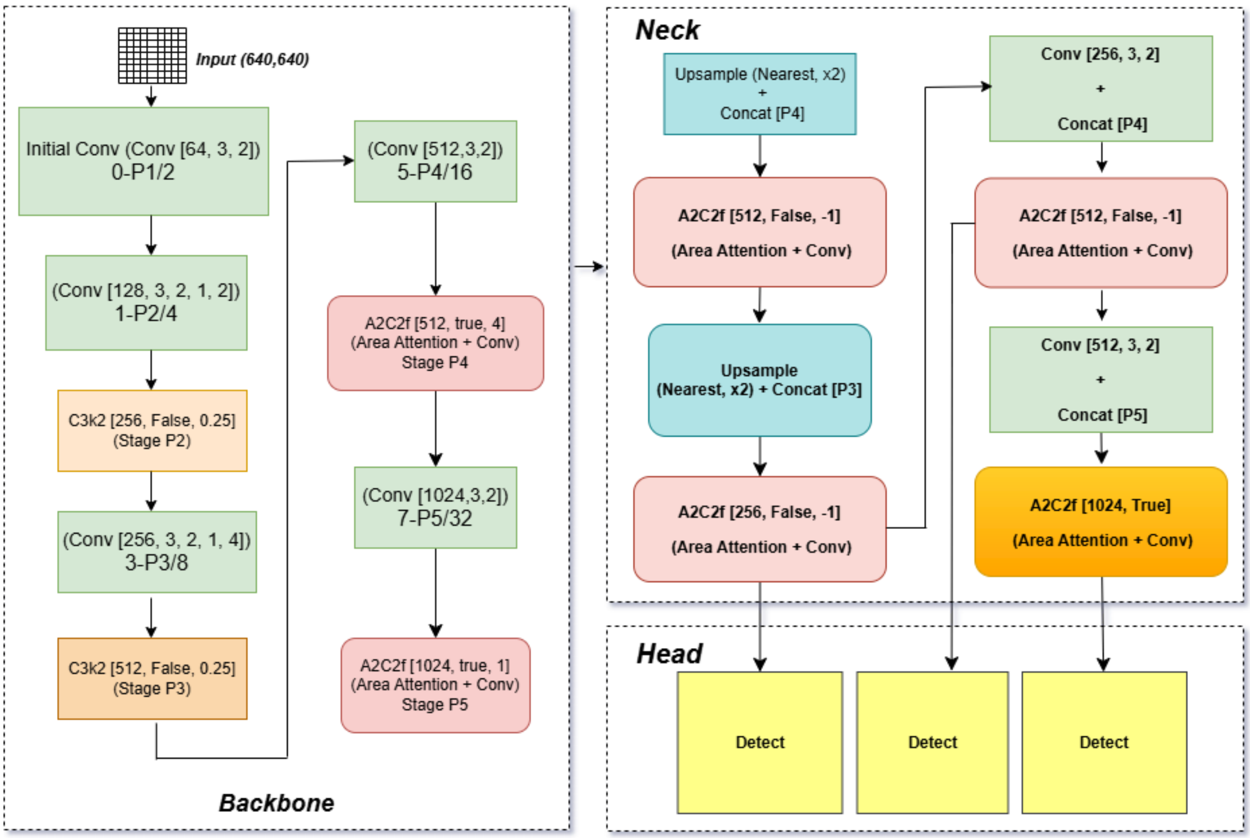

Figure V.3 The structural architecture of the proposed $A2C2f$ module, showcasing the parallel processing branches: the Area Attention (A2) block for spatial masking, the localized bottleneck pathways, and the identity residual shortcut mapping [15].

As tracked in Figure V.3, the $A2C2f$ engine executes parallel operations to balance representation accuracy and extraction efficiency:

1. **Area attention (A2) branches:** This stream isolates localized areas instead of computing a global attention map across the entire image, which suppresses uniform background cell grids. It creates projections for Queries (Q), Keys (K), and Values (V), following the structural matrix transformation:

$$Attention(Q,K,V) = softmax\left(\frac{QK^T}{\sqrt{d_k}}\right)V \quad (V\text{-}2)$$

Where d_k is the dimensionality scaling factor of the Key components, which regulates dot-product magnitudes to prevent gradient vanishing during softmax normalization.

2. **Residual ELAN (R-ELAN) pathways:** This path introduces an identity connection that directly bypasses the main attention blocks. This routing optimizes backpropagation gradient vectors near the network head, stabilizing deep learning paths and preventing vanishing gradients:

$$F_{output} = Conv(Concat(A2(F_{in}), Bottleneck(F_{in}))) + F_{in} \quad (V\text{-}3)$$

V.3.3 Multi-Scale neck segmented attention (Flash Attention)

To efficiently aggregate and propagate multi-scale feature representations to the detection head, the proposed network incorporates an Area Attention mechanism accelerated by a segmented Flash Attention formulation. Instead of processing the entire feature map simultaneously, the attention module partitions feature maps into localized spatial regions, thereby reducing memory bandwidth requirements and computational complexity while preserving long-range contextual information. This design enables efficient feature interaction and improves the representation of defect characteristics at different spatial scales.

Furthermore, the multi-scale feature maps generated throughout the backbone and neck are fused through complementary top-down and bottom-up feature propagation pathways interconnected by skip connections. This bidirectional feature aggregation preserves fine-grained spatial information required for the accurate localization of small defects while simultaneously enriching the semantic representation necessary for recognizing larger and more complex anomalies. As a result, the network achieves robust detection performance across photovoltaic defects exhibiting significant variations in size, shape, and appearance.

V.3.4 PV-YOLOv12n network layout and parameters

The global layer-by-layer parameter configuration, input routing paths (From), parameter volumes, and localized argument fields of the proposed PV-YOLOv12n model are comprehensively detailed in Table V-4.

Table V-4 Detailed parameter configuration and layer routing setup of the PV-YOLOv12n architecture [15].

Index	From	N	Params	Module	Arguments
0	-1	1	464	Conv	[3, 16, 3, 2]
1	-1	1	4672	Conv	[16, 32, 3, 2]
2	-1	1	6640	C3k2	[32, 64, 1, False, 0.25]
3	-1	1	36992	Conv	[64, 64, 3, 2]
4	-1	1	26080	C3k2	[64, 128, 1, False, 0.25]
5	-1	1	147712	Conv	[128, 128, 3, 2]
6	-1	2	180864	A2C2f	[128, 128, 2, True, 4]
7	-1	1	295424	Conv	[128, 256, 3, 2]
8	-1	2	689408	A2C2f	[256, 256, 2, True, 1]
9	-1	1	0	Upsample	[None, 2, 'nearest']
10	[-1, 6]	1	0	Concat	[1]
11	-1	1	86912	A2C2f	[384, 128, 1, False, -1]
12	-1	1	0	Upsample	[None, 2, 'nearest']
13	[-1, 4]	1	0	Concat	[1]
14	-1	1	24000	A2C2f	[256, 64, 1, False, -1]
15	-1	1	36992	Conv	[64, 64, 3, 2]
16	[-1, 11]	1	0	Concat	[1]
17	-1	1	74624	A2C2f	[192, 128, 1, False, -1]
18	-1	1	147712	Conv	[128, 128, 3, 2]
19	[-1, 8]	1	0	Concat	[1]
20	-1	1	394240	**A2C2f**	[384, 256, 1, True]
21	[14, 17, 20]	1	464912	Detect	[80, [64, 128, 256]]

V.3.5 Implementation workflow of the proposed PV-YOLOv12n framework

This section describes the programmatic implementation workflow adopted for the proposed photovoltaic defect detection framework. The objective is to provide a structured representation of the computational pipeline, beginning with dataset preparation and concluding with defect localization and classification. To clearly distinguish the reference architecture from the proposed contribution, two algorithms are presented. Algorithm 1 describes the implementation workflow of the baseline YOLOv12 detector, whereas Algorithm 2 details the proposed PV-YOLOv12n framework developed in this research.

The baseline YOLOv12 architecture follows the conventional Backbone–Neck–Head paradigm adopted by modern single-stage object detectors. The backbone is responsible for hierarchical feature extraction using convolutional layers, C3k2 blocks, and Area Attention-based A2C2f modules. The extracted features are subsequently aggregated by the neck through multi-scale feature fusion before being processed by the detection head to estimate bounding-box coordinates, object confidence, and class probabilities. During training, the network parameters are optimized by minimizing the composite detection loss through backpropagation and iterative parameter updates.

Building upon the baseline YOLOv12n architecture, the proposed PV-YOLOv12n introduces an enhanced feature extraction strategy specifically tailored for the detection of defects in photovoltaic EL images. The proposed modification replaces the original deep feature extraction block with the A2C2f module, which strengthens feature representation by incorporating an efficient area-attention mechanism while maintaining the lightweight nature and computational efficiency of the baseline network. This architectural enhancement enables the model to capture richer contextual information and more discriminative features, thereby improving its ability to identify subtle, low-contrast, and small-scale defects commonly encountered in EL imagery.

The extracted feature maps are subsequently propagated through the neck, where multi-scale feature fusion integrates low-level spatial details with high-level semantic information to enhance defect representation across different scales. These fused features are then forwarded to the detection head, which simultaneously performs bounding-box regression, objectness estimation, and defect classification. During inference, NMS is applied to remove redundant overlapping detections and retain only the most confident predictions, resulting in accurate and reliable localization of photovoltaic defects. The complete implementation workflow of both the baseline YOLOv12n and the proposed PV-YOLOv12n models is summarized in Algorithms 1 and 2, respectively.

Algorithm 1 Baseline YOLOv12 Implementation

```
Input:
      Training dataset Dtrain
      Validation dataset Dval
      Number of epochs E
      Learning rate α
      Batch size B

Output:
      Trained YOLOv12 detector

1: Initialize the YOLOv12 network parameters.

2: for epoch = 1 to E do

3:      for each mini-batch Bi ∈ Dtrain do

4:          Load EL images and annotations.

5:          Resize and normalize the input images.

6:          Apply data augmentation.

7:          Perform forward propagation through

                Backbone
                    ├── Convolution Layers
                    ├── C3k2 Modules
                    └── A2C2f Modules with Area Attention

8:          Aggregate multi-scale features
            using the Neck.

9:          Generate object predictions
            using the Detection Head.

10:         Compute the overall detection loss.

11:         Perform backpropagation.

12:         Update network parameters.

13:     end for

14:     Evaluate the model on Dval.

15:     Save the best-performing model.

16: end for

17: Return the trained YOLOv12 detector.
```

Algorithm 2 Proposed PV-YOLOv12n Implementation

```
Input:
      Training dataset Dtrain
      Validation dataset Dval
      Number of epochs E
      Learning rate α
      Batch size B

Output:
      Trained PV-YOLOv12n detector

1: Initialize the baseline YOLOv12 network.

2: Replace the original deep C3k2 feature extraction
   block with the proposed A2C2f module.

3: for epoch = 1 to E do

4:      for each mini-batch Bi ∈ Dtrain do

5:          Load EL images and annotations.

6:          Resize and normalize the input images.

7:          Apply data augmentation.

8:          Perform forward propagation through
            the modified backbone.

9:          Extract hierarchical features using
            the proposed A2C2f module.

10:         Enhance defect-sensitive feature
            representations via Area Attention.

11:         Fuse multi-scale feature maps
            using the Neck.

12:         Predict bounding boxes,
            confidence scores,
            and defect categories
            using the Detection Head.

13:         Compute the total detection loss.

14:         Perform backpropagation.

15:         Update network parameters.

16:     end for

17:     Evaluate the model on Dval.

18:     Save the best-performing model.

19: end for

20: During inference,
      apply confidence thresholding
      followed by Non-Maximum Suppression.

21: Return the final PV-YOLOv12n detector.
```

V.4 Performance evaluation and results

This section presents the comprehensive results of the experiments. The proposed PV-YOLOv12n model is quantitatively and qualitatively benchmarked against the baseline YOLOv12n. The analysis covers overall performance, training dynamics, per-class accuracy, qualitative visual output, and a comparison against state-of-the-art (SOTA) models.

V.4.1 Quantitative performance comparison

The primary evaluation was a direct comparison between the proposed PV-YOLOv12n and the baseline YOLOv12n, trained and tested on both the PVEL-AD and Roboflow datasets.

Table V-5 *Overall performance and efficiency comparison [15].*

Dataset	Model	mAP@50	mAP@50-95	Precision	Recall	Inference Speed (ms)	Parameters	GFLOPs
PVEL-AD	**YOLOv12n**	**0.90**	**0.57**	**0.83**	**0.86**	**4.26**	**2,602,288**	**6.65**
PVEL-AD	**PV-YOLOv12n**	**0.91**	**0.58**	**0.84**	**0.87**	**4.24**	**2,617,648**	**6.66**
Roboflow	**YOLOv12n**	**0.88**	**0.73**	**0.89**	**0.87**	**4.45**	**2,602,288**	**6.65**
Roboflow	**PV-YOLOv12n**	**0.91**	**0.75**	**0.92**	**0.88**	**4.43**	**2,617,648**	**6.66**

The results, summarized in

Table V-5, clearly demonstrate the efficacy of the proposed architectural modification.

A. **Accuracy on PVEL-AD:** On the PVEL-AD dataset, the proposed PV-YOLOv12n outperformed the baseline YOLOv12n, achieving an mAP@50 of 0.91 compared with 0.90. The improvement was more pronounced under the stricter mAP@50–95 metric, where PV-YOLOv12n reached 0.58, demonstrating superior localization accuracy across multiple IoU thresholds.

B. **Generalization on Roboflow:** This performance improvement extended to the Roboflow dataset, which validates the model's generalization. The PV-YOLOv12n achieved a mAP@50 of 0.91 and a mAP@50-95 of 0.75, outperforming the baseline in both metrics.

C. **Computational efficiency:** Crucially, these accuracy gains were achieved with negligible computational overhead. As shown in

D. Table **V-5**, the PV-YOLOv12n model maintains a highly efficient profile (2.6M parameters, 6.6 GFLOPs), confirming its suitability for real-time deployment.

V.4.2 Ablation study: impact of the A2C2f module

An ablation study was conducted to assess the effectiveness of the proposed architectural enhancement by comparing the baseline YOLOv12n with the optimized PV-YOLOv12n model under identical training conditions. By keeping the hyperparameters, learning schedule, and data partitioning unchanged, the contribution of the A2C2f module was evaluated independently in terms of detection accuracy and computational efficiency. The results on the PVEL-AD and Roboflow datasets are presented in Table V-6.

Table V-6 *Ablation study results comparing the Baseline YOLOv12n and the optimized PV-YOLOv12n across both datasets [15].*

Dataset	**Model**	**Precision**	**Recall**	**mAP@50**	**mAP@50-95**	**Speed (ms)**	**Params**	**GFLOPs**
PVEL-AD	YOLOv12n (Base)	0.83	0.86	0.90	0.57	4.26	2,602,288	6.65
	PV-YOLOv12n (Ours)	**0.84**	**0.87**	**0.91**	**0.58**	**4.24**	2,617,648	6.66
Roboflow	YOLOv12n (Base)	0.89	0.87	0.88	0.73	4.45	2,602,288	6.65
	PV-YOLOv12n (Ours)	**0.92**	**0.88**	**0.91**	**0.75**	**4.43**	2,617,648	6.66

V.4.3 PVEL-AD dataset

The introduction of the A2C2f module led to measurable improvements in the balance between detection accuracy and sensitivity when evaluated on the cell-level PVEL-AD dataset. The optimized architecture exhibited consistent gains across localization, classification, and efficiency-related metrics.

With respect to localization performance, the enhanced model achieved a modest yet consistent improvement of 1% in both mAP@50 (increasing from 0.90 to 0.91) and mAP@50–95 (rising from 0.57 to 0.58). These results indicate improved bounding-box alignment over a broad range of Intersection over Union thresholds, reflecting more precise spatial predictions.

Improvements were also observed in error suppression behavior. Precision increased from 0.83 to 0.84, while recall reached 0.87, suggesting that the modified network more effectively discriminates defect regions from background patterns. This indicates a reduction in false detections without sacrificing the ability to identify true defect instances.

From a computational standpoint, the integration of the A2C2f module resulted in only a minor increase in model size, corresponding to an additional 15,360 parameters (approximately 0.58%). Notably, this increase did not introduce inference overhead; instead, a slight improvement in runtime was observed, with an average inference time of 4.24 ms. This confirms that the proposed enhancement improves feature representation efficiency without compromising real-time performance.

V.4.4 Roboflow dataset

The benefits of the proposed architectural enhancement become even more evident when evaluated on the Roboflow dataset, which presents greater visual complexity and more realistic operating conditions due to environmental disturbances, varying illumination, and diverse defect appearances. These challenging characteristics provide a more rigorous assessment of the model's robustness and generalization capability.

Quantitative results demonstrate that PV-YOLOv12n consistently outperforms the baseline YOLOv12n across all major detection metrics. In particular, the proposed model achieves an improvement of 3.3% in mAP@50, increasing from 0.88 to 0.91, together with a 2.6% gain in mAP@50–95, improving from 0.73 to 0.75. These results confirm that the proposed feature extraction strategy enhances the model's ability to generalize to complex real-world scenarios while maintaining reliable detection performance under challenging imaging conditions.

A notable improvement is also observed in precision, which increases from 0.89 to 0.92. This enhancement indicates that the A2C2f module effectively strengthens feature discrimination by emphasizing informative defect characteristics while suppressing background noise and irrelevant features. Consequently, the model produces fewer false-positive detections arising from environmental artifacts, such as dust accumulation, bird droppings, shadows, and surface contamination, which frequently interfere with outdoor photovoltaic inspections.

Furthermore, the improvement in mAP@50–95 demonstrates the proposed model's enhanced localization accuracy across a broad range of Intersection over Union (IoU) thresholds. Since this metric imposes progressively stricter localization requirements, the observed gain indicates that PV-YOLOv12n is more capable of accurately identifying defects exhibiting significant variations in size, shape, and appearance, particularly small-scale and low-contrast anomalies that are difficult to detect using conventional feature extraction mechanisms. These findings demonstrate that the proposed architectural modification not only improves overall detection accuracy but also enhances localization precision and robustness, making the model more suitable for practical photovoltaic fault diagnosis in real-world operating environments.

V.4.5 Training dynamics and convergence analysis

To assess the convergence behavior of the PV-YOLOv12n architecture, a detailed analysis was conducted by monitoring the evolution of both mAP@50 and the more stringent mAP@50–95 metrics throughout the complete training process, comparing the results between the baseline YOLOv12n and the modified model. The mAP@50 results are displayed in figure V.4, while the mAP@50-95 results are shown in figure V.5.

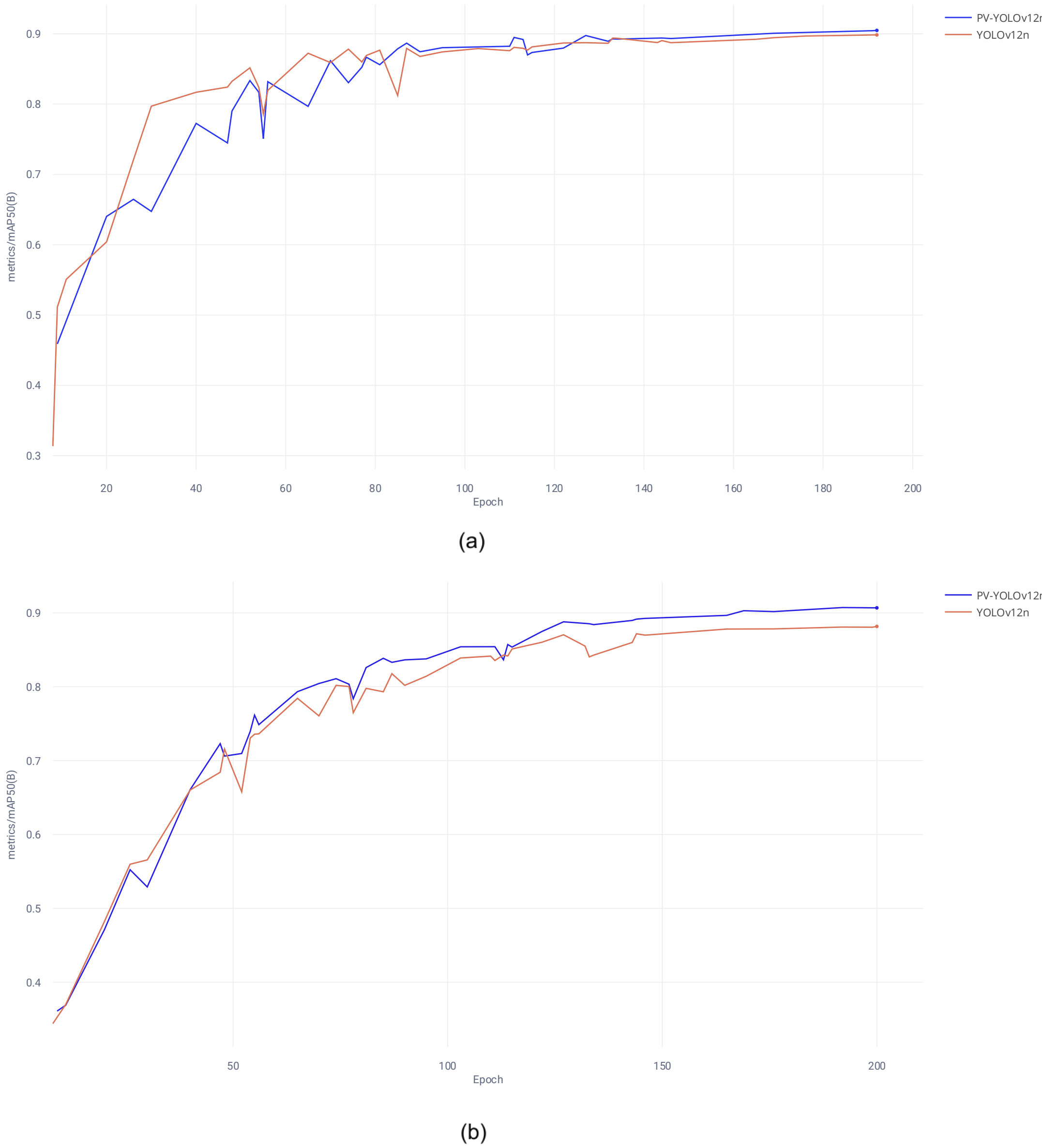

Figure V.4 mAP@50 convergence analysis of PV-YOLOv12n versus baseline YOLOv12n on (a) PVEL-AD dataset and (b) Roboflow dataset [15].

On the primary PVEL-AD dataset, the PV-YOLOv12n model exhibited faster and more stable convergence relative to the baseline YOLOv12n. The modified architecture reached its final mAP@50 of 0.91 by approximately epoch 160, whereas the baseline model only plateaued at 0.90 around epoch 180. This accelerated improvement can be attributed to the A2C2f module, which enhances feature extraction from the earliest stages of training. Evidence of this effect is seen in the substantially steeper slope of the PV-YOLOv12n learning curve during the initial epochs (0–

50), indicating rapid acquisition of defect-relevant representations. This trend was also consistent for the stricter mAP@50-95 metric, where the PV-YOLOv12n maintained a consistent advantage, suggesting the module yields more precise bounding box predictions under tighter localization constraints.

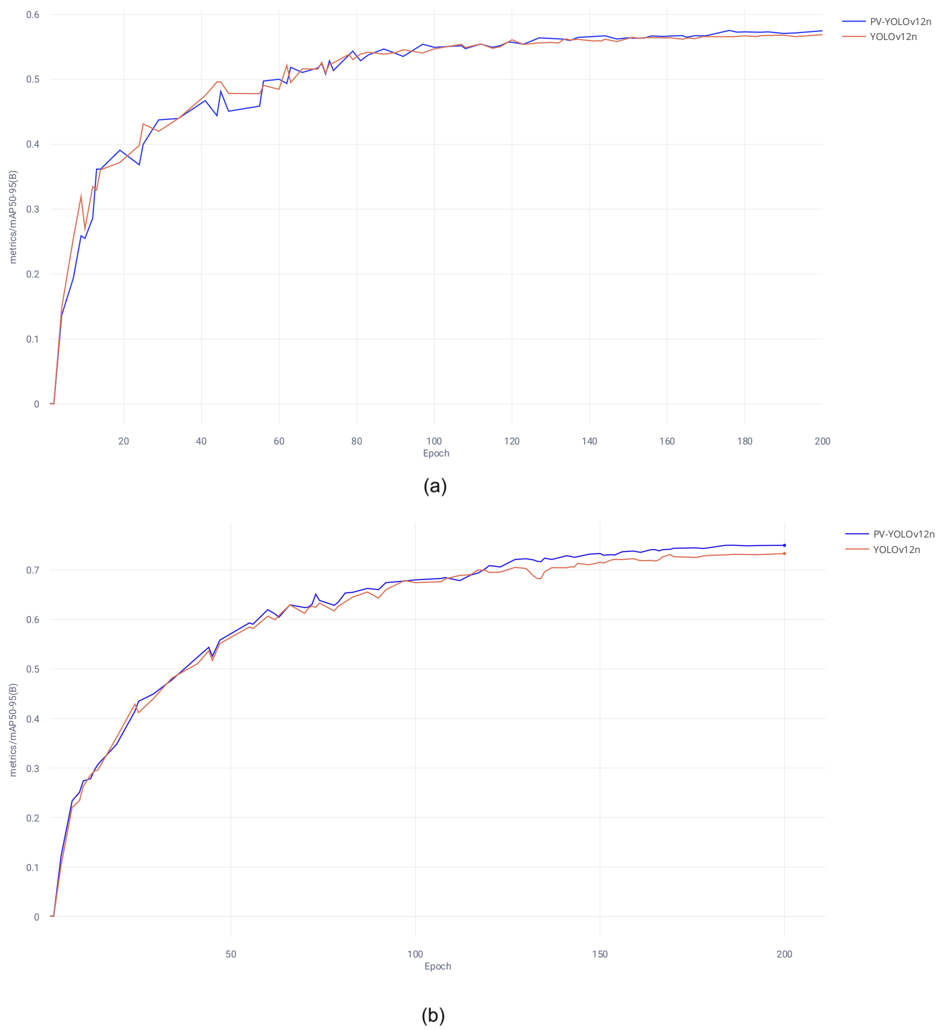

Figure V.5 mAP@50-95 convergence analysis of PV-YOLOv12n versus baseline YOLOv12n on (a) PVEL-AD dataset and (b) Roboflow dataset [15].

Evaluating the model using the stricter mAP@50–95 metric, which calculates average precision across a narrower range of Intersection over Union thresholds, provides clear insight into its fine-grained localization capabilities. On the PVEL-AD dataset, PV-YOLOv12n consistently outperformed the baseline throughout training, ultimately reaching 0.58 compared to 0.57 for YOLOv12n, as depicted in Figure V.5. This performance advantage was more pronounced on the

Roboflow dataset, where the enhanced model achieved 0.75 mAP@50–95, exceeding the baseline's 0.73. The sustained improvement under these tighter evaluation criteria demonstrates that the A2C2f module strengthens feature representation, resulting in more precise bounding-box predictions across varying IoU thresholds a critical benefit when detecting the diverse, real-world defects present in the Roboflow images.

In addition to the quantitative mAP analysis, the classification performance of both models was assessed visually through confusion matrices generated from the test sets of the PVEL-AD and Roboflow datasets (Figures IV.6 and IV.7). This comparison illustrates each model's ability to correctly discriminate between visually similar photovoltaic defect classes, providing complementary evidence of PV-YOLOv12n's improved detection reliability.

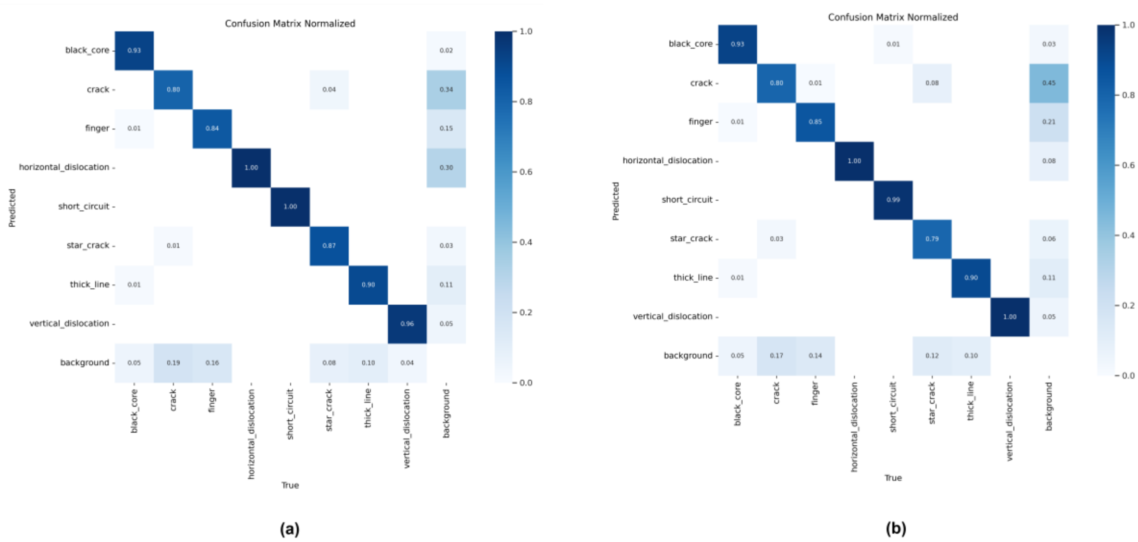

Figure V.6 Comparison of classification performance on the PVEL-AD Dataset. confusion matrix for (a) PV-YOLOv12n and (b) baseline YOLOv12n [15]

Figure V.6 illustrates that both models achieve generally strong classification performance, as evidenced by the concentration of high true positive values along the main diagonal of the confusion matrices. Nevertheless, the PV-YOLOv12n model (Figure V.6 (a)) demonstrates a noticeable decrease in misclassification rates relative to the baseline (Figure V.6 (b)). This improvement is especially apparent when differentiating visually similar defect types, such as subtle variations between standard cracks and star cracks. The enhanced feature representation and attention mechanism introduced by the A2C2f module enable PV-YOLOv12n to achieve more precise localization and a better balance between precision and recall, thereby reducing false positives in these challenging categories.

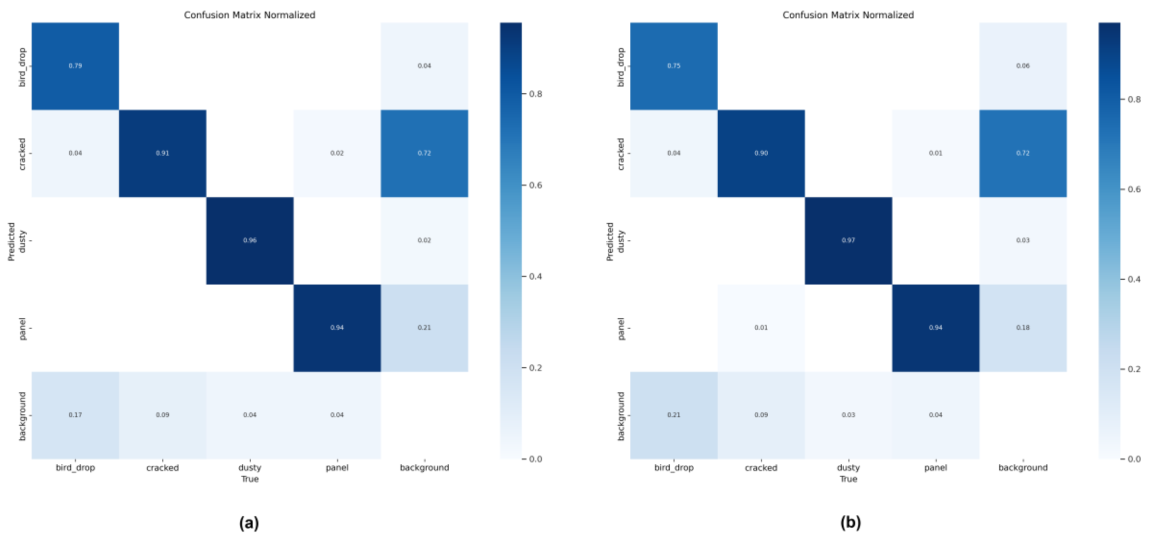

Figure V.7 Comparison of classification performance on the Roboflow dataset. confusion matrix for (a) PV-YOLOv12n and (b) baseline YOLOv12n [15]

Analysis of the confusion matrices for the Roboflow dataset indicates that PV-YOLOv12n (Figure V.7 (a)) outperforms the baseline in defect classification, as shown by the increased concentration of true positives along the main diagonal. The enhanced architecture demonstrates particular strength in identifying small or environmentally complex anomalies, such as bird droppings and dust deposits, which often confuse standard detection models. By refining the feature representation through the A2C2f module, the network achieves more accurate localization and substantially reduces false positives, thereby improving the reliability and robustness of defect detection under the diverse and challenging conditions present in real-world photovoltaic imagery.

To evaluate how effectively the models maintain a balance between precision and recall during training, the F1-score was monitored across all epochs for both architectures. This metric serves as an important indicator of the models' stability and reliability in detecting defects throughout the learning process.

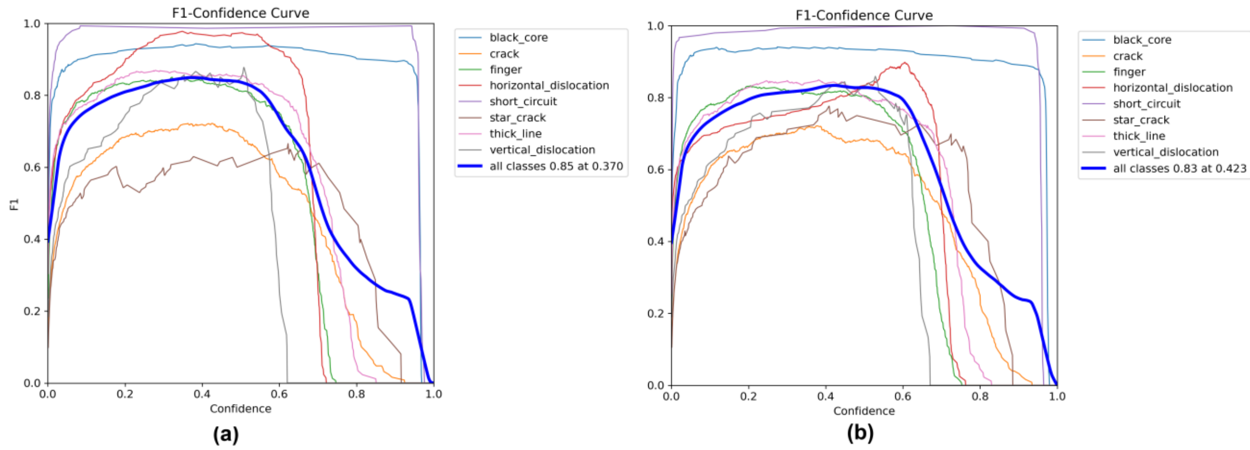

Figure V.8 F1-score convergence analysis of (a) PV-YOLOv12n versus (b) baseline YOLOv12n on the PVEL-AD dataset [15].

As shown in Figure V.8 for the PVEL-AD dataset, PV-YOLOv12n consistently outperformed the baseline across the entire training period. The F1-score of the proposed model started at 0.52 during the initial epochs and gradually increased to a maximum of 0.87, compared with YOLOv12n, which began at 0.49 and plateaued at 0.85. The accelerated convergence and higher sustained F1-scores highlight the enhanced stability and robustness of defect detection achieved by the modified architecture. Notably, PV-YOLOv12n reached its peak performance roughly 20 epochs earlier than the baseline, reflecting the improved learning efficiency afforded by the A2C2f module, which facilitates more effective feature extraction and selective attention.

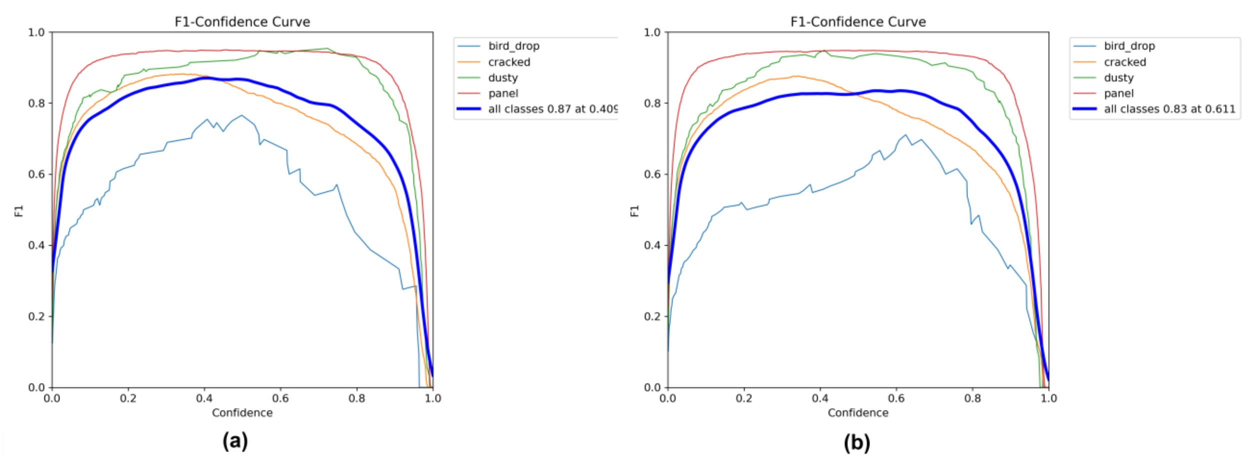

Figure V.9 F1-score convergence analysis of (a) PV-YOLOv12n versus (b) baseline YOLOv12n on the Roboflow dataset [15].

A similar performance trend was observed on the Roboflow dataset (Figure V.9), further demonstrating that the proposed PV-YOLOv12n maintains a more favorable balance between precision and recall under realistic and challenging operating conditions. Unlike electroluminescence images acquired in controlled environments, the Roboflow dataset comprises RGB images affected by varying illumination, complex backgrounds, shadows, perspective changes, and environmental contaminants, making the defect detection task considerably more demanding. Despite these challenges, the proposed model consistently exhibits superior learning behavior throughout the training process.

As illustrated in Figure V.9, the F1-score of PV-YOLOv12n increases steadily from approximately 0.55 during the initial training epochs to a final value of 0.91, whereas the baseline YOLOv12n starts at 0.51 and gradually converges to 0.88. This consistent improvement indicates that the proposed architecture achieves a more effective compromise between minimizing false positives and reducing false negatives, thereby producing a more reliable detector across diverse defect categories. The higher final F1-score confirms that the integration of the A2C2f module enables the network to learn more discriminative and robust feature representations, particularly for subtle and difficult-to-detect photovoltaic defects.

The improvement is especially significant for small-scale, low-contrast, and environmentally induced defects, including dust accumulation, bird droppings, localized contamination, and other surface anomalies whose visual appearance often resembles the surrounding background. By enhancing feature representation through attention-guided information aggregation, the proposed module enables the detector to preserve fine structural details while simultaneously exploiting broader contextual information, thereby reducing both missed detections and false alarms.

V.4.6 Per-class performance and modality analysis

To understand the nuanced impact of the A2C2f module, a comprehensive per-class performance comparison was conducted across all defect categories in both the PVEL-AD (cell-level) and Roboflow (module-level) datasets. The results, summarized in Table V-7, confirm that the model's overall accuracy gains are driven by substantial improvements in the detection of challenging, small-sized defects.

Table V-7 *Comprehensive defect detection performance comparison using mAP@0.5 across individual classes and datasets [15].*

Dataset	Defect Class	PV-YOLOv12n (mAP@0.5)	YOLOv12n (mAP@0.5)	Improvement (Δ%)	Size Category
PVEL-AD	Black_core	97.6	96.7	+0.9	Large
	crack	83.5	76.7	+6.8	Small-medium
	finger	89.6	90.1	-0.5	Medium
	horizontal_dislocation	94.0	99.3	-5.3	Large
	short_circuit	99.5	99.5	0.0	Large
	star_crack	77.9	72.8	+5.1	Small
	thick_line	93.0	90.9	+2.1	Medium
	vertical_dislocation	95.3	95.5	-0.2	Large
	mAP@0.5 (Overall)	**91.3**	**90.2**	**+1.1**	All sizes
Roboflow	bird_drop	73.9	65.5	+8.4	Small
	cracked	93.6	92.2	+1.4	Medium-large
	dusty	98.8	97.5	+1.3	Large
	panel	97.5	97.4	+0.1	Large
	mAP@0.5 (Overall)	**90.9**	**88.2**	**+2.7**	All sizes

V.4.7 Comparison with state-of-the-Art YOLO architectures

To position the proposed work within the current landscape of real-time object detection, a final benchmarking comparison was performed against various contemporary and predecessor YOLO architectures (YOLOv8n through YOLOv12n). This evaluation assessed both detection accuracy and computational overhead, using the PVEL-AD and Roboflow datasets. The results are summarized in Table V-8.

Table V-8 *Performance comparison of YOLO-based models across the PVEL-AD and Roboflow datasets, using both accuracy and efficiency metrics.*

Model	PVEL-AD				Roboflow Dataset				Parameters (M)	GFLOPs
	mAP@0.5	Precision	Recall	mAP@0.5:0.95	mAP@0.5	Precision	Recall	mAP@0.5:0.95		
PV-YOLOv12n	**91.3**	**88.7**	**86.1**	**57.8**	**90.9**	**87.0**	**86.8**	**76.8**	**2.6**	**6.6**
YOLOv12n	90.2	84.4	86.3	57.1	88.2	85.1	85.6	75.5	2.6	6.5
YOLOv11n	89.5	86.1	85.8	52.3	89.2	84.5	85.8	73.3	2.6	6.5
YOLOv10n	86.8	86.6	85.9	49.4	87.4	80.8	79.5	64.6	2.3	6.7
YOLOv9t	85.3	81.5	90.4	45.5	86.9	86.8	75.5	59.6	2.0	7.7
YOLOv8n	91.3	89.3	87.3	58.3	87.3	78.9	86.9	67.4	3.2	8.7

The PV-YOLOv12n model consistently achieved the highest, or at least equal highest, detection accuracy (mAP@0.5) across both evaluated datasets, confirming its effectiveness for photovoltaic defect detection. On the PVEL-AD dataset, the model reached 91.3% mAP@0.5, while on the Roboflow dataset it attained 90.9%. These modest yet consistent improvements over the baseline YOLOv12n illustrate the beneficial impact of the A2C2f architectural enhancement on overall detection performance. Earlier YOLO versions, including v9t, v10n, and v11n, generally demonstrated lower accuracy and, in certain cases, higher computational overhead, highlighting the progressive efficiency gains in the more recent YOLO series.

A notable distinction emerges in comparison with YOLOv8n. Although YOLOv8n matches PV-YOLOv12n with a 91.3% mAP@0.5 on PVEL-AD, the latter exhibits a clear advantage in computational efficiency. PV-YOLOv12n requires only 6.6 GFLOPs and contains 2.6 million parameters, whereas YOLOv8n demands 8.7 GFLOPs and 3.2 million parameters. This reduction in model complexity directly translates to lower inference latency, making PV-YOLOv12n not only highly accurate but also more practical for deployment in real-time, resource-constrained photovoltaic inspection systems.

V.4.8 Visual presentation and discussion

The quantitative findings are further substantiated through a qualitative visual analysis of the model's defect localization performance and activation patterns.

V.4.8.1 Bounding box comparison of defect detection

Figure V.10 presents a comparative visualization of the defect detection results produced by the proposed PV-YOLOv12n and the baseline YOLOv12n across both the PVEL-AD and Roboflow datasets. The qualitative comparison complements the quantitative evaluation presented in the previous sections by providing visual evidence of the improvements achieved through the proposed architectural modification. The results clearly demonstrate that PV-YOLOv12n delivers more accurate, robust, and consistent defect localization across a wide range of defect types and imaging conditions. The bounding boxes generated by the proposed model are generally tighter, more precisely aligned with the actual defect boundaries, and exhibit fewer localization errors, reflecting its superior ability to accurately identify and delineate photovoltaic defects. Such precise localization is essential for reliable fault diagnosis and subsequent maintenance planning in photovoltaic systems.

In contrast, the baseline YOLOv12n displays greater variability in its predictions, with bounding boxes that are frequently less well-fitted to the defect regions and occasionally include unnecessary background or fail to fully encompass the defective areas. These localization inaccuracies become more apparent when defects are small, exhibit irregular shapes, or possess low visual contrast relative to the surrounding cell or module surface. Moreover, PV-YOLOv12n demonstrates improved detection of subtle and fine-grained anomalies in both the controlled PVEL-AD electroluminescence images and the more challenging Roboflow RGB images, particularly when defects are embedded within complex textures or affected by environmental disturbances. This enhanced localization capability indicates that the proposed A2C2f module enables the network to preserve fine spatial details while simultaneously exploiting richer contextual information, leading to more reliable discrimination between defective and non-defective regions. Overall, the superior qualitative results observed in Figure V.10 further validate the effectiveness of the proposed architecture and demonstrate its practical advantages for accurate, reliable, and real-world photovoltaic defect detection.

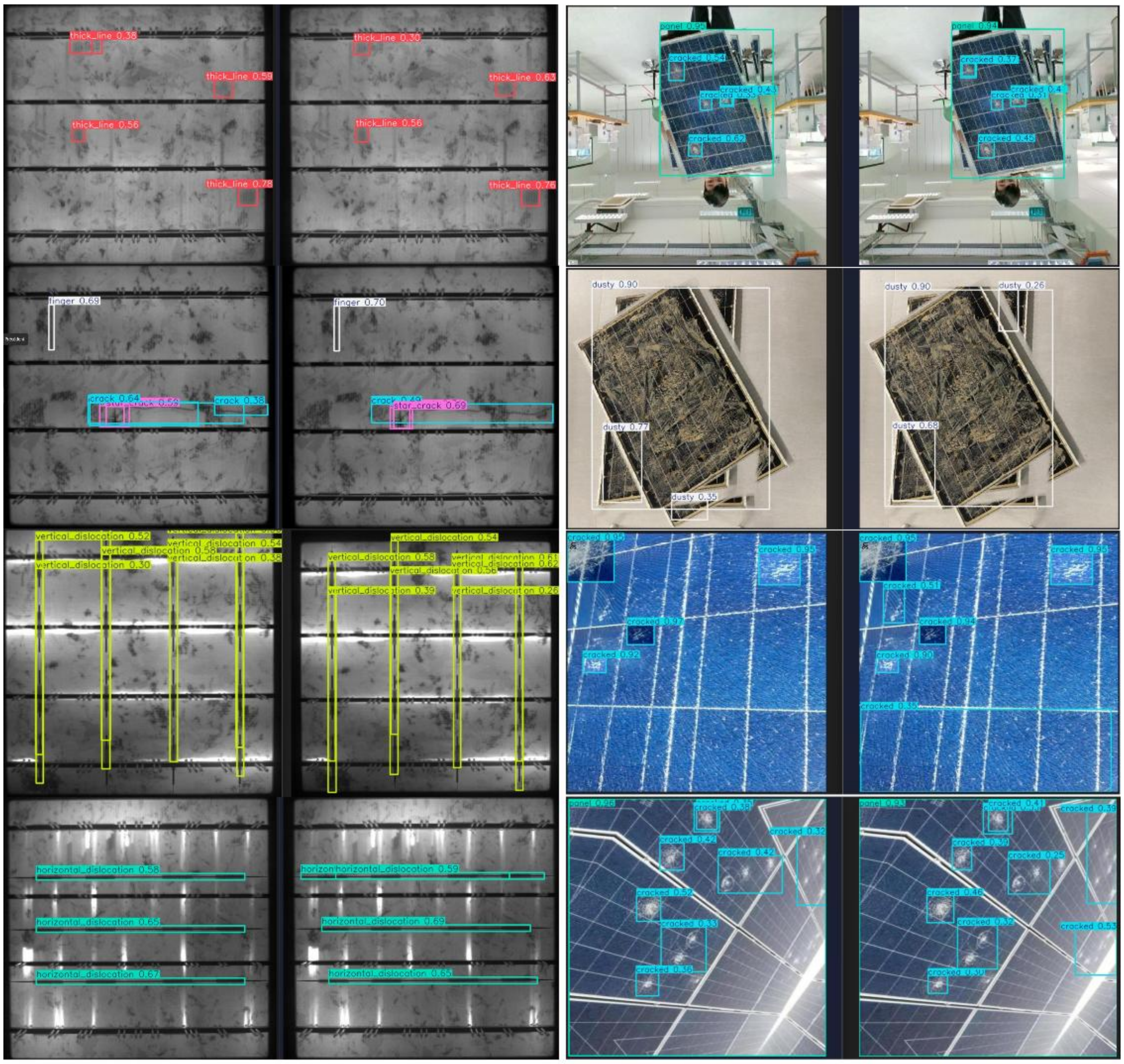

(PV-YOLOv12n) (YOLOv12n) (PV-YOLOv12n) (YOLOv12n)

(a) (b)

Figure V.10 Comparative visualization of bounding box predictions for (a) PVEL-AD and (b) Roboflow datasets, comparing PV-YOLOv12n and baseline YOLOv12n [15].

V.4.8.2 Heatmap analysis of defect detection

To further demonstrate the enhancements in defect localization, Figure V.11 provides heatmap visualizations that indicate the intensity of model activations and identify regions most influential in their predictions. Across both the PVEL-AD (Figure V.11 (a)) and Roboflow (Figure V.11 (b)) datasets, PV-YOLOv12n shows stronger and more concentrated activations around defect-prone areas, including structural cracks and horizontal dislocations. The regions highlighted in red correspond to areas where the model exhibits higher confidence in defect boundaries. In contrast, the baseline YOLOv12n produces more diffuse activations, reflecting less precise localization. The focused and compact activation patterns of PV-YOLOv12n confirm its superior ability to detect subtle and complex defects with greater accuracy.

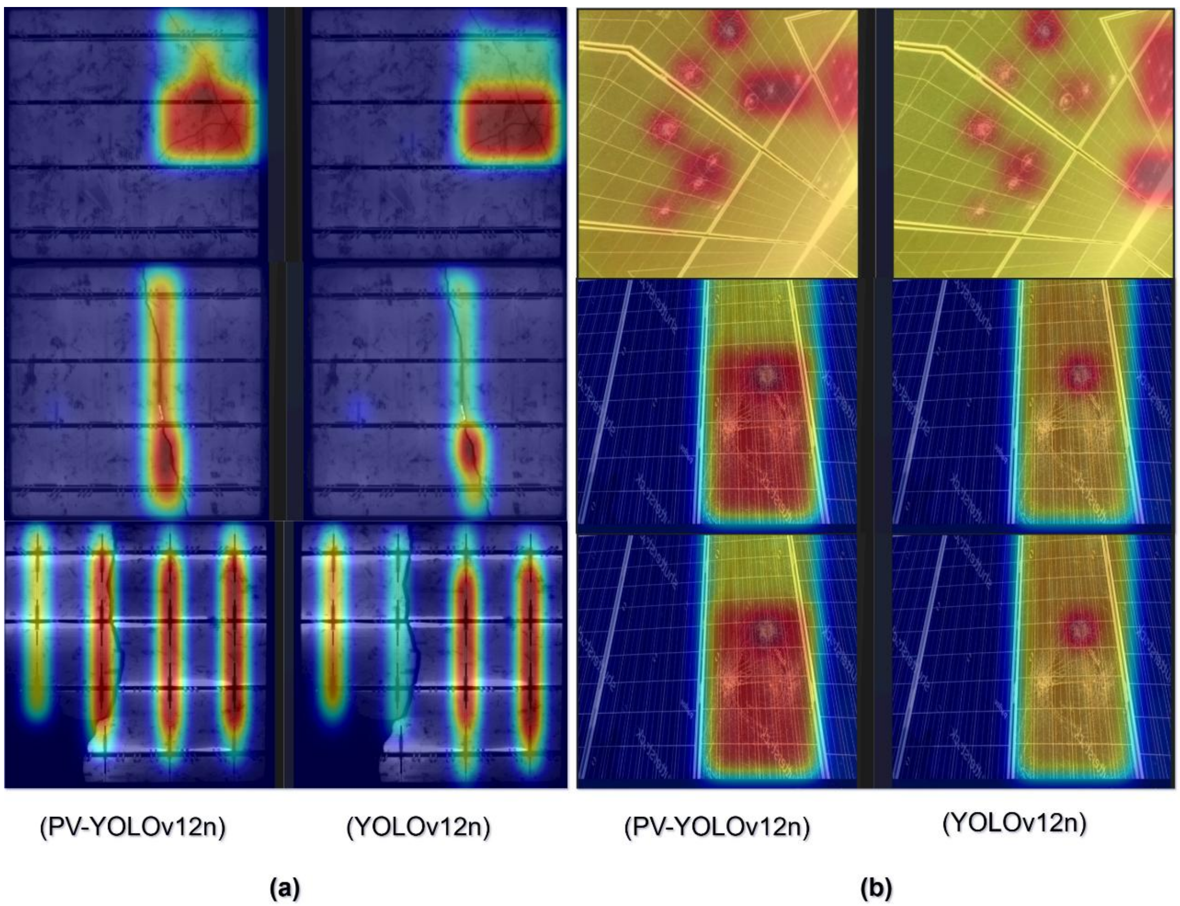

Figure V.11 Heatmap visualizations comparing the activation intensity of PV-YOLOv12n and YOLOv12n on (a) PVEL-AD and (b) Roboflow datasets [15].

V.4.9 Discussion

The comprehensive evaluation demonstrates that incorporating the A2C2f module into the YOLOv12 architecture significantly improves PV defect detection accuracy while maintaining high computational efficiency. PV-YOLOv12n achieved 91.3% mAP@50 on the PVEL-AD dataset and 90.9% mAP@50 on the Roboflow dataset, consistently surpassing the baseline YOLOv12n. Furthermore, it provides a more computationally efficient alternative to other high-accuracy models such as YOLOv8n.

Key advantages of the architectural enhancements include:

- **Precision-recall stability:** The model exhibits higher F1-scores and faster convergence, reflecting robust sensitivity to defects and a lower false positive rate throughout training.
- **Enhanced small-scale defect localization:** Leveraging the Area Attention A2 mechanism within the A2C2f module, the network prioritizes critical regions, leading to significant improvements in detecting challenging, small defects such as star cracks (+5.1) and bird droppings (+8.4).
- **Lightweight computational efficiency:** With only 2.6 million parameters and 6.6 GFLOPs, PV-YOLOv12n is well-suited for deployment on resource-constrained edge devices, including drone-based inspection systems.

A particularly notable outcome is the consistent performance across two fundamentally different data modalities: the Electroluminescence (EL) PVEL-AD dataset and the RGB-based Roboflow dataset. This modality-independent success is largely attributed to the A2C2f module.

For EL imagery, PV defects manifest as subtle, low-contrast luminance variations. The Area Attention mechanism amplifies these faint structural signals associated with cracks and dislocations while suppressing uniform or noisy background regions. In contrast, the RGB Roboflow dataset presents defects with complex textures and irregular shapes, such as bird droppings or dust. The same attention mechanism effectively prioritizes these anomalous features regardless of background color or variability. Additionally, the R-ELAN component stabilizes gradient flow, ensuring robust convergence for datasets with distinct feature distributions. Consequently, the A2C2f module enhances performance across data types by improving figure-ground separation and feature refinement, rather than being tailored to a specific imaging modality.

Electroluminescence imaging provides a particularly strong foundation for PV defect detection due to the direct correspondence between visual patterns and underlying physical phenomena. The architecture of PV-YOLOv12n, combined with the PVEL-AD defect categorization, exploits this relationship to deliver high industrial interpretability and actionable quality control insights. Each detected anomaly corresponds to a distinct physical defect: for instance, cracks indicate wafer fractures leading to interrupted current flow, whereas a 'Black Core' points to localized poor silicon quality caused by non-radiative recombination.

V.4.10 Comparison with recent works

To thoroughly assess the effectiveness of the proposed PV-YOLOv12n model, a detailed benchmark was performed against both contemporary and earlier state-of-the-art YOLO-based defect detection methods. The results, summarized in Table V-9, highlight the comprehensive strengths of the proposed approach.

PV-YOLOv12n achieved strong performance, with a mAP@50 of 91.3% on the PVEL-AD dataset and 90.9% on the Roboflow dataset. One of the model's most notable advantages is its robust generalization capability, which is rarely observed in highly specialized competing architectures. PV-YOLOv12n consistently delivers high accuracy across two distinct and challenging public datasets: the Roboflow Universe dataset, containing 6,493 RGB images, and the PVEL-AD dataset, comprising 5,589 EL images. This consistent performance across different imaging modalities and large-scale datasets demonstrates the model's versatility and resilience.

When compared to models evaluated on the same Roboflow dataset, such as YOLOv11m, the slightly lower mAP of PV-YOLOv12n reflects an intentional design trade-off for markedly reduced computational requirements, enabling real-time deployment on edge devices, including drones. Achieving 91.3% mAP@50 on the complex PVEL-AD dataset with eight defect classes is comparable to larger models such as MRA-YOLOv8, which achieves 91.7% but incurs significantly higher computational costs.

In summary, the comparative analysis confirms that PV-YOLOv12n excels beyond isolated accuracy metrics by offering a well-balanced and application-oriented solution. Although certain specialized models achieve higher performance figures under tightly controlled experimental conditions, their applicability is often limited. In contrast, PV-YOLOv12n delivers a compelling combination of competitive detection accuracy, robust generalization across heterogeneous public datasets including both optical (RGB) and EL imagery and notably low computational complexity. This balanced performance profile positions PV-YOLOv12n as a scalable, reliable, and deployment-ready framework for real-world automated photovoltaic inspection and monitoring systems.

Table V-9 *Performance comparison of PV-YOLOv12n with recent methods for solar panel defect detection across multiple datasets (mAP@50) [15].*

Author	Year	Dataset	Image Type	Classes	Images	Method	Accuracy (%)
Zheng et al.	2022	Self-Constructed	Infrared	2	3360	S-YOLOv5	98.1
Zhang & Yin	2022	Self-Constructed	EL	3	2534	Improved YOLOv5	89.6
Chen et al.	2023	PVEL-AD (EL 2021)	EL	3	5246	SSD	78.0
						Faster R-CNN	72.27
						RCA-Faster R-CNN	83.29
						RetinaNet	84.53
						MCSAM	87.14
Li et al.	2023	PV-Multi-Defect	Grayscale	5	1108	GBH-YOLOv5	97.8
Pan et al.	2024	PVEL-AD	EL	10	4500	YOLO-ACF	92.6
Wang et al.	2025	PVEL-AD	EL	8	—	MRA-YOLOv8	91.7
		SPDI	EL/Optical	3	—	—	69.3
Khanam et al.	2025	Roboflow Universe	Optical/RGB	4	6493	YOLOv11m	93.4
						YOLOv8	92.3
Xu et al.	2025	Self-Constructed	PL	6	4500	YOLOv5	91.5
Ghahremani et al.	2025	Self-Constructed	Thermal	3	316	YOLOv11-X	92.7
Proposed	**2025**	**Roboflow Universe**	**Optical/RGB**	**4**	**6493**	**PV-YOLOv12n**	**91.0**
Proposed	**2025**	**PVEL-AD**	**EL**	**8**	**5589**	**PV-YOLOv12n**	**91.0**

V.4.11 Conclusion

The study successfully demonstrates that PV-YOLOv12 provides an efficient and highly accurate framework for the automated detection of defects in photovoltaic cells and panels. By integrating the specialized A2C2f module, the model enhances feature extraction to reliably capture fine microcracks, material anomalies, and surface defects across both the PVEL-AD and Roboflow datasets, achieving a superior performance of 0.91 mAP@50 compared to the baseline YOLOv12n. Crucially, with a lightweight architecture of only 2.6 million parameters, the network maintains ultra-fast inference speeds (4.24 to 4.43 ms), proving its readiness for real-time edge deployment and industrial field inspections.

General conclusion

This doctoral research has successfully demonstrated the viability and efficacy of advanced deep learning architectures for the automated non-contact inspection of PV assets across different structural scales. At the system level SP, this work established that the transformer-based RT-DETR architecture offers a superior paradigm for real-time thermal hotspot detection using IRT. It achieved a high mean Average Precision while significantly outperforming traditional single-stage detectors like YOLOv8-l, eliminating computational post-processing latency, and optimizing real-time edge viability. At the component level SC, this thesis introduced PV-YOLOv12n, an optimized lightweight model tailored for high-resolution EL imagery. By integrating the Attention-driven A2C2f module at the P5 scale, the network successfully suppressed structural background noise, such as busbars and finger lines, and focused features on subtle, low-contrast anomalies. The model achieved an improved accuracy across the PVEL-AD and Roboflow datasets while maintaining a minimal parameter footprint, making it highly suitable for high-throughput automated industrial inspection.

Limitations of the present work

Despite the high detection accuracy and processing speeds achieved, a critical evaluation of the experimental and methodological framework reveals several limitations that must be acknowledged:

- **The disconnect between visual anomalies and electrical degradation:** A primary limitation of this research is its isolation from live electrical parameters. While the developed deep learning models excel at localizing and classifying anomalies like microcracks or hotspots from thermal and EL imagery, they do not quantify the immediate or long-term impact of these defects on the actual energy yield or electrical integrity, such as I-V curve degradation or power output drop, of the PV module.
- **Dependence on static, publicly available datasets:** The training and evaluation of the models relied heavily on curated, closed benchmarks like PVEL-AD and Roboflow. These images, while highly diverse, represent static environmental conditions. The models have not been comprehensively validated against the broad variability of real-world operational

environments, such as sudden irradiance changes, varying drone flight altitudes, extreme weather conditions, or heavy atmospheric distortion.

- **Simplified categorization and binary constraints:** For certain training phases, multi-class defect scenarios were condensed into binary classifications, such as defective versus non-defective, to maintain statistical stability. In real-world environments, solar arrays often suffer from co-existing multi-defects, such as concurrent shadowing, delamination, and bypass diode failures, which a binary or strictly isolated multi-class model may struggle to accurately disentangle.
- **Hardware and spatial resolution thresholds:** The localization of deep microcracks in EL imagery remains highly sensitive to base image contrast and pixel density. In edge deployment scenarios where drone-mounted thermal or EL hardware faces payload constraints, lower-resolution inputs could lead to higher rates of False Negatives for early-stage or sub-millimeter cell fractures.

Perspectives for future research

Based on the identified limitations, several promising paths are proposed to advance this field of research:

- **Multi-modal data fusion (visual + thermal + electrical):** Future investigations should move away from single-modality imaging toward a holistic diagnostic framework. Combining structural EL data, thermal IRT data, and real-time electrical telemetry—such as I-V curves or IoT-based time-series current-voltage data—into a multi-modal deep learning network would bridge the gap between defect identification and absolute power loss estimation. This would allow operators to prioritize maintenance based on economic impact rather than visual severity alone.
- **Generative data augmentation for rare defect adaptation:** To resolve data scarcity and class imbalances for rare, highly critical fault modes like potential induced degradation (PID) or specific back contact failures, future work will investigate generative AI. Implementing specialized Generative Adversarial Networks (GANs) or Diffusion Models could synthesize physically accurate EL and thermal defect profiles. This would improve the network's robustness before real-world field deployment.

- **Self-supervised and semi-supervised learning frameworks:** To eliminate the time-consuming and manual process of human-annotated bounding boxes via platforms like CVAT, transitioning to self-supervised pre-training represents a critical next step. By training models on massive volumes of unlabeled aerial PV footage to learn foundational structural representations of normal panels, the network could flag defects as anomalies via unsupervised or semi-supervised reconstruction techniques.
- **Ultra-lightweight onboard processing for autonomous UAVs:** While PV-YOLOv12n and RT-DETR demonstrate excellent efficiency, additional architecture optimization is required to achieve completely autonomous edge intelligence. Future research will focus on model quantization, such as converting models from FP32 to INT8 precision, and knowledge distillation to embed these defect detection architectures directly onto ultra-low-power microcontrollers onboard autonomous drones. This would enable fully automated, real-time "detect-and-alert" flight patterns across utility-scale solar installations without requiring cloud telemetry links.

References

[1] C. Gu, G. Zhu, Y. Shi, L. Yao, and Y. Zhang, "IRH-DETR: an efficient real-time detection model for minute hotspot defects in photovoltaic panel infrared imagery," *Engineering Research Express,* vol. 8, no. 12, p. 125308, 2026.

[2] M. Shamisavi, I. Segovia Ramirez, and C. Q. Gómez Muñoz, "Comparative Evaluation of YOLO-and Transformer-Based Models for Photovoltaic Fault Detection Using Thermal Imagery," *Energies,* vol. 19, no. 3, p. 845, 2026.

[3] C. Dong, L. Chen, Y. Liu, Q. Hua, Y. Zhang, and F. Zhang, "An improved feature aggregation network for photovoltaic cell defect detection," *Journal of Renewable and Sustainable Energy,* vol. 17, no. 1, 2025.

[4] V. Boicea, D. Enescu, D. Sidea, P. Di Leo, G. Giacalone, and A. Ciocia, "Detection and Classification of Photovoltaic Module Defects Using Electroluminescence Imaging," in *2026 8th Global Power, Energy and Communication Conference (GPECOM)*, 2026: IEEE, pp. 570-575.

[5] M. Al-Mahbashi, S. A. Ghorashi, A. Khader, S. J. Malebary, H. E. A. Elsrej, G. Li, M. Al-Soswa, and A. Al-Radaei, "An effective approach to improving photovoltaic defect detection using the new DCD-YOLOv8s model," *Scientific Reports,* vol. 15, no. 1, p. 38308, 2025.

[6] W. Cai and H. Lv, "YOLO-PV: An Enhanced YOLO11n Model with Multi-Scale Feature Fusion for Photovoltaic Panel Defect Detection," *Energies,* vol. 18, no. 20, p. 5489, 2025.

[7] B. Zheng and Y. Yang, "AE-YOLO: Research and Application of the YOLOv11-Based Lightweight Improved Model in Photovoltaic Panel Surface Intelligent Defect Detection," *Materials,* vol. 18, no. 23, p. 5404, 2025.

[8] J. Zhu, X. Qian, L. Wang, C. Yin, T. Wang, Z. Xu, Z. Yao, and B. Wang, "YOLO-MSG: A Lightweight and Real-Time Photovoltaic Defect Detection Algorithm for Edge Computing," *Energies,* vol. 19, no. 9, p. 2043, 2026.

[9] A. Rahman, "Solar panel surface defect and dust detection: Deep learning approach," *Journal of Imaging,* vol. 11, no. 9, p. 287, 2025.

[10] J. Dun, H. Yang, S. Yuan, and Y. Tang, "EER-DETR: An Improved Method for Detecting Defects on the Surface of Solar Panels Based on RT-DETR," *Applied Sciences,* vol. 15, no. 11, p. 6217, 2025.

[11] H. Xiao and J. Zheng, "RT-DETR-Based Small-Sample Defect Detection for Solar Vacuum Glass Collector Tubes," *Applied Sciences,* vol. 16, no. 11, p. 5353, 2026.

[12] G. Liu, D. Yang, J. Ye, H. Lu, Z. Wang, and Y. Zhao, "A real-time welding defect detection framework based on RT-DETR deep neural network," *Advanced Engineering Informatics,* vol. 65, p. 103318, 2025.

[13] D. Shan, X. Tong, and D. Liu, "UDRT-DETR: a small UAV detection method based on infrared imaging and RT-DETR," *Applied Optics,* vol. 65, no. 8, pp. 2613-2627, 2026.

[14] D. Rahmouni, L.-H. Mouss, M. D. Mouss, and M. Benbouzid, "A YOLOv12-based Framework for Failure Diagnosis in Photovoltaic System Modules," in *IECON 2025–51st Annual Conference of the IEEE Industrial Electronics Society*, 2025: IEEE, pp. 1-6.

[15] A. Mohamed, Y. Nacera, B. Ahcene, A. Teta, E. O. Belabbaci, A. Rabehi, Y. A. Alsabah, and M. Benghanem, "Optimized YOLO based model for photovoltaic defect detection in electroluminescence images," *Scientific Reports,* vol. 15, no. 1, p. 32955, 2025.

[16] L. Clarke, Y.-M. Wei, A. De La Vega Navarro, A. Garg, A.N. Hahmann, S. Khennas, I.M.L. Azevedo, A. Löschel, A.K. Singh, L. Steg, G. Strbac, K. Wada. "IPCC Sixth Assessment Report, Working Group III: Mitigation of Climate Change, Chapter 6: Energy systems." https://www.ipcc.ch/report/ar6/wg3/chapter/chapter-6/ (accessed july 2026, 2026).

[17] X. Wang, L. Guo, G. Xue, J. Tan, W. Niu, and Y. Wu, "Toward Low-Carbon Power Systems: Reviewing Life Cycle Carbon Footprints of Diverse Generation Pathways," *Energies,* vol. 18, no. 24, p. 6413, 2025.

[18] R. Kumar, V. P. Singh, and M. K. Gupta, "Sustainable electricity generation through solar energy technologies," in *Renewable Energy Development: Technology, Material and Sustainability*: Springer, 2025, pp. 149-165.

[19] G. Bilicic and S. Scroggins, "Lazard's levelized cost of energy analysis-version 16.0," *Lazard, April,* 2023.

[20] M. Armiento, M. Lelli, C. Andrews, B. Idini, and R. Ruff, "Analysing the global workforce dynamics of the energy transition: main findings from the World Energy Employment report 2023," *Discover Sustainability,* vol. 6, no. 1, p. 35, 2025.

[21] R. N. (REN). "Global Overview." https://www.ren21.net/gsr-2025/global_overview/ (accessed july 2026, 2026).

[22] F. Bizzarri, S. Nitti, and G. Malgaroli, "The use of drones in the maintenance of photovoltaic fields," in *E3S web of Conferences*, 2019, vol. 119: EDP Sciences, p. 00021.

[23] P. Di Leo, A. Ciocia, G. Malgaroli, and F. Spertino, "Advancements and Challenges in Photovoltaic Power Forecasting: A Comprehensive Review," *Energies,* vol. 18, no. 8, p. 2108, 2025. [Online]. Available: https://www.mdpi.com/1996-1073/18/8/2108.

[24] R. N. (REN). "Renewables 2025 Global Status Report Collection." https://www.ren21.net/gsr-2025/technologies/solar-pv/ (accessed july 2026, 2026).

[25] N. Bala, M. Suleiman, J. Musa, S. H. Taiwo, U. Abdullahi, and A. Alhassan, "Comparative Analysis on the Performances of Monocrystalline and Polycrystalline Photovoltaic Cell (Pvc)," *Journal of Current Research and Studies,* vol. 3, no. 3, pp. 134-146, 2026.

[26] H. Yuan, "Structural Systems, Wind-load Mechanisms, and Engineering Applications of Photovoltaic Support Structures: A Review," *Advances in Research,* vol. 27, no. 1, pp. 286-296, 2026.

[27] V. Kaviya and V. Kirubakaran, "A review of inverter designs for solar PV systems and their performance enhancement via intelligent FACTS-based grid support," *Discover Applied Sciences,* 2026.

[28] S. Nandi, S. Barnwal, Y. V. Choudhary, T. Goswami, S. Karmakar, S. K. Kundu, and M. Gangopadhyaya, "Comparative Evaluation of Classical Perturb and Observe and Incremental Conductance MPPT Algorithms for Photovoltaic Systems," in *2026 9th International Conference on Electronics, Materials Engineering & Nano-Technology (IEMENTech)*, 2026, vol. 9: IEEE, pp. 1-6.

[29] A. Alsharif, K. S. Q. Qassab, A. Dobi, A. A. Ahmed, M. A. Alsharif, A. Almaktoof, and I. Imbamya, "A Comprehensive Review of Energy Storage Batteries for Solar Energy Systems," *Journal of Insights in Basic and Applied Sciences,* pp. 154-171, 2026.

[30] E. Dinesh, B. Sivashankar, K. Thakshith, R. Sowgar, and S. Sri Hari, "Design and Implementation of a PWM-Based Solar Charge Controller for Electric Vehicle Battery Management Using ATmega328," in *2026 International Conference on Visual Analytics and Data Visualization (ICVADV)*, 2026: IEEE, pp. 1452-1458.

[31] H. B. Morari, L. V. Bellinaso, E. L. Carvalho, S. N. Banavath, G. De Carne, and D. Vinnikov, "Solid-State Circuit Breakers for DC-Powered Buildings: An Overview of Standards, Directives, and Technologies," *IEEE Open Journal of Power Electronics,* 2026.

[32] N. K. Singh, S. Bhattacharya, and P. K. Sadhu, "Design of floating photovoltaic systems," *Floating Photovoltaics: Design, Performance, Degradation, Financial Sustainability, and Environmental Impacts,* p. 69, 2026.

[33] H. M. Snousi, F. A. Aleej, M. Bara, and A. Alkilany, "IoT-Enabled Real-Time Monitoring and Fault Diagnosis Framework for Smart Power Distribution Systems," *National Journal of Intelligent Power Systems and Technology,* pp. 26-33, 2026.

[34] A. Abass, "Light absorption enhancement and electronic properties of thin-film solar cells," Ghent University, 2014.

[35] A. S. Al-Ezzi and M. N. M. Ansari, "Photovoltaic solar cells: a review," *Applied System Innovation,* vol. 5, no. 4, p. 67, 2022.

[36] M. K. Singla, J. Gupta, M. Safaraliev, H. Zeinoddini-Meymand, and A. J. Ghanizadeh, "Mathematical modeling for solar cell optimization: evaluating sustainability with different diode configurations," *IEEE Access,* vol. 12, pp. 93802-93822, 2024.

[37] W. Abd El-Basit, A. M. Abd El-Maksood, and F. Soliman, "Mathematical model for photovoltaic cells," *Leonardo Journal of Sciences,* vol. 23, pp. 13-28, 2013.

[38] R. Aliev, J. Gulomov, A. Mirzaalimov, J. Kakhkhorov, and B. Rashidov, "ANALIZING THE EFFECT OF LIGHT INCIDENCE ANGLE ON PHOTOELECTRIC PARAMETERS OF SILICON SOLAR CELL," *Янги материаллар ва гелиотехнологиялар,* p. 161, 2030.

[39] A. H. Dawood and E. T. Hashim, "Simulink Model for Monocrystalline Solar Panel Performance," *Journal of Engineering,* vol. 32, no. 2, pp. 40-56, 2026.

[40] D. F. Muñoz-Torres, O. D. Montoya, J. C. Hernández, W. Gil-González, and L. F. Grisales-Noreña, "Enhancing Solar Cell Performance: Atan-Sinc Optimization Algorithm for Precise Parameter Extraction in the Three-Diode Model," *Applied System Innovation,* vol. 9, no. 1, p. 26, 2026.

[41] C. Wang, R. C. MacKenzie, U. Würfel, D. Neher, T. Kirchartz, C. Deibel, and M. Saladina, "Transport resistance dominates the fill factor losses in record organic solar cells," *Advanced energy materials,* vol. 16, no. 3, p. 2405889, 2026.

[42] R. Ananda, "Exploring the Origin of Instability in Thin-Film Solar Cells Based on Wide-Gap (Ag, Cu)(In, Ga) Se2 via Repeated Electrical Characterisation," ed, 2026.

[43] R. Tarkhasi, M. Deymi-Dashtebayaz, B. Amini, and S. Ghorbani, "A comprehensive review of CPVT solar systems: structural configurations, thermal management strategies, and

thermoelectric–CFD advances," *Energy Conversion and Management,* vol. 349, p. 120826, 2026.

[44] V. Kamala Devi, P. Valsaraj, and N. V. E. Pramod, "Experimentation, Simulation & Analysis of Partial Shading Effect in Solar Modules," *Energy Science & Engineering,* 2026.

[45] Q. Zhang, P. Chen, X. Zhao, X. Yu, A. R. b. M. Yusoff, Y. Yu, and P. Gao, "Thermal Management of Perovskite Solar Cells," *ChemSusChem,* vol. 19, no. 1, p. e202501649, 2026.

[46] A. Sohani, H. Sayyaadi, C. Cornaro, M. H. Shahverdian, M. Pierro, D. Moser, N. Karimi, M. H. Doranehgard, and L. K. Li, "Using machine learning in photovoltaics to create smarter and cleaner energy generation systems: A comprehensive review," *Journal of Cleaner Production,* vol. 364, p. 132701, 2022.

[47] G. Qin, Y. Jin, L. Qiao, and Z. Wu, "Advances, Challenges, and Recommendations for Non-Destructive Testing Technologies for Wind Turbine Blade Damage: A Review of the Literature from the Past Decade," *Sensors,* vol. 26, no. 6, p. 1773, 2026.

[48] K. Sharma, A. Kumar, V. Yadav, S. Dhar, and D. K. Banerjee, "From Detection to Prediction: The NDE 4.0 Transition," *NDT,* vol. 4, no. 3, p. 17, 2026.

[49] Z. Zhai, X. Li, J. Chen, B. Ruan, J. Lai, Q. Liu, and H. Zhou, "Bridging the scalability-stability gap in perovskite photovoltaics via solution-processed coating," *Science China Materials,* pp. 1-35, 2026.

[50] J. P. S. Briar and L. He, "A high efficiency solar cell and system," in *2021 IEEE 48th Photovoltaic Specialists Conference (PVSC)*, 2021: IEEE, pp. 0074-0079.

[51] X. Xu, H. Qiao, R. Ma, B. Wang, Z. Zhao, L. Li, X. Zhou, B. Yang, and X. Yu, "An experimental comparison study of full-flow photovoltaic/thermal and bifacial PV systems in Jiangsu, China," *Solar Energy,* vol. 303, p. 114105, 2026.

[52] A. A. Hasan, A. M. Zuhdi, A. Q. Al-Shetwi, M. A. Islam, K. P. Sankar, M. Idris, and G. Alkawsi, "Investigating Long-Term Degradation and Defects of Solar Photovoltaic Modules in Tropical Climates: A Case Study of Malaysia," *IET Renewable Power Generation,* vol. 20, no. 1, p. e70198, 2026.

[53] T. T. Cao, T. Van Pham, C. Van Trinh, H. P. Van, and A. Hoang, "Building Model for Forecasting Dust," in *Proceedings of the 4th International Conference on Cognitive and*

Intelligent Computing—Volume 2: ICCIC-2024, 29–30 November, Hyderabad, India, 2026: Springer Nature, p. 357.

[54] A. Gassner, G. C. Eder, J. Anger, and V.-M. Archodoulaki, "Evolution of the fluorine content in photovoltaic module backsheets," *Solar Energy Materials and Solar Cells,* vol. 304, p. 114393, 2026.

[55] M. A. A. Bin Ishak, M. A. A. Rahmat, S. I. Ud Din, and A. Ibrahim, "An Overview of Current State of Reuse and Recycling of Degraded Solar Modules: A Review," *Journal of Renewable Energy and Environment,* vol. 13, no. 2, pp. 79-92, 2026.

[56] G. Oreski, C. Barretta, P. Christöfl, P. Gebhardt, K. A. Weiß, D. C. Miller, S. Uličná, M. Kempe, L. S. Bruckman, and A. Virtuani, "What is a polyolefin? A critical overview of ethylene copolymers used as solar photovoltaic module encapsulants," *Progress in Photovoltaics: Research and Applications,* vol. 34, no. 4, pp. 367-395, 2026.

[57] V. Kamburov, M. Zagorski, D. Arnaudov, V. Mateev, A. Nikolov, K. Dimitrov, R. Dimitrova, E. Tongov, K. Petrov, and Y. Stoyanova, "Photovoltaic Panels' Thermo-Mechanical Delamination by Electric Resistive Heating," *Recycling,* vol. 11, no. 6, p. 108, 2026.

[58] X. Wang, W. Li, M. Xie, X. Wang, Y. Shuai, and Z. Wang, "Advanced bubble control engineered electrodes for high-efficient hydrogen evolution," *Renewable and Sustainable Energy Reviews,* vol. 226, p. 116368, 2026.

[59] F. J. Muñoz-Rodríguez, J. L. Sánchez-Jiménez, C. Robles, C. Ventura, C. Gilabert, C. Rus, and G. Jiménez-Castillo, "String level DC performance analysis in Rooftop photovoltaic systems with multi-MPPT inverters," *Solar Energy,* vol. 308, p. 114359, 2026.

[60] M. A. Monnaf, A. Ghosh, A. I. Shimul, Q. Hossain, L. Ferdoush, M. F. I. Buian, A. K. Roy, S. Ahmed, M. M. Rahman, and N. L. Dey, "Numerical Modeling and machine learning-assisted analysis of ultra-thin CuSbS2 solar cells incorporating SnS2 ETL and V2O5 BSF layers," *Journal of Inorganic and Organometallic Polymers and Materials,* vol. 36, no. 2, pp. 1050-1071, 2026.

[61] F. Doğan, M. Aktaş, N. Olgun, M. Çalışan, and İ. Türkoğlu, "Detection of Cell Damage and Types in Solar Panels: A Comprehensive Review," *Dicle Üniversitesi Mühendislik Fakültesi Mühendislik Dergisi,* vol. 17, no. 1, 2026.

[62] P. Dixit, V. Shah, P. Mehta, H. Patel, R. Sathyamurthy, A. E. Kabeel, and A. J. Santhosh, "Systematic review of soiling mitigation strategies for solar photovoltaic panels," *Discover Sustainability,* vol. 7, no. 1, p. 428, 2026.

[63] X. Liu, G. Zhu, Z. Li, and D. Li, "A comprehensive evaluation framework using generative adversarial networks for infrared defect images in photovoltaic modules," *Solar Energy,* vol. 306, p. 114311, 2026.

[64] M. Kaintz and A. Cammarata, "From Defects to Devices: Design Guidelines for High-Performance Diamond-Based Solar Cells and Single-Dopant Diodes," *arXiv preprint arXiv:2605.04942,* 2026.

[65] A. Bouraiou, M. Hamouda, A. Chaker, A. Neçaibia, M. Mostefaoui, N. Boutasseta, A. Ziane, R. Dabou, N. Sahouane, and S. Lachtar, "Experimental investigation of observed defects in crystalline silicon PV modules under outdoor hot dry climatic conditions in Algeria," *Solar Energy,* vol. 159, pp. 475-487, 2018.

[66] D. Lausch, M. Patzold, M. Rudolph, C.-M. Lin, J. Fröbel, and K. Kaufmann, "Magnetic field imaging (MFI) of solar modules," in *35th European Photovoltaic Solar Energy Conference and Exhibition*, 2018: EU PVSEC), pp. 1060-1064.

[67] M. Achit, N. Yassa, A. Bouzida, A. Mazari, and O. Fergani, "Enhancing PV panel diagnosis: RT-DETR vs YOLO v8 for real-time hotspots detection," *Studies in Engineering and Exact Sciences,* vol. 5, no. 2, pp. e8390-e8390, 2024.

[68] A. Salimi, S. H. Sedani, M. Ghasemi, S. K. Ünver, E. Dönerçark, M. Koç, V. Depauw, H. S. Radhakrishnan, H. Nasser, and R. Turan, "Compositional analysis of (p) a-SiCx: H emitter layers for enhanced short-circuit current density in SHJ solar cells," *Materials Science in Semiconductor Processing,* vol. 214, p. 110912, 2026.

[69] R. Alonso, F. Castaño, Y. J. Cruz, A. Villalonga, and R. E. Haber, "Early defect detection in thermo-insulating panels: A case study on quality inspection," *The International Journal of Advanced Manufacturing Technology,* vol. 142, no. 1, pp. 493-509, 2026.

[70] U. Jahn, M. Herz, M. Köntges, D. Parlevliet, M. Paggi, I. Tsanakas, J. Stein, K. A. Berger, S. Ranta, and R. H. French, *Review on infrared and electroluminescence imaging for PV field applications: International Energy Agency Photovoltaic Power Systems Programme*. International Energy Agency, 2018.

[71] G. Goudelis, P. I. Lazaridis, and M. Dhimish, "A review of models for photovoltaic crack and hotspot prediction," *Energies,* vol. 15, no. 12, p. 4303, 2022.

[72] O. Breitenstein, "Illuminated versus dark lock-in thermography investigations of solar cells," *International Journal of Nanoparticles,* vol. 6, no. 2-3, pp. 81-92, 2013.

[73] A. H. Aksoy, A. N. Özsezen, and T. Özden, "Evaluation of a VIPV-Based Solar-Assisted Charging System with Multi-MPPT Control and Shingled PV Panels for Electric Urban Delivery Motorcycles," *International Journal of Automotive Science And Technology,* vol. 10, no. 2, pp. 427-436.

[74] S. Meyer, S. Richter, S. Timmel, M. Gläser, M. Werner, S. Swatek, and C. Hagendorf, "Snail trails: root cause analysis and test procedures," *Energy Procedia,* vol. 38, pp. 498-505, 2013.

[75] K. Jäger, U. Aeberhard, E. Alarcon Llado, B. Bläsi, S. Burger, B. Ehrler, W. Favre, A. Fejfar, T. Gageot, and I. Gordon, "Optics for terawatt-scale photovoltaics: review and perspectives," *Advances in Optics and Photonics,* vol. 17, no. 1, pp. 185-294, 2025.

[76] J. Weber, S. Hoffmann, K. Kaufmann, and A. De Rose, "Magnetic field imaging (MFI) of shingle solar modules," in *2022 IEEE 49th Photovoltaics Specialists Conference (PVSC)*, 2022: IEEE, pp. 1424-1427.

[77] A. M. Al-Amri, "Printed sensors for environmental monitoring: Advancements, challenges, and future directions," *Chemosensors,* vol. 13, no. 8, p. 285, 2025.

[78] E. Parladi and E. Adiguzel, "A Multimodal Data-Driven Framework for Failure Analysis and Performance Degradation of Photovoltaic Panels in Smart City Applications," *IEEE Access,* 2026.

[79] D. M. Kaddes, P. A. E. khedr, and P. M. A. Belal, "Optimizing energy consumption: a strategy for UAV-based inspection systems in photovoltaic power plants," *Future Business Journal,* vol. 12, no. 1, p. 62, 2026.

[80] S. Keszthelyi, Z. Pónya, Á. Csóka, G. Bázár, T. Morschhauser, and T. Donkó, "Non-destructive imaging and spectroscopic techniques to investigate the hidden-lifestyle arthropod pests: A review," *Journal of Plant Diseases and Protection,* vol. 127, no. 3, pp. 283-295, 2020.

[81] S. Besold, U. Hoyer, J. Bachmann, T. Swonke, P. Schilinsky, R. Steim, and C. Brabec, "Quantitative imaging of shunts in organic photovoltaic modules using lock-in thermography," *Solar Energy Materials and Solar Cells,* vol. 124, pp. 133-137, 2014.

[82] D. B. Sulas-Kern, S. Johnston, M. Owen-Bellini, K. Terwilliger, J. Meydbray, L. Spinella, A. Sinha, L. T. Schelhas, and D. C. Jordan, "UV-fluorescence imaging of silicon PV modules after outdoor aging and accelerated stress testing," in *2020 47th IEEE Photovoltaic Specialists Conference (PVSC)*, 2020: IEEE, pp. 1444-1448.

[83] A. Paduthol, O. Kunz, K. Kaufmann, M. Patzold, D. Lausch, and T. Trupke, "Magnetic field imaging: strengths and limitations in characterising solar cells," in *2019 IEEE 46th Photovoltaic Specialists Conference (PVSC)*, 2019: IEEE, pp. 0822-0824.

[84] H. Tella, M. A. Mohandes, B. Liu, A. Al-Shaikhi, and S. Rehman, "A Novel Cost-Function for Transformer-based YOLO Algorithm to Detect Photovoltaic Panel Defects," *FME Transactions,* vol. 52, no. 4, 2024.

[85] R. del Prado Santamaría, M. Dhimish, G. A. dos Reis Benatto, T. Kari, P. B. Poulsen, and S. V. Spataru, "From indoor to daylight electroluminescence imaging for PV module diagnostics: A comprehensive review of techniques, challenges, and AI-driven advancements," *Micromachines,* vol. 16, no. 4, p. 437, 2025.

[86] A. Wang and Y. Xuan, "Close examination of localized hot spots within photovoltaic modules," *Energy Conversion and Management,* vol. 234, p. 113959, 2021.

[87] D. Y. Goswami, *Principles of solar engineering*. CRC press, 2022.

[88] R. A. Eltuhamy, M. Rady, E. Almatrafi, H. A. Mahmoud, and K. H. Ibrahim, "Fault detection and classification of CIGS thin-film PV modules using an adaptive neuro-fuzzy inference scheme," *Sensors,* vol. 23, no. 3, p. 1280, 2023.

[89] G. Ramadas, "Detection of Cracks in Solar Panel Images Using Complex Wavelet Transform and ANFIS Classification Method," 2023.

[90] T. Boot and H. Irshad, "Diagnostic assessment of deep learning algorithms for detection and segmentation of lesion in mammographic images," in *International conference on medical image computing and computer-assisted intervention*, 2020: Springer, pp. 56-65.

[91] K. Takahashi, K. Yamamoto, A. Kuchiba, and T. Koyama, "Confidence interval for micro-averaged F 1 and macro-averaged F 1 scores," *Applied Intelligence,* vol. 52, no. 5, pp. 4961-4972, 2022.

[92] S. Deitsch, V. Christlein, S. Berger, C. Buerhop-Lutz, A. Maier, F. Gallwitz, and C. Riess, "Automatic classification of defective photovoltaic module cells in electroluminescence images," *Solar Energy,* vol. 185, pp. 455-468, 2019.

[93] A. S. Al-Waisy, D. A. Ibrahim, D. A. Zebari, S. Hammadi, H. Mohammed, M. A. Mohammed, and R. Damaševičius, "Identifying defective solar cells in electroluminescence images using deep feature representations," *PeerJ Computer Science,* vol. 8, p. e992, 2022.

[94] P. Parhar, R. Sawasaki, A. Todeschini, H. Vahabi, N. Nusaputra, and F. Vergara, "HyperionSolarNet: Solar panel detection from aerial images," *arXiv preprint arXiv:2201.02107,* 2022.

[95] K. Perry and C. Campos, "Panel segmentation: A python package for automated solar array metadata extraction using satellite imagery," *IEEE Journal of Photovoltaics,* vol. 13, no. 2, pp. 208-212, 2023.

[96] M. V. C. V. d. Costa, O. L. F. d. Carvalho, A. G. Orlandi, I. Hirata, A. O. d. Albuquerque, F. V. e. Silva, R. F. Guimarães, R. A. T. Gomes, and O. A. d. C. Júnior, "Remote sensing for monitoring photovoltaic solar plants in Brazil using deep semantic segmentation," *Energies,* vol. 14, no. 10, p. 2960, 2021.

[97] L. Li and E. Lau, "RU-Net: Solar panel detection from remote sensing image," in *2022 IEEE Green Energy and Smart System Systems (IGESSC)*, 2022: IEEE, pp. 1-6.

[98] H. Jiang, L. Yao, N. Lu, J. Qin, T. Liu, Y. Liu, and C. Zhou, "Multi-resolution dataset for photovoltaic panel segmentation from satellite and aerial imagery," *Earth System Science Data Discussions,* vol. 2021, pp. 1-17, 2021.

[99] A. Sampath, P. Bijapur, A. Karanam, V. Umadevi, and M. Parathodiyil, "Estimation of rooftop solar energy generation using satellite image segmentation," in *2019 IEEE 9th International Conference on Advanced Computing (IACC)*, 2019: IEEE, pp. 38-44.

[100] N. Wang, Z.-L. Sun, Z. Zeng, and K.-M. Lam, "Effective segmentation approach for solar photovoltaic panels in uneven illuminated color infrared images," *IEEE Journal of Photovoltaics,* vol. 11, no. 2, pp. 478-484, 2020.

[101] D. d. B. Soares, F. Andrieux, B. Hell, J. Lenhardt, J. Badosa, S. Gavoille, S. Gaiffas, and E. Bacry, "Predicting the solar potential of rooftops using image segmentation and structured data," *arXiv preprint arXiv:2106.15268,* 2021.

[102] A. Di Tommaso, A. Betti, G. Fontanelli, and B. Michelozzi, "A multi-stage model based on YOLOv3 for defect detection in PV panels based on IR and visible imaging by unmanned aerial vehicle," *Renewable energy,* vol. 193, pp. 941-962, 2022.

[103] T. Tajwar, O. H. Mobin, F. R. Khan, S. F. Hossain, M. Islam, and M. M. Rahman, "Infrared thermography based hotspot detection of photovoltaic module using YOLO," in *2021 IEEE 12th Energy Conversion Congress & Exposition-Asia (ECCE-Asia)*, 2021: IEEE, pp. 1542-1547.

[104] X. Zhu, S. Lyu, X. Wang, and Q. Zhao, "TPH-YOLOv5: Improved YOLOv5 based on transformer prediction head for object detection on drone-captured scenarios," in *Proceedings of the IEEE/CVF international conference on computer vision*, 2021, pp. 2778-2788.

[105] S. P. Pathak, S. Patil, and S. Patel, "Solar panel hotspot localization and fault classification using deep learning approach," *Procedia Computer Science,* vol. 204, pp. 698-705, 2022.

[106] T. Sun, H. Xing, S. Cao, Y. Zhang, S. Fan, and P. Liu, "A novel detection method for hot spots of photovoltaic (PV) panels using improved anchors and prediction heads of YOLOv5 network," *Energy Reports,* vol. 8, pp. 1219-1229, 2022.

[107] X. Li, Q. Yang, Z. Chen, X. Luo, and W. Yan, "Visible defects detection based on UAV-based inspection in large-scale photovoltaic systems," *IET Renewable Power Generation,* vol. 11, no. 10, pp. 1234-1244, 2017.

[108] P. Zhu, L. Wen, D. Du, X. Bian, H. Fan, Q. Hu, and H. Ling, "Detection and tracking meet drones challenge," *IEEE transactions on pattern analysis and machine intelligence,* vol. 44, no. 11, pp. 7380-7399, 2021.

[109] L. Li, Z. Wang, and T. Zhang, "Photovoltaic panel defect detection based on ghost convolution with BottleneckCSP and tiny target prediction head incorporating YOLOv5," *arXiv preprint arXiv:2303.00886,* 2023.

[110] F. Hong, J. Song, H. Meng, R. Wang, F. Fang, and G. Zhang, "A novel framework on intelligent detection for module defects of PV plant combining the visible and infrared images," *Solar Energy,* vol. 236, pp. 406-416, 2022.

[111] M. Zhang and L. Yin, "Solar cell surface defect detection based on improved YOLO v5," *IEEE access,* vol. 10, pp. 80804-80815, 2022.

[112] Q. Zheng, J. Ma, M. Liu, Y. Liu, Y. Li, and G. Shi, "Lightweight hot-spot fault detection model of photovoltaic panels in UAV remote-sensing image," *Sensors,* vol. 22, no. 12, p. 4617, 2022.

[113] S. Hassan and M. Dhimish, "Enhancing solar photovoltaic modules quality assurance through convolutional neural network-aided automated defect detection," *Renewable Energy,* vol. 219, p. 119389, 2023.

[114] Y. Cao, D. Pang, Q. Zhao, Y. Yan, Y. Jiang, C. Tian, F. Wang, and J. Li, "Improved YOLOv8-GD deep learning model for defect detection in electroluminescence images of solar photovoltaic modules," *Engineering Applications of Artificial Intelligence,* vol. 131, p. 107866, 2024.

[115] A. Ghahremani, S. D. Adams, M. Norton, S. Y. Khoo, and A. Z. Kouzani, "Detecting defects in solar panels using the YOLO v10 and v11 algorithms," *Electronics,* vol. 14, no. 2, p. 344, 2025.

[116] N. Wang, S. Huang, X. Liu, Z. Wang, Y. Liu, and Z. Gao, "MRA-YOLOv8: a network enhancing feature extraction ability for photovoltaic cell defects," *Sensors,* vol. 25, no. 5, p. 1542, 2025.

[117] G. Xu, J. Huang, W. Gong, and J. Teng, "Solar Cell Defects Detection Based on Photoluminescence Images and Upgraded YOLOv5 Model," *Journal of Engineering,* vol. 2025, no. 1, p. 8397362, 2025.

[118] I. Nasri, M. Mansouri, M. Trabelsi, L. Kheriji, and A. W. Skorek, "A Review on Multimodal-Based Fault Detection and Diagnosis in Photovoltaic Systems: Fusion and Attention Mechanisms," *IEEE Access,* 2026.

[119] K. AbdulMawjood, S. S. Refaat, and W. G. Morsi, "Detection and prediction of faults in photovoltaic arrays: A review," in *2018 IEEE 12th international conference on compatibility, power electronics and power engineering (CPE-POWERENG 2018)*, 2018: IEEE, pp. 1-8.

[120] A. Najiah Nurul Afifah, I. Indrabayu, A. Suyuti, and S. Syafaruddin, "A review on image processing techniques for damage detection on photovoltaic panels," *ICIC International,* 2021.

[121] Y. Zhang, M. Sakhuja, F. J. Lim, S. Tay, C. Tan, M. Bieri, V. A. Krishnamurthy, D. Wang, P. K. Krishnakumar, and J. Ha, "The PV System Doctor–Comprehensive diagnosis of PV system installations," *Energy Procedia,* vol. 130, pp. 108-113, 2017.

[122] B. Aboagye, S. Gyamfi, E. A. Ofosu, and S. Djordjevic, "Characterisation of visual defects on installed solar photovoltaic (PV) modules in different climatic zones in Ghana," *Scientific African,* vol. 20, p. e01682, 2023.

[123] S. Gallardo-Saavedra, L. Hernádez-Callejo, and Ó. Duque-Pérez, "Analysis and characterization of PV module defects by thermographic inspection," *Revista Facultad de Ingeniería Universidad de Antioquia,* no. 93, pp. 92-104, 2019.

[124] E. V. Kurian, A. Krishna, D. S. Pillai, M. I. Hossain, A. Krama, S. Bayhan, and B. Aissa, "Fault detection and diagnosis in PV systems," 2026.

[125] E. Ahani, J. Yang, and A. Ahani, "Structural glass health monitoring: A comparative evaluation of flaw detection approaches," *Composite Structures,* p. 120072, 2026.